NUCLEAR REACTIONS LEADING TO ENERGY LEVELS OF Ar^{37} AND K^{37}

Thesis by

James Henry McNally

In Partial Fulfillment of the Requirements

For the Degree of

Doctor of Philosophy

California Institute of Technology

Pasadena, California

1966

(Submitted October 18, 1965)

ACKNOWLEDGMENTS

I would like to thank the faculty of Kellogg Radiation Laboratory for the efforts they have extended on my behalf. In particular, I would like to thank Professor W. Whaling for his continued efforts. I appreciate several encouraging discussions with Professors C.M. Class and L. Davis, Jr., and Dr. H. Winkler.

I am grateful for discussions with Professors J.N. Bahcall, C.A. Barnes, and R.W. Kavanagh concerning the mass 37 system and for the interest they have shown in this work. I acknowledge gratefully the close working relationship with D.E. Groce during the assembly of the spectrometer and the initial Ne^{20} experiment. Most of the data on array operation were collected in collaboration with L. Cocke. W.D. Harrison furnished aid and instruction during the use of the scattering chamber. A. Bacher wrote the Q-value computer program. R. Miller supervised the design and construction of the emulsion holder. The aid of the entire Kellogg staff has been sincerely appreciated.

Financial aid in the form of a Woodrow Wilson Fellowship, Institute Scholarships and Assistantships derived from Office of Naval Research contracts is greatly appreciated.

Finally, without the aid of my wife, Nancy, this thesis would not exist. Words cannot express my gratitude.

ABSTRACT

In view of recent interest in the $Cl^{37}(\nu_{solar}, e-)Ar^{37}$ reaction cross section, information on some aspects of mass 37 nuclei has been obtained using the $K^{39}(d, \alpha)Ar^{37}$ and $Cl^{35}(He^3, p)Ar^{37}$ reactions. Ar^{37} levels have been found at 0, 1.41, 1.62, 2.22, 2.50, 2.80, 3.17, 3.27, 3.53, 3.61, 3.71, (3.75), (3.90), 3.94, 4.02, (4.21), 4.28, 4.32, 4.40, 4.45, 4.58, 4.63, 4.74, 4.89, 4.98, 5.05, 5.10, 5.13, 5.21, 5.35, 5.41, 5.44, 5.54, 5.58, 5.67, 5.77, and 5.85 MeV (the underlined values correspond to previously tabulated levels). The nuclear temperature calculated from the Ar^{37} level density is 1.4 MeV. Angular distributions of the lowest six levels with the $K^{39}(d, \alpha)Ar^{37}$ reaction at $E_d = 10$ MeV indicate a dominant direct interaction mechanism and the inapplicability of the $2I + 1$ rule of the statistical model. Comparison of the spectra obtained with the $K^{39}(d, \alpha)Ar^{37}$ and $Cl^{35}(He^3, p)Ar^{37}$ reactions leads to the suggestion that the 5.13-MeV level is the $T = 3/2$ Cl^{37} ground state analog. The ground state Q-value of the $Ca^{40}(p, \alpha)K^{37}$ reaction has been measured: -5179 ± 9 keV. This value implies a K^{37} mass excess of -24804 ± 10 keV. Description of a NMR magnetometer and a sixteen-detector array used in conjunction with a 61-cm double-focusing magnetic spectrometer are included in appendices.

TABLE OF CONTENTS

I. INTRODUCTION

A. SOLAR ν'S

Since neutrinos are the only known participants in nuclear reactions that have a mean free path at least as large as the solar radius, it is of interest to consider what astrophysical information can be extracted from the detection of solar neutrinos.

Fowler (1960) and Parker, Bahcall, and Fowler (1964) have discussed in detail the fusion reactions that are currently believed to be the primary sources of solar energy. The basic reaction is $H^1(p,e^+\nu)H^2(p,\gamma)He^3$ followed by:

1) $He^3(He^3,2p)He^4$
2) $He^3(\alpha,\gamma)Be^7(e^-,\nu)Li^7(p,\alpha)He^4$
3) $He^3(\alpha,\gamma)Be^7(p,\gamma)B^8(e^+\nu)Be^{8*}(\alpha)He^4$
4) $He^3(p,\gamma)Li^4(e^+\nu)He^4$

The fourth termination branch produces less than 0.2% of the total He^4 generated (Bahcall 1964a). The carbon-nitrogen-oxygen cycle is currently believed to contribute only a few per cent of the total energy generated by the sun (Sears 1964).

Calculations of the solar neutrino flux at the earth have been carried out by the construction and solution of a variety of solar models (Sears 1960, Bahcall, Fowler, Iben and Sears 1963, Sears 1964, Bahcall 1964b). The complex shape of the neutrino energy spectrum is evident from Table I, which indicates the reactions and fluxes currently

believed to be primarily responsible for solar neutrinos. An experimental determination of the neutrino spectrum outlined in Table I would:

1) resolve the flux contributions of individual nuclear reactions and make clearer the role of nuclear reactions in the sun, and

2) provide an accurate measurement of the central solar temperature by utilizing the temperature dependence of the $Be^7(p, \gamma)B^8$ cross section.

B. THE $Cl^{37}(\nu_{solar}, e^-)Ar^{37}$ EXPERIMENT

A neutrino detection scheme based on the detection of Ar^{37} nuclei produced by the $Cl^{37}(\nu_{solar}, e^-)Ar^{37}$ reaction has been shown to be feasible (Davis 1964). It is expected that this experiment will furnish information primarily on high-energy solar neutrinos. The cross section, σ, for this reaction has been predicted by Bahcall (1964a, b, and c). The number of expected Ar^{37} nuclei created, per unit time per Cl^{37} atom is simply

$$N = \int \sigma \phi \, dE$$

where ϕ is the neutrino flux and E the neutrino energy.

In order to calculate the reaction cross section, Bahcall has assumed the validity of the shell model. He assumes that only the five states of $_{18}Ar^{37}_{19}$ involving the coupling of the $1d^2_{3/2}$ proton holes and the $1d_{3/2}$ neutron hole will have large matrix elements for the $Cl^{37}(\nu, e^-)Ar^{37}$ reaction. The first calculations were based on the level

assignments shown in Figure 1. These calculations produced both the matrix elements for the $Cl^{37}(\gamma, e^-)Ar^{37}$ reaction and the matrix elements for β decays in the remainder of the mass 37 system. The calculations have stimulated interest in the experimental determination of the predicted branching ratios for β decay in the mass 37 system as well as the collection of information about the Ar^{37} level structure.

C. OUTLINE OF PRESENT EXPERIMENT

The primary purpose of the experiment described in this thesis was to investigate the level structure of Ar^{37}. The experiment may be divided into four parts as follows:

1) Alpha spectra from the $K^{39}(d, \alpha)Ar^{37}$ reaction were used to locate Ar^{37} levels below 4.5-MeV excitation energy. This work is described in Part III, pages 22 to 29.

2) Angular distributions of the first six states in Ar^{37} were measured with the $K^{39}(d, \alpha)Ar^{37}$ reaction using 10-MeV incident deuterons. This work is described in Part IV, pages 30 to 45.

3) Spectra from the $Cl^{35}(He^3, p)Ar^{37}$ and $K^{39}(d, \alpha)Ar^{37}$ reactions were used in a search for the Ar^{37} $T = 3/2$ state that is the analog of the Cl^{37} ground state. This work is described in Part V, pages 46 to 70.

4) The ground state Q-value of the $Ca^{40}(p, \alpha)K^{37}$ reaction was measured. This work is described in Part

II, pages 7 to 21.

D. OTHER RELATED Ar^{37} AND K^{37} EXPERIMENTS

The known Ar^{37} level structure at the start of the experimental work described in section C is shown in Figure 1. The primary experiments leading to this level structure are summarized below; the levels observed in some of these experiments are listed in Table IV.

$Ar^{36}(d,p)Ar^{37}$. Davison et al.(1949) employed a detection scheme consisting of a proportional counter with absorbers to determine the proton energy. A discriminator was employed to select only the highest energy pulses from the counter. Contaminant Ar^{40} protons partially obscured the region above 2.6-MeV Ar^{37} excitation, and only the ground state, 1.42-, 1.61-, 2.25-, 2.54-, 3.55-, and 5.07-MeV levels were observed. Zucker and Watson (1950) employed the same system of proton detection but used a target with a higher degree of Ar^{36} enrichment and reported all the levels of Figure 1 above 2.5 MeV. Owing to slightly poorer resolution they did not see the 1.62- or 2.25-MeV levels. Yamamoto and Steigert (1961) obtained $l_n = 2,0$, and 2 angular distributions for the first three levels respectively, using $E_d = 3.85$ MeV and proton ranges in emulsions to identify the proton groups.

$Cl^{37}(p,n)Ar^{37}$. Ferguson and Paul (1959) obtained an excitation spectrum at zero degrees and placed ± 10-keV errors on levels at 0, 1.42, 1.61, 2.25 and 2.41 MeV.

Their published spectrum ends two points above 2.41-MeV excitation energy and the reduced magnitude of these points appears to be the only evidence for a 2.41-MeV level.

$S^{34}(\alpha,n)Ar^{37}$. Nelson et al.(1963) have found Ar^{37} levels at 0, (0.70), 1.54, 2.56, 3.50, 4.40, and 4.63 $\pm$ .05 MeV by means of a zero degree spectrum.

The hyperfine structure of Ar^{37} has been investigated by Robertson et al.(1960, 1965). This investigation has led to the 3/2 spin assignment for the ground state.

Previous work on the specific reactions studied has been sparse. The $K^{39}(d,\alpha)Ar^{37}$ reaction was utilized in an early measurement of the half life of Ar^{37} by observing the K conversion electron capture (Weimer, Kurbatov, and Pool 1944). The $Ca^{40}(p,\alpha)K^{37}$ reaction was used to manufacture K^{37} leading to the beta decay of K^{37} with a 5.10 $\pm$ 0.07-MeV end point energy (Sun and Wright 1958).

A large number of experimenters began working on the mass 37 system simultaneously with the experiment reported here. The work directly relating to this thesis is summarized below. Some of these experiments will be discussed later in greater detail.

$Ar^{36}(d,p)Ar^{37}$. Rosner and Schneid (1964, 1965) have studied this reaction with a beam of 15-MeV deuterons and solid state detectors; the spin assignments determined from their angular distribution are given in Figure 2. Wiza et al.(1965) are conducting high resolution level surveys

with the reaction $Ar^{36}(d,p)Ar^{37}$.

$Cl^{35}(He^3,p)Ar^{37}$. Castro (1964) has obtained spectra of Ar^{37} levels below 6.1-MeV excitation energy. DWBA fits to the angular distributions of some of the low-lying levels were attempted.

$K^{39}(d,\alpha)Ar^{37}$. Rawlins et al.(1964) have investigated this reaction with deuteron energies of 3 to 4 MeV, from the standpoint of the statistical model and the $2I+1$ rule.

$Ca^{40}(p,\alpha)K^{37}(e^+\nu)Ar^{37}$ and $Ar^{36}(p,\gamma)K^{37}(e^+\nu)Ar^{37}$. Kavanagh and Goosman (1964, 1965) have determined the branching ratios of K^{37} beta decay. From gamma angular distributions they conclude that the spin and parity of the 2.80-MeV Ar^{37} level (mirror of the 2.74-MeV K^{37} level) is $(5/2+)$.

$Cl^{37}(p,n)Ar^{37}$. Davies and Barnes (1964) have obtained time-of-flight neutron spectra at zero degrees. They do not see the 2.41-MeV level of Ferguson and Paul (1959). Adelberger and Barnes (1965) have obtained similar spectra of the 5-MeV Ar^{37} region.

$Ca^{40}(p,\alpha)K^{37}$. Kavanagh and Goosman (1965) have observed the ground state of K^{37} in their $Ca^{40}(p,\alpha)K^{37}$ study of K^{37} levels below 2.8 MeV.

Lowest K^{37} $T=3/2$ Level. The Ca^{37} beta decay studies of Hardy and Verrall (1964) and Reeder et al. (1964) and the K^{37} studies of Kavanagh and Goosman (1965) lead to a 5040 $\pm$ 12 keV value for the lowest K^{37} $T=3/2$ level.

II. $Ca^{40}(p,\alpha)K^{37}$ GROUND STATE Q-VALUE

A. INTRODUCTION

Measurement of the $Ca^{40}(p,\alpha)K^{37}$ Q-value was undertaken to reduce the 45-keV K^{37} mass uncertainty appearing in the 1964 mass tables of Mattauch et al.(1965). This uncertainty limits the accuracy of the experimental K^{37} - Ar^{37} ft values to approximately 5%.

The K^{37} mass is also of interest in computing the excitation energy of K^{37} levels corresponding to resonances in the Ar^{36}+ p excitation function (Kavanagh and Goosman 1964). The Ar^{36}+ p energy is known to within ± 4 keV. In order to relate the energy of the K^{37} states above the Ar^{36}+ p threshold to the ground state, either a measurement of the gamma energy or an independent measurement of the K^{37} ground state mass is required. Kavanagh and Goosman (1964) have measured the gamma ray energy (±10 keV) and find the mass excess of K^{37} is -24793 ± 11 keV.

The measurement of the $Ca^{40}(p,\alpha)K^{37}$ ground state Q-value was begun while the He^3 injector was out of order, and work on the $Cl^{35}(He^3,p)Ar^{37}$ reaction could not proceed. Because of the limited amount of machine time available, the measurement does not demonstrate the accuracy to which a Q-value measurement could be made with the spectrometer. It is described as the first of the work on the mass 37 system because it utilizes and illustrates most of

the spectrometer techniques employed in these thesis experiments. The 61-cm spectrometer has been described in detail by Groce (1963); no further description is given since the apparatus is now a routinely-operated piece of experimental equipment in conjunction with the ONR-CIT tandem accelerator. The discussion of the present experiments assumes familiarity with either the thesis of Groce or the operation of the spectrometer.

B. TARGETS

The thick targets used for the measurement of the $Ca^{40}(p, \alpha)K^{37}$ ground state Q-value were made by evaporating natural calcium pellets in the target chamber furnace illustrated by Groce (1963). The calcium was evaporated from a holder made from tantalum sheet onto commercial 23-karat gold leaf (Hastings and Co.) of approximately 1000 Angstroms thickness.

The alphas were detected with the 61-cm spectrometer placed at either 90^{o} or 150^{o} to the incident beam. The normal to the calcium surface bisected the angle between the incoming beam and the magnet entrance. By observing the alphas in the backward hemisphere the target could be used in a "reflecting" rather than "transmitting" geometry. The highest energy alphas originate in the exposed surface of the calcium and do not pass through the gold backing. Target loss corrections would be required if either the

protons or alpha particles passed through the thick calcium or gold backing before the alphas entered the spectrometer.

The use of a thick target simplifies the determination of target thickness; the ideal spectrum of counts vs. frequency will be a step function with the surface target nuclei contributing the counts at the step edge. Both Ca^{42} (0.6%) and Ca^{44}(2.1%) undergo (p, α)reactions that could contribute an alpha continuum in the momentum region of the ground state group from the 97% Ca^{40} in the target. No background continuum is seen, and it is possible to use thick targets.

C. SPECTRA COLLECTION DETAILS

The particle detection system for the magnetic spectrometer is quite versatile, consisting of

1) a single solid state detector placed in the focal plane to intercept the central ray of the spectrometer,

2) an array of sixteen solid state detectors arranged along the focal plane of the spectrometer, and

3) three 2.5-cm x 15.2-cm nuclear emulsions that may be located in the focal plane to provide six exposures without disturbing the spectrometer vacuum system.

Preliminary $Ca^{40}(p,\alpha)K^{37}$ surveys with the detector array

were made using both thick and thin targets. Although the array immediately indicates whether the thick target criterion has been satisfied, it is of little value in examining the detailed structure of the thick target step because the spacing of the detectors is 5.80 mm (from center to center) compared with the 1.84-mm slit size which principally determines the frequency width of the step. The spectra used in determining the Q-value for the K^{37} ground state are shown in Figure 3. After the array was used to determine the target thickness, detector 8 (the central ray detector) was connected to a standard Ortec preamplifier whose output was examined by 100 channels of an RIDL 400-channel analyzer. The spectra from the remaining array detectors were stored in one-quarter of a Nuclear Data 4096-channel analyzer and served only to substantiate the background and plateau counting rates. The nuclear data memory was printed out only after each of the spectra of Figure 3 was completed. Since the printout time of the RIDL 100 channels is much less than the Nuclear Data 1024 channels, this procedure not only saves time but also utilizes an electronics system that is in general more dependable.

All data were taken with a fixed beam energy and varying spectrometer fields. Both image and object slits of the beam analyzing magnet were 2.54 mm wide. Slits in

front of the target chamber were 1.27 mm in a vertical direction and 1.53 mm in a horizontal direction. The 90^{o} data were obtained with a spectrometer angular acceptance $\theta = 0.79^{o}$, $\phi = 6.56^{o}$. The $Ca^{40}(p,\alpha)K^{37}$ 150^{o} data were obtained with an angular acceptance $\theta = 1.33^{o}$, $\phi = 6.56^{o}$.

In addition to the $Ca^{40}(p,\alpha)K^{37}$ profiles, similar profiles were obtained for the elastic scattering of protons from Ca^{40}. These $Ca^{40}(p,p)Ca^{40}$ spectra (Figure 4) are analyzed in the same manner as the $Ca^{40}(p,\alpha)K^{37}$ spectra and verify the general measurement procedures.

D. SPECTRA

The spectra were obtained in the following order (with target changes indicated by asterisks): Figure 3a, *, Figure 3b, Figure 3c, Figure 4a, *, Figure 4b and Figure 4c. The target changes were made in an attempt to minimize any target deterioration that might arise from long beam exposures and to establish that no local target effects seriously affected the calculated Q-value.

In order to establish the true momentum position of the ideal rectangular step, various experimental contributions must be unfolded from each spectrum. The profile will depend on:

1) the object height, δr_s, (vertical dimension of the beam spot),

2) the collector slit width, δr_c,

3) the horizontal (θ) angular acceptance of the spectrometer and the reaction cross section variation within this angle,

4) the energy dependence of the reaction cross section,

5) the target surface conditions, e.g., contaminant layers and surface homogeneity,

6) the aberrations present under the operation conditions imposed on the spectrometer, i.e., field value, angular acceptance, and object dimensions,

7) energy dependence of the stopping cross sections in the target,

8) the variation of beam intensity across the object slits of the analyzer, and

9) current variation in the magnet.

Conversely, of course, if we knew the functions describing these contributions, the functions could be folded into each other and finally into the ideal step shape to obtain the experimental data profile. The effects of some of the above contributions are discussed by Brown, Snyder, Fowler, and Lauritsen (1951) and, in greater detail, by Bardin (1961).

In the present measurement $\delta r_c > 3M\delta r_s$ where M is the magnification, so the effect of (1) should be small compared to (2). The θ contribution originating with the

change of outgoing particle energy with angle is shown on all parts of Figures 3 and 4 and is comparable to the δr_c contribution. The Θ contribution (3) has been assumed to be rectangular, i.e., the cross section does not vary appreciably over approximately the one-degree width of the slits. Similarly, (4) has been assumed to involve a constant cross section with energy. Since these last two assumptions have not been experimentally verified, data were collected at two different laboratory angles. The frequent changes of targets has not revealed any surface effects (5) that would complicate the extraction of the step frequency from the data. Although the exact aberration contribution (6) is not known, the rounding of the upper step edge is in qualitative agreement with the elastic scattering data of Groce (1963). At the energies of the present measurement, (7) may be neglected. The scattering data of Groce (1963) and the work of Pearson (1963) yield a beam resolution function (8) that is much narrower than the width calculated from the analyzing magnet slit openings. Therefore (8) is also neglected. The contributions of (9), which are expected to be symmetric in momentum and also very small for the apparatus used, are also neglected.

In summary, it is assumed that only δr_c, Θ and aberration play important roles in the present measurement.

Further, the dominant δr_c and θ contributions are approximately symmetric in momentum, and when folded into the ideal step shape should yield a curve whose momentum at half height represents the momentum of the outgoing particle. The frequencies at half height are extracted from Figures 3 and 4 and used to calculate the Q-values discussed in Section F. A 4-kc/sec error is assigned to each frequency determination on the basis of both the statistical uncertainty of the midpoint frequency of the step and the possibility of varying asymmetrical effects leading to rounded step edges.

E. CALIBRATION

Both the 90° beam analyzing magnet (radius 86.3 cm) and the spectrometer (radius 61.0 cm) are calibrated by passing particles of known kinetic energy, E, charge Z, and mass M through the magnets. For each magnet, the parameter k in the equation (Appendix III)

$$k = \frac{E}{f^2 Z^2}\left(\frac{M}{M_p}\right)\left(1 + \frac{E}{2M}\right)$$

may be calculated from the measured magnetometer frequency, f.

The analyzer parameter, k_a, will be constant if f is proportional to the central trajectory field, B_o, as expected for the uniform field 90° analyzing magnet. Fisher

and Whaling (1964) have shown that the momentum of particles passing through the analyzing magnet is proportional to the measured field within one part in 3000 for fields corresponding to He^{4++} energies from 2.5 to 10 MeV. It is therefore necessary to measure k_a at only one field value in this range.

B is a function of radius, r, for the spectrometer. In order to measure B_o directly it would be necessary to locate the magnetometer on the central trajectory. Since this would obstruct the transmission of particles through the spectrometer, the magnetometers are located (Figure 21) at one side of the magnet gap. Unfortunately, at this position the magnetometer field deviates from the ideal relation

$$B = \left(\frac{r_o}{r}\right)^{\frac{1}{2}} B_o,$$

requiring measurements of k_s as a function of f_s.

The general calibration procedure is discussed below. As an example of this procedure the calibration curves for a wide range of f_s values are shown. These curves have been used in analysis of the Ar^{37} level spectra. The one k_s determination (at 20 Mc/sec) necessary for the Q-value determination treated in this part is presented as a special case of the general procedure.

The steps of the calibration procedure are:

1) With the standard Po^{212} source [8785.0 ± 0.8 keV

(Wapstra 1964)] at the object position, the corresponding spectrometer frequency $f_{s\alpha}$ is determined. $k_s(f_{s\alpha})$ is calculated. The peak frequency of the alpha line was used (Groce 1963).

2) With the spectrometer at zero degrees and the same spectrometer field as (1) a beam with the same momentum as the source alpha particles is admitted through the spectrometer after passing through a pinhole in a tantalum sheet which is used to define accurately the object position. Both source and pinhole are located by measuring a standard distance (7.925 cm) from the bottom of the lucite top of the target chamber. This measurement determines an analyzing magnet calibration constant, $k_a(f_{a\alpha})$.

3) Assuming analyzing magnet linearity as discussed, the spectrometer may now be calibrated by passing a known-energy beam through the pinhole and the spectrometer. This determines a unique spectrometer frequency for the unique beam energy (frequency). Since

$$\frac{f_s}{f_a} = \left(\frac{k_a(f_a)}{k_s(f_s)}\right)^{\frac{1}{2}} = \left(\frac{k_a(f_{a\alpha})}{k_s(f_s)}\right)^{\frac{1}{2}}$$

variation of the beam energy varies f_s and $k_s(f_s)$ is found for a range of f_s values.

Figure 5 shows data obtained for spectrometer frequencies from 20 Mc/sec to 44 Mc/sec; it is presented as the ratio of the two magnet frequencies found in (3), and

the Po^{212} calibration is shown in the inset.

One complication is the sensitivity of the spectrometer calibration to radial detector displacements. Fortunately, only the first step of the calibration procedure must be repeated if the detector position has been shifted from the calibrated detector position.

For a particle energy E, let f_s equal the original geometry spectrometer frequency while f_s' ($=f_s+\Delta f_s$) equals the spectrometer frequency with the detector displaced a distance Δr from the original position. Since the dispersion

$$D = \frac{\Delta r/r}{\Delta f/f}, \quad \Delta f_s = \frac{f_s}{D} \frac{\Delta r}{r} .$$

The dispersion (Appendix II) has been shown to be independent of frequency, implying that f_s'/f_s is also independent of frequency. Repetition of step (1) gives

$$\frac{f_{s\alpha}'}{f_{s\alpha}} = \frac{f_s'}{f_s} .$$

For a given particle energy E

$$k_s' = k_s \left(\frac{f_s}{f_s'}\right)^2 = k_s \left(\frac{f_{s\alpha}}{f_{s\alpha}'}\right)^2$$

Combining this expression with the original calibration gives (f_{s2} and f_{a2} are the step 2 results)

$$k_s'(f_s') = \left(\frac{f_{s\alpha}\, f_a f_{s2}}{f_{s\alpha}' f_s f_{a2}}\right)^2 k_s(f_{s\alpha})$$

Since k_s' depends on the frequency of the calibration al-

phas ($f_{s\alpha}'$), we may generate a family of k_s' vs. f_s' curves with $f_{s\alpha}'$ as a parameter. Figure 6 presents two of these curves from which the spectrometer calibration constants were obtained for other reactions to be described later.

One of the greatest advantages of the above direct beam method is that only small beams are required to carry out the calibrations. The analyzing magnet slits may be reduced to 0.62 mm from their typical settings of 3.8 mm and data are very quickly obtained.

k_s (20 Mc/sec) was determined at the same time that the value of k_a was determined for the $Ca^{40}(p,\alpha)K^{37}$ measurement. The Bi^{212} alpha line [6049.5 ± 0.7 keV (Wapstra 1964)] was used as the energy standard because its energy ($f_s \sim 23$ Mc/sec) placed it close to the 20 Mc/sec region in which Q-value spectra were collected. During the experiment only small variations in the magnet occurred in the 20 Mc/sec region. The field was recycled (0 amps to 700 amps to 0 amps to the final field of approximately 200 amps) between each spectrum.

Figure 7 shows a typical pinhole spectrum together with the B^{212} alpha line ($\theta = 1.33^{\circ}$, $\phi = 6.56^{\circ}$) used in one of the k_a determinations. Because the pinhole data are taken by counting the beam particles with a scaler for a given period of time, beam fluctuations cause variations of the data that far exceed statistical variations.

This has little effect on the accuracy of the midpoint determination because the steep sides of the trapezoidal spectra have approximately equal absolute values of slope and the precise half height position is unimportant.

Four pinhole measurements of k_a were made with three types of beam.

Beam	Source	k_a
He^{3++}	Negative ion source	.019885
He^{3++}	" " "	.019885
d	" " "	.019879
He^{3++}	Neutral injection	.019877
		.019881 average

Calibration constant uncertainties are established by assuming ±1 kc/sec uncertainties in the calibration data and combining this value with the Bi^{212} alpha energy uncertainty to give

$$k_a = (19881 \pm 5) \times 10^{-6}.$$

The average value of k_a was then used with two additional pinhole measurements to find an average k_s at approximately 20 Mc/sec.

1) k_s (20 Mc/sec) = .0113637
2) k_s (20 Mc/sec) = .0113593
average k_s (20 Mc/sec) = .0113615

and k_s (20 Mc/sec) = $(11361.5 \pm 5) \times 10^{-6}$

F. CALCULATIONS

A relativistic Q-value program for use with the spectrometer has been written by A. Bacher as a corollary

to the more general ADBKIN. The input data are the masses of the target (nuclear), ingoing, and outgoing particles; the constants of both magnets, laboratory angle, the frequencies of both magnets (f_a and f_s), and a small frequency interval specified for each magnet (Δf_a and Δf_s). The program then finds Q-values(Appendix III)for the four sets of frequencies: f_a, f_s; $f_a + \Delta f_a$, f_s; f_a, $f_s + \Delta f_s$; and $f_a + \Delta f_a$, $f_s + \Delta f_s$. These combinations of frequencies allow a simple evaluation of Q-value uncertainties since all errors may be expressed either in terms of the analyzing magnet frequency, the spectrometer frequency, or the spectrometer angle.

The contributions to the uncertainty in the Q-value are listed in Table II. The analyzing magnet slit width of 2.5 mm contributes the largest uncertainty to the Q-value. The value quoted in Table II corresponds to an uncertainty in the mean radius of $\pm \frac{1}{4}$ of the full slit width.

Current changes in the two magnets introduce an additional uncertainty. The average current over the collection interval is difficult to determine since the magnets are not monitored constantly by the experimenter. The value of this uncertainty is therefore assumed to be of the same order as the current excursions over a short period time at the beginning and end of each collection

interval.

The spectrometer angle uncertainty of 0.05^{o} is based on the track protractor measurements described by Groce (1963) and the measurement of the zero degree beam position.

The measured Q-values are:

$Ca^{40}(p,\alpha)K^{37}$	90^{o}	-5179.6 ± 9.4 keV
	150^{o}	-5178.3 ± 9.4 keV
$Ca^{40}(p,p)Ca^{40}$	90^{o}	4.2 ± 5.3 keV
	150^{o}	4.1 ± 5.3 keV

Since the beam energy differed for the two reactions, there is no justification for attempting to reduce the error by adjusting f_a to yield a zero $Ca^{40}(p,p)Ca^{40}$ Q-value (within the large beam uncertainty limits).

G. RESULT

Using the 1964 mass tables (Mattauch et al. 1965) the $Ca^{40}(p,\alpha)K^{37}$ Q-value of -5179 ± 9 keV yields a K^{37} mass excess of

-24804 ± 10 keV.

Kavanagh and Goosman's (1964) 1850 ± 11 keV Ar^{36} + p threshold value in K^{37} implies a K^{37} mass excess of

-24793 ± 11 keV.

These values compare well with each other and the mass table value of

-24810 ± 45 keV.

III. Ar^{37} LEVELS $E_x < 4.5$ MeV

A. INTRODUCTION

The work described in this section was undertaken in order to verify the low-lying levels of Ar^{37} as tabulated in Endt and Van der Leun (1962) and assumed by Bahcall (1964) in his model hypothesis for cross section calculations (see Figure 1). The resolution and background rejection features of the 61-cm spectrometer were advantageous for this study. Therefore a reaction was sought that would involve incident and outgoing charged particles with a Q-value sufficiently large that outgoing particles could be easily detected and would not be greatly hindered by the Coulomb barrier. Further, it was desirable to have a solid target--either self-supporting or mounted on a thin backing foil--with a large abundance of the target isotope. The above requirements suggest the first three of the following reactions (Q-values are from Endt and Van der Leun [1962]):

1) $K^{39}(d,\alpha)Ar^{37}$ Q = 7.862 MeV
2) $Cl^{35}(He^3,p)Ar^{37}$ = 9.582
3) $Cl^{37}(He^3,t)Ar^{37}$ = -0.834
4) $S^{34}(\alpha,n)Ar^{37}$ = -4.629
5) $Ar^{36}(n,\gamma)Ar^{37}$ = 8.794
6) $Ar^{36}(d,p)Ar^{37}$ = 6.570
7) $Cl^{37}(p,n)Ar^{37}$ = -1.599
8) $Ca^{40}(n,\alpha)Ar^{37}$ = 1.750
9) $Cl^{35}(t,n)Ar^{37}$ = 8.818

10) $Cl^{35}(\alpha,d)Ar^{37}$ Q = -8.771 MeV

11) $Ar^{36}(t,d)Ar^{37}$ = 2.537

12) $Ar^{36}(\alpha,He^3)Ar^{37}$ = -11.783

13) $Ar^{38}(p,d)Ar^{37}$ = -9.617

14) $Ar^{38}(d,t)Ar^{37}$ = -5.584

15) $Ar^{38}(He^3,\alpha)Ar^{37}$ = 8.763

16) $K^{39}(n,t)Ar^{37}$ = -9.726

17) $K^{39}(p,He^3)Ar^{37}$ = -10.491

Since none of the first three reactions listed has been used for Ar^{37} level studies, they provide independent verification of the previously established level system. Preliminary runs showed that the data could be obtained more rapidly with reaction (1) than with reactions (2) or (3). Reaction (3) involves Cl^{37} with a twenty-four per cent natural abundance, and tritons from this reaction were not observed in a brief initial exploration. The $K^{39}(d,\alpha)Ar^{37}$ reaction was used for the study of the Ar^{37} excited states below 4.5 MeV.

B. EXPERIMENTAL DETAILS

K^{39} targets were prepared by vacuum evaporation of either KBr or KI on carbon foils of approximately 50-μgms /cm^2 thickness. The carbon foils were made on microscope slides by first evaporating $BaCl_2$ and then sputtering carbon from an arc onto the $BaCl_2$ surface (Woytowich 1962). The foils were then floated off on water and mounted on tantalum holders over holes 8 mm in diameter. Potassium

halide was then placed in a tantalum boat and evaporated onto four holders placed so that the square of the distance from the boat doubled with each succeeding holder. The target thicknesses then differed by four successive factors of two, and targets of the optimum thickness could be quickly found by investigating the apparent momentum width of the ground state of Ar^{37}. There was no deterioration in targets left for a month or more in a desiccator and no deterioration was observed in the yield if the beam remained less than 0.3 μa. Beam defining slit apertures were 1.5 mm horizontally and 1.8 mm vertically. Neither halide was obviously superior to the other and targets prepared from the two halides were used interchangeably.

A 10-MeV deuteron beam was used, and the alphas were detected with the spectrometer sixteen-detector array (Appendix II). The array slits were 3.18 mm in width and the magnet angular aperture was $\phi = 6.56^{\circ}$ and $\Theta = 3.04^{\circ}$. The beam was stopped in a tantalum sheet connected to the target holder and placed at +300 volts with respect to the grounded chamber walls. The electron suppressor was placed at -300 volts with respect to the chamber walls. The spectra shown in Figure 8a were obtained with KBr targets at laboratory angles of 30° and 150°. Additional data (Figure 8b) were obtained with the same resolution using KI targets and angles of 60°, 90°, 120°, and 140° for the region of excitation between 3.5- and 4.5-MeV Ar^{37} excitation. It is

clear that increased resolution would be desirable to resolve further the doublets (multiplets) in this region. The resolution in terms of Ar^{37} excitation energy is approximately 50 keV (FWHM). Levels numbered 18 and 19 (also 20 and 21) are separated by 50 keV. The frequency and yield factors described in Appendix II were used to reduce the array data to the equivalent single particle data shown in Figure 8.

The collector slit width ($\delta r_c = 3.2$mm), one of the major contributors to the final resolution of the data, approximately equals the 2.6-mm dead spacing between detectors. Since several data points on each peak are required to determine the level positions, a given region of the survey is obtained by changing the magnetic field in steps corresponding to a 1.9-mm displacement of the image along the perpendicular to the central ray. The data of each field region spanned by the array are therefore composed of three separate spectra, slightly displaced in field. The fields of the next series of three spectra are adjusted so that the data from detector one of the first series are adjacent to the data of detector sixteen in the new series. One additional spectrum is taken after each series of three spectra with the magnetic field at an intermediate value between two series. This spectrum quickly indicates that the array is functioning properly and that the pulses from each detector are being routed correctly. Array electronic malfunc-

tions usually change the number of events detected with an individual detector by at least 50%.

The only target contaminant observed in the spectra of Figure 8 is C^{13}. The broad group at 34.5 Mc/sec in the 30^{o} spectra is the ground state of B^{11}, populated by the reaction $C^{13}(d,\alpha)B^{11}$. The Ar^{39} ground state from $K^{41}(d,\alpha)Ar^{39}$ has been observed weakly at a higher momentum than the Ar^{37} ground state, but no excited states of this reaction were observed. The isotopic abundance of K^{41} is 6.9%; K^{40} (0.01%) is the only other natural isotope of potassium. The kinematic momentum shift between 30^{o} and 150^{o} for a target mass two atomic units from K^{39} differs from the K^{39} shift by approximately 180 kc/sec (an easily detectable quantity, as seen in Figure 8). The two spectra of Figure 8a have been shifted relative to each other to align vertically states originating from K^{39} nuclei.

Table III indicates some of the factors that lead to the uncertainty assignment for the excitation energies of the Ar^{37} levels. All factors except those dealing directly with the target orientation and thickness have been discussed in the preceding section. The spectrometer calibration constants have been found in Figure 6. Peak frequencies have been used to find the Q-values of each level. These frequencies have a relatively large error assignment ($\pm$ 1/6 FWHM) because of the large statistical errors. Each ordinate mark in Figure 8 indicates 50 counts.

In addition to the uncertainties discussed above, there is a systematic uncertainty owing to small unknown energy losses of the deuterons and alphas in the halide target and the carbon supporting foil. In obtaining the 90^{o}, 120^{o}, 140^{o}, and 150^{o} data, the normal to the halide surface bisected the angle formed by the beam and spectrometer entrance. The incoming deuterons and outgoing alphas were not required to pass through the carbon foil. Although we are interested in the alpha energy from target nuclei on the front surface of the halide (the condition which involves no energy losses), alphas leave the target with a continuous energy range whose maximum corresponds to front surface target nuclei and whose minimum corresponds to back surface target nuclei.

Since the peaks in Figure 8 have base widths W, equal to the sum of all the momentum resolutions, an estimation of the target contribution, δT, may be obtained from

$$M \delta r_s + \delta r_c + \delta \Theta + \delta T = W.$$

The beam energy spread is negligible for the present case (Pearson 1963 and Groce 1963). The assumed beam size ($M\delta r_s$) may overestimate the source slit contribution to the momentum resolution since the beam may not illuminate the target uniformly over the entire vertical slit dimension (δr_s). For the ground state at 150^{o},

$$M \delta r_s + \delta r_c + \delta \Theta = 125 \text{ kc/sec and } W = 120 \text{ kc/sec}.$$

Even with the assumption $\delta r_s = 0$, the value of δT would be approximately 20 kc/sec; this would shift the peak location

approximately 10 kc/sec from the frequency corresponding to the front surface target nuclei.

The 30^{o} and 60^{o} data were taken with the normal to the halide surface at the same angle as the spectrometer entrance. The incoming deuterons pass through the carbon foil before reaching the halide target. The carbon foils were visually estimated to be approximately 50 micrograms per cm^2 thick (Cusson 1965 and Woytowich 1962). This thickness implies a 4-keV energy loss for 10-MeV deuterons (Demirlioglu and Whaling 1962). From the ratio of deuterons to alpha stopping cross sections (1/5.7), the 150^{o} data imply a maximum halide target contribution of 8 kc/sec. The total maximum systematic uncertainty for the 30^{o} and 60^{o} data is approximately 12 kc/sec.

In order to minimize the effects of the systematic and beam energy uncertainties, the average excited state Q-values found from the data of Figure 8 were subtracted from the average ground state Q-value in order to obtain the excitation energies. The ground state Q-value of Mattauch et al (1965), 7.859 ± 3 keV, agrees with the experimental ground state Q-value of 7.857 ± 17 keV; this also indicates that the effect of systematic target loss errors is small. The total uncertainty assignments adopted are 16 keV.

C. RESULTS

Table IV lists the excitation energies found in this and other work. Figure 2 shows the excitation energies

found in this work. The level density implied by the new diagram will be discussed in a following part.

No new levels having a cross section greater than one-tenth of the ground state cross section appear below 2-MeV Ar^{37} excitation energy. The only previously reported level which was not observed in the $K^{39}(d,\alpha)Ar^{37}$ spectra is the level at 2.41 MeV. This level was observed by Ferguson and Paul (1959) using the $Cl^{37}(p,n)Ar^{37}$ reaction at zero degrees but was not observed by Davies and Barnes (1964) using the same reaction at zero degrees (Part I, Section D).

The assignment of a level at 4.22 MeV is tentative since the cross section decreases in moving to a forward angle so that the target nucleus cannot be identified from the kinematic shift. This level has been established as an Ar^{37} level by Castro (1964) with the $Cl^{35}(He^{3},p)Ar^{37}$ reaction and Wiza *et al.* (1965) with the $Ar^{36}(d,p)Ar^{37}$ reaction.

IV. $K^{39}(d,\alpha)Ar^{37}$ ANGULAR DISTRIBUTIONS

A. INTRODUCTION

Calculations of the $Cl^{37}(\nu,e^-)Ar^{37}$ cross section are based on both the location of the Cl^{37} ground state analog level in Ar^{37} and the properties of Ar^{37} levels below 3 MeV excitation energy. In an attempt to learn more about the levels below 3 MeV and the mechanism of the $K^{39}(d,\alpha)Ar^{37}$ reaction, angular distributions of these levels were obtained with $E_d = 10$ MeV.

Conclusions about the properties of the low-lying Ar^{37} levels will, of course, depend on the reaction mechanism. If a compound nuclear (CN) mechanism were dominant, data might be interpreted in terms of the statistical model's $2I+1$ rule: the total reaction cross section is proportional to $2I+1$, I the final nucleus spin. Successful interpretation would yield spin assignments for the Ar^{37} levels below 3 MeV.

If the direct interaction (DI) mechanism were dominant, it would be difficult to extract information. In general, determination of the angular momentum transferred by the proton and neutron does not uniquely specify the spin of the final state. A spectroscopic factor, S, may be extracted from the magnitude of the cross section: S is defined by

$$\frac{d\sigma}{d\Omega} = F(\theta, Q, L, Z, R)S(i,f)$$

(θ = scattering angle, Q = reaction Q-value, L = momentum trans-

fer, Z = target charge, R = target radius, and i and f, properties of the initial and final states.) The theoretical evaluation of S has been discussed formally by Yoshida (1962) and in a more qualitative fashion by Bromley (1964). The two-particle spectroscopic factor has not, as yet, been widely used as a tool of nuclear spectroscopy.

If a DI mechanism is established, there is reason to expect that isotopic spin will be conserved in the $K^{39}(d,\alpha)Ar^{37}$ reaction. Since the ground state of K^{39} has $T=\frac{1}{2}$, only $T=\frac{1}{2}$ states in Ar^{37} will have large cross sections. Both $T=\frac{1}{2}$ and $T=3/2$ Ar^{37} levels are expected to be formed in the $Cl^{35}(He^3,p)Ar^{37}$ reaction, and comparison of the $Cl^{35}(He^3,p)Ar^{37}$ and $K^{39}(d,\alpha)Ar^{37}$ level schemes might indicate the excitation energy of the lowest $T=3/2$ Ar^{37} level. This consequence of a DI mechanism is discussed in more detail in Part V.

B. EXPERIMENTAL DETAILS AND RESULTS

The scattering chamber described by Harrison and Whitehead (1963) was used in obtaining the $K^{39}(d,\alpha)Ar^{37}$ angular distributions. The data were collected with a single Molechem solid state detector (n-type 6500 ohm-cm nominal resistivity). The bias value of 60 volts (300 microns depth) was determined by the requirement that the detector be thick enough to stop completely 20-MeV alpha particles, yet not so thick that proton and deuteron energy losses are large enough to cause pile-up background in the alpha energy

region of interest. The detector was fixed to the movable arm and was approximately 7.9 cm from the beam spot on the target. A 0.5-mm thick tantalum collimator with a rectangular opening (0.76 mm parallel to the detector-beam plane by 4.8 mm) was located on the movable arm approximately 7.25 cm from the beam spot. Another 0.5 mm thick collimator with a rectangular opening (4.8 mm parallel to the detector-beam plane by 7.9 mm) was located on the arm approximately 2.1 cm from the beam spot. This second collimator eliminated the possibility of detecting beam scattered from the beam catcher or defining slits.

A target of KBr on carbon foil, prepared in the manner described in Part III, was used in determining the angular distributions. Gold backing foil created severe background at forward angles, dictating the use of carbon target backings. The KBr surface was oriented at 40^{o} to the beam direction so that it was facing the incoming 10-MeV deuteron beam (Figure 9). The shaded areas of Figure 9 indicate the portions of the quadrants in which data were taken at every 5^{o} laboratory angle from $\theta_{lab} = 165^{o}$ to 20^{o} with the exception of $\theta_{lab} = 25^{o}$.

Figure 10 shows one of the spectra from which the relative differential cross sections for the lowest six Ar^{37} levels were extracted. A target thickness was selected that would enable the first two excited states to be barely

resolved. The kinematic energy spread owing to the finite entrance aperture ($\Theta = 0.60^{o}$) is 20 keV at 90^{o}; the first two Ar^{37} excited states are separated by 120 keV. Thus the target thickness (and ΔE_d) is on the order of 100 keV. This large target thickness resulted in a correspondingly high count rate and also served to increase the spread of incident deuteron energy. Assuming statistical model validity, the corresponding spread of excitation energies in the compound nucleus means that the angular distributions should show less fluctuations and possibly better $2I+1$ rule validity.

The angular distributions were obtained with no change of target position. A monitor detector was placed at approximately $\theta_{lab} = 60^{o}$. In principle the data from each angle could be normalized by the monitor detector yield. Unfortunately, a large changing background was present in the home-made monitor detector and it was not used in the final data reduction. Two other experimental aspects must be considered. First, if the target is inhomogeneous, a change in the illumination of the beam area defined by the beam slits (0.9 mm by 0.9 mm) may imply a change in the relative cross section from one angle to another. The most probable source of target inhomogeneity will be target deterioration under excessive beam current. Second, as the more forward angles are observed, the dead time increases, owing to increased

proton and deuteron yields. This increase produces a larger electronic dead time.

Figure 11 shows the angular distributions for the first six Ar^{37} levels. The ordinate of each of the six plots is the same; each tick mark represents approximately 100 counts per 430 microcoulombs (a correction has been made for the lab to center-of-mass cross section conversion). The data were taken in the following order: Θ_{lab} = 160, 150, 140, 130, 120, 110, 100, 90, 80, 70, 60, 50, 40, 30, 20, 155, 165, 145, 135, 125, 115, 105, 95, 85, 45, 55, 65, 75, and 35 degrees.

With the exception of the first angle, 160^{o}, where a larger number of counts appears than at adjacent angles, there is no yield variation outside statistics that could be attributed to target deterioration or to beam shift between the first and second halves of the data angles investigated. Therefore in the backward hemisphere the error bars represent only statistical (including background estimation and subtraction) uncertainties. Determination of the forward hemisphere error bars is complicated by analyzer dead time losses. At 20^{o} the RIDL 400-channel analyzer meter dead time was ~25%, at 30^{o} ~18% and at backward angles ~2%. The error bars at forward angles are based on two independent uncertainties: the statistical uncertainty and the dead time uncertainty (assumed to be one-half of the meter reading).

The open circles in Figure 11 indicate one further experimental uncertainty. The kinematic behavior and cross section of an unidentified contaminant group have been determined. In all cases (open circle points) the presence of this group increases the uncertainty of the subtracted background less than a factor of two.

C. DISCUSSION

The experimental data are discussed both in terms of the two reaction mechanisms (CN and DI) and of the spectroscopic information that one dominant mechanism might reveal. With respect to a dominant CN mechanism, which is considered first, it is reasonable to expect validity of the $2I+1$ rule.

Assuming a CN mechanism, Bethe (1937) pointed out that when the energy levels of the CN are sufficiently dense, the cross section for a reaction to a particular final state, f, is proportional to the average partial width of the compound levels for decay to the particular final state, and he writes

$$\Gamma_f \sim (2I_f + 1) E \xi_f$$

where E is the kinetic energy of particles emitted to the state f and ξ_f is the "sticking probability," a quantity which Bethe assumes to vary slowly with the energy E. The so-called $2I+1$ rule follows from the assumption that $E\xi_f$ is independent of f, and Bethe notes that this assumption is

best justified when one compares final states that differ little in energy. The 2/1 intensity of the proton groups to the ground and first excited states in the reaction $Li^6(d,p)Li^7$ is cited by Bethe as evidence for this rule.

The conditions under which the $2I+1$ rule approximation should hold have been recently discussed in greater detail by Ericson (1960) and MacDonald (1962). These conditions have been summarized by Hansen et al.(1964) as:

> "1) The reaction mechanism should be compound nucleus formation.
> 2) The bombarding conditions should be such that a large number of compound states are excited and the spin J of these states should satisfy the condition $J > I$.
> 3) The energy of the outgoing particles should be large enough to ensure that barrier penetration does not suppress any ℓ-values feasible with J and I.
> 4) The cross sections $\sigma(I)$ should be averaged over 'sufficiently' many compound states in order to destroy any special correlation that may exist between the compound states and the final states."

It is difficult to make more quantitative statements and estimates of the $2I+1$ rule validity. For most (d,α) reactions a beam energy of 5 MeV will ensure the presence of conditions (2), (3), and (4); the compound nucleus will be excited to a region with overlapping levels. Specifically, if a CN description of the $K^{39}(d,\alpha)Ar^{37}$ reaction is valid, then description in terms of the $2I+1$ rule should be valid for the excitation energy with which we are dealing.

Dominance of a particular reaction mechanism may be treated qualitatively in terms of the reaction time scale.

The CN mechanism implies an intermediate state lifetime long enough so that statistical equilibrium among all possible nuclear excitation modes may be reached. The DI mechanism, on the other hand, implies a correlation between the incident and outgoing particles; the incident particle undergoes a reaction with a small group of target particles (or a single target particle) and the particle(s) with sufficient energy promptly leave the nucleus, undergoing no further particle interactions. The CN mechanism is therefore associated with long intermediate state lifetimes, while the DI mechanism is associated with short lifetimes. Generally, as the excitation energy of the intermediate system is increased, the nuclear lifetime, $\tau = \hbar/\Gamma$, decreases, and therefore reactions through highly excited intermediate nuclei will proceed via the DI mechanism. Reactions through much lower excitation energies will be characterized by a dominant CN mechanism.

It is difficult, however, to predict which (if either) reaction mechanism will dominate the $K^{39}(d,\alpha)Ar^{37}$ reaction with 10-MeV incident deuterons, i.e., which of the reaction mechanisms will be valid for a 24-MeV excitation energy in the Ca^{41} intermediate nucleus. In an attempt to examine further the problem of the expected reaction mechanism, a digression is made to summarize the results of the two most extensively studied (d,α) reactions carried out on

nuclei with $20 \leq A \leq 40$.

The $Al^{27}(d,\alpha)Mg^{25}$ reaction was first studied from the $2I+1$ point of view by Sheline et al. (1959). These authors observed the alpha products only at 130^{o} and with two bombarding energies $E_d = 7.5$ and 8.5 MeV. Assuming isotropic angular distributions they divided each "cross section" by $2I+1$ (twelve Mg^{25} levels with known spins were utilized) and, after correcting for the alpha penetrability, found values with a rms deviation of 33%. The uncertainty of the 130^{o} yield values was claimed to be 15%. Since the appearance of this paper, there has been a considerable effort, not only to measure accurate cross sections for $2I+1$ purposes, but also to investigate more generally other predictions (such as cross section fluctuations and symmetry of angular distributions about 90^{o} after averaging over various E_d intervals) of a statistical compound nuclear model.

Cassagnou et al. (1963) have studied in detail fluctuations appearing in angular distributions and excitation functions from $E_d = 2$ to 10 MeV ($E_d = 6.5$ MeV corresponds to 24-MeV Si^{29} excitation energy). Ericson's predictions of fluctuating cross sections and symmetric energy-averaged angular distributions are well verified for the range of E_d from 2 to 5 MeV. Compared to the 5-MeV data, the 10-MeV data show angular distributions that have:

1) increased similarity of shape for all alpha groups

2) an increased tendency toward forward and backward

peaking ("U"-shape)

3) less marked symmetry about 90^{o}.

The conclusion of Cassagnou et al. is that the $E_d = 10$ MeV results do not preclude a DI contribution and that their data are of insufficient precision either to confirm or deny the Ericson fluctuation predictions.

Other authors (Hinds et al. 1961, MacDonald 1962, Hansen et al. 1964, Gadioli et al. 1964, Abuzeid et al. 1964, Jahns et al. 1964, Naqib et al. 1965, and Cosper and Johnson 1965) have analyzed their $Al^{27}(d,\alpha)Mg^{25}$ data in terms of the $2I+1$ rule. The spirit in which the $2I+1$ rule is tested for the determination of unknown spins is indicated by MacDonald's implication that spin determinations with uncertainties less than one unit are unlikely with the $2I+1$ rule, even under the most favorable conditions. Using this criterion, the rule holds for the data from $E_d = 1.4$ to 14.7 MeV, including the $E_d = 14.7$ MeV data of Yanabu et al. (1962), which was analyzed in terms of a DI mechanism. The $2I+1$ rule has, then, worked admirably with the $Al^{27}(d,\alpha)Mg^{25}$ reaction, even at a bombarding energy high enough that good PWBA fits may be obtained from the DI mechanism.

A quantitative examination of this $2I+1$ rule as a function of deuteron energy is possible by evaluation of $\sigma/2I+1$, the cross section divided by $2I+1$. The following table lists the experimenters, deuteron energy range, and rms deviation from the average $\sigma/2I+1$ for the lowest five

Mg^{25} levels.

Experimenters	E_d(MeV)	$\sigma/2I+1$ (%)
Gadioli et al.	1.4-2.3	9-T
Abuzeid et al.	1.5-2.5	9-T
Jahns et al.	2.4-2.6	17-T; 17-B
Hansen et al.	3.5-3.8	19-T
Naqib et al.	5.3-6.5	10-T
Cosper and Johnson	9.3	6-T; 18-B; 6-CN
Hinds et al.	10	22-T; 12-B
Yanabu et al.	14.7	40-T; 27-B

In the right hand column, T is the total cross section, either for all angles measured or for 0° to 180° using extrapolations; B is the cross section integrated over the backward hemisphere; CN is the so-called compound nuclear cross section. The latter is an attempt to decompose the angular distributions into incoherent DI and CN parts--the CN part is assumed to be isotropic with a differential cross section equal to the minimum of the measured differential cross section. This decomposition procedure has been used extensively by the Purdue group (Cosper et al) in analyzing (d,α) reactions. The practice of using only the cross section integrated over the backward hemisphere is common at bombarding energies where there is a large DI contribution to the cross section. The argument is that since the DI mechanism contributes a relatively larger (forward peaked) cross section to the forward hemisphere, the backward hemisphere cross section will represent more accurately the CN contribution to the cross section.

As the bombarding energy is increased, the table indi-

cates poorer $2I+1$ agreement. This is not totally unexpected in view of the idea of an increasing DI contribution and lack of a $2I+1$ term in the plane wave pickup theory (Butler 1957).

A further point of interest is the effect of corrections upon simple $2I+1$ cross section proportionality (Ericson 1960 and MacDonald 1962). Abuzeid et al. have made a correction for the alpha penetrability (condition 3 of Hansen) and obtain results very similar to those of Gadioli et al., who make no apparent cross section correction (both have 9% rms deviations). MacDonald (1962) has made corrections for the $E_d = 10$ MeV data of Hinds et al. with little or no improvement in the $2I+1$ agreement.

Jänecke (1963) has extensively investigated the $Ca^{40}(d,\alpha)K^{38}$ reaction with $E_d = 7.7$ MeV (18.2 MeV in Sc^{42}). His experiment provides some basis for decomposition of the cross section into DI and CN parts as described above. From the statistical theory he has computed the cross sections to the lowest five levels in K^{38}. These cross sections are normalized to the nearly isotropic ($J^\pi = 0^+, T = 1$) level data with the assumption that isotopic spin rules are completely violated via the CN mechanism and no DI contribution is present (i.e., the isotopic spin rule is completely conserved in the DI case). The CN cross sections thus calculated for the $T = 0$ K^{38} levels (where the DI mechanism is "allowed") yield differential cross sections approximately

equal to the minimum of the measured differential cross section. Attributing the difference between the actual cross section and the calculated CN cross section to a DI cross section, he finds that typically two-thirds of the reaction cross sections proceed by the DI mechanism. At $E_d = 14.8$ MeV Micheletti and Mukherjee (1965) found that the ground state cross section plotted against the momentum transferred agrees well with the $E_d = 7.7$-MeV data; they discuss their data in terms of a predominant pickup mechanism.

Jänecke suggests that the DI dominance of the $Ca^{40}(d,\alpha)K^{38}$ reaction at a bombarding and excitation energy lower than that of the $Al^{27}(d,\alpha)Mg^{25}$ reaction is a result of even (or self conjugate) target nuclei cluster configurations that favor DI (d,α) reactions. Because of the fragmentary nature of work on other reactions it is not possible on the basis of previous experimental results to predict what reaction mechanism will be exhibited by the $K^{39}(d,\alpha)Ar^{37}$ reaction with $E_d = 10$ MeV.

In discussing the $K^{39}(d,\alpha)Ar^{37}$ data of Figure 11 it is apparent that the general shape of each of the angular distributions is forward peaked. Although the statistical model predicts symmetrical distributions about 90° when data from a sufficiently broad range of bombarding energies are averaged together, the $E_d = 10$-MeV $Al^{27}(d,\alpha)Mg^{25}$ data of Hinds et al. and Cassagnou et al., though generally unsymmet-

rical and forward peaked, still have cross sections that show $2I + 1$ proportionality. The $E_d = 14.7$-MeV angular distributions of Yanabu et al. are qualitatively very similar to the $E_d = 10$-MeV $K^{39}(d,\alpha)Ar^{37}$ angular distributions. It is interesting to compare the rms deviation of $\sigma/2I + 1$, using the four Ar^{37} levels of known spin and the cross sections from Figure 11, with the table of $Al^{27}(d,\alpha)Mg^{25}$ results:

Ar^{37} Level	Spin	σ_T	$\frac{\sigma_T}{2I+1}$	σ_B	$\frac{\sigma_B}{2I+1}$	σ_{CN}	$\frac{\sigma_{CN}}{2I+1}$
g.s.	3/2	147	36.8	46	11.5	44	11.0
1.4	1/2	155	77.5	40	20.0	38	19.0
1.6	7/2	87	10.9	37	4.6	28	3.5
2.2	-	181	-	58	-	50	-
2.5	3/2	68	17.0	26	6.5	22	5.5
2.8	(5/2)	518	86.4	106	17.7	110	18.3

The results for the standard deviation of $\sigma/2I + 1$ are: 73%-T; 56%-B; and 62%-CN.

There appears to be no experimental support for the $2I + 1$ rule at $E_d = 10$ MeV for the $K^{39}(d,\alpha)Ar^{37}$ reaction. Rawlins, Riley, and Shin (1964) have also investigated the $K^{39}(d,\alpha)Ar^{37}$ reaction (at $E_d = 3$ to 4 MeV). Although they find "marked fluctuations" in the excitation functions, they find some forward peaking. There appears to be no possibility of applying the $2I + 1$ rule since the results of integrating yields over the backward hemisphere are consistent with a spin of 3/2 rather than the known (Rosner and Schneid 1965) 7/2 for the 1.6-MeV level.

The forward peaking of the six lowest Ar^{37} levels and

failure of the 2I+1 rule indicates that a DI mechanism is dominant at E_d =10 MeV for the $K^{39}(d,\alpha)Ar^{37}$ reaction. Although both PWBA and DWBA (d,α)reaction calculations have been made, the theory of (d,α) DI mechanism reactions is not as well explored, or as well tested experimentally, as the one-particle transfer reactions.

In principle, fitting experimental (d,α) DI data will determine ℓ_{n+p} , the angular momentum of the proton and neutron transferred in the reaction. Only pickup is treated since it is experimentally difficult to distinguish between the pickup and knockout mechanisms (Pellegrini 1961). Even if it were possible to determine ℓ_{n+p}, the $3/2^+$ K^{39} g.s. spin and parity and the two-particle transfer make it possible for a given ℓ_{n+p} momentum transfer to form a variety of J values in Ar^{37}. Conversely, a given J^π Ar^{37} level may be formed by more than one ℓ_{n+p} value. This is shown in the following table of permitted ℓ_{n+p} values for assumed J^π values.

J^π	ℓ_{n+p}	J^π	ℓ_{n+p}
$1/2^+$	0,2	$1/2^-$	1,3
$3/2^+$	0,2,4	$3/2^-$	1,3
$5/2^+$	0,2,4	$5/2^-$	1,3,5
$7/2^+$	2,4,6	$7/2^-$	1,3,5

Jänecke's (1963) data on the $Ca^{40}(d,\alpha)K^{39}$ reaction supports his qualitative argument predicting the enhancement of high ℓ_{n+p} values. This argument states that since the DI mechanism is primarily a surface reaction and

$L \sim k\, r_o$ (L is the angular momentum, k the momentum, and r_o the nuclear radius), $L_\alpha \sim 6$ and $L_{n+p} \sim 3$. But the transferred $\underline{\ell}_{n+p} = \underline{L}_\alpha - \underline{L}_d$, so $\ell_{n+p} \sim 3$ is the smallest favored transferred angular momentum. It is difficult to determine unambiguously high ℓ_{n+p} values by either PWBA or DWBA methods, even with single particle pickup, and, as shown in the table, a unique ℓ_{n+p} value will not uniquely determine the final state J^π. No work has been reported as yet on J-dependent DWBA two-particle DI theory.

D. CONCLUSION

The experimental $K^{39}(d,\alpha)Ar^{37}$ angular distributions at $E_d = 10$ MeV give no support for the $2I+1$ rule. A DI reaction mechanism appears likely in view of the forward peaking and $2I+1$ rule failure. No conclusions are made with regard to the spin and parity of the astrophysically interesting 2.8-MeV Ar^{37} level.

V. A SEARCH FOR THE LOWEST Ar^{37} T = 3/2 LEVEL; Ar^{37} LEVELS 4.5 < E_x < 5.9 MeV

A. INTRODUCTION

The important role of the lowest Ar^{37} T = 3/2 level in the determination of the $Cl^{37}(\nu, e-)Ar^{37}$ cross section is indicated in Part I. The part that follows is a description of a search for this Cl^{37} ground state analog level in order to determine its Ar^{37} excitation energy. A dominant DI mechanism implies probable isotopic spin rule validity for the $K^{39}(d,\alpha)Ar^{37}$ reaction. Therefore, only T = $\frac{1}{2}$ levels will be strongly populated. The $Cl^{35}(He^3,p)Ar^{37}$ reaction will populate both T = 3/2 and T = $\frac{1}{2}$ levels in Ar^{37}. If the $Cl^{35}(He^3,p)Ar^{37}$ spectra reveal all the $K^{39}(d,\alpha)Ar^{37}$ spectra levels plus one additional level near the predicted T = 3/2 level position, the additional level may be the T = 3/2 level sought. Facets of the straightforward procedure described above will be expanded in the discussion.

B. $K^{39}(d,\alpha)Ar^{37}$ EXPERIMENTAL DETAILS

The experimental work described in this section is the extension of the spectra of Part III (Figure 8) to higher excitation energy. E_d is 11 MeV and the analyzing magnet slits are 3.81 mm. Because the level density rapidly increases with excitation energy, increased experimental resolution is required to investigate the 4.5 to 5.5 MeV excitation energy region.

The table below lists some of the experimental details.

θ_{lab} (degrees)	θ_{cm} (degrees)	$\Delta\phi$ (degrees)	$\Delta\theta$ (degrees)	Resolution (~keV FWHM)
18.8	20.0	6.56	1.60	30
28.2	30.0	6.56	1.60	30
37.7	40.0	6.56	1.50	30
66.5	70.0	6.56	1.50	40
106.4	110.0	6.56	1.50	40
137.4	140.0	6.56	1.50	40

To obtain increased resolution, the data were collected with the 1.8-mm array slits (described in Appendix II) rather than the 3.2-mm slits previously used. The beam defining slits form a 1.5-mm square aperture.

The ordering of frequencies, f_s, in the data collection process is the same as for the data of Ar^{37} levels below 4.5 MeV. The use of higher resolution for the present data means that a larger number of exposures must be made in order to span the 2.6-mm focal plane region between detectors. Only one series of exposures is necessary since the array conveniently covers the regions between 4.5- and 5.5-MeV Ar^{37} energy at one frequency setting. Within this series there are eight (110° and 140°) or nine (20° to 70°) exposures separated by the same frequency interval. Because of the low counting rate three separate series were obtained with approximately 150, 450, and 450 microcoulombs of beam at 40°, 70°, 110°, and 140°. At 20° and 30° single 450 microcoulomb beam exposures were made.

Targets were prepared and selected as discussed in Part III Section B for the data of the last four angles given. KBr was used for the 40^{o} and 140^{o} data; KI for the 70^{o} and 110^{o} data. KBr was used for the 20^{o} and 30^{o} data with commercial gold leaf substituted for the carbon backing. As in the previously described work, the targets were oriented so that for spectrometer angles less than 90^{o} the beam passes through the backing before reaching the halide material. For angles greater than 90^{o} the halide surface was toward the beam and the "reflection" geometry was utilized. Carbon backings were unsatisfactory for the 20^{o} and 30^{o} spectra because contaminant peaks due to the reactions $C^{13}(d,\alpha)B^{11*}$ (2.14 MeV) and $O^{16}(d,\alpha)N^{14}$ (ground state) obscured the portion of the Ar^{37} excitation region above 5.2 MeV. The magnitude of the contaminant peaks was reduced by the use of gold backings. Since the gold backing precludes the use of a monitor detector (Part IV) a separate method was devised to obtain relative cross sections for the angles observed. At each of these angles it is noted (Figure 12) that the data appear to be free from major contaminants in the region between 4.5 and 4.8 MeV. There appear to be three levels in this region that are well separated from neighboring Ar^{37} levels (Figures 8 and 12) as well as from contaminants. The following procedure was carried out in a relatively short time with approximately 400 microcoulomb beam charge exposures.

With the 3.2-mm slits and a series of four exposures, spectra between 4.3 and 5.0 MeV were obtained for each angle. The yield between approximately 1 and 3 MeV Ar^{37} excitation energy was measured with a solid state monitor detector located at approximately 120^{o} to the beam axis.

The order of data collection was: 20^{o}, 30^{o}, 40^{o}, 70^{o}, *, 110^{o}, 140^{o}, *, 20^{o} (the asterisks between angles represent rotation in target position relative to the beam position). The forward hemisphere data were obtained with the KI surface toward the beam (the carbon surface toward the spectrometer) and the target plane approximately 45^{o} to the beam. The backward hemisphere data were obtained with the KI surface toward the beam in the usual "reflecting" geometry and the plane of the target approximately 35^{o} to the beam axis. The usual beam-stopping tantalum sheet was replaced by a sheet of tantalum bent in such a manner that a part of the sheet extended toward the center of the chamber and prevented the monitor detector from detecting events occurring during the beam-stopping process. The yield at each angle was normalized to the average monitor detector yield of the four exposures, and the final high resolution data were normalized in turn to this adjusted yield. The last 20^{o} series was obtained with only the approximate target plane angle of the first 20^{o} series. The yield per unit monitor count from the two 20^{o} series

agreed, however, to 3.3%.

The data obtained at the six angles are shown in Figure 12. The ordinate scales indicate the same relative cross sections for the plots at each angle. Typical error bars indicate the statistical uncertainties; ordinate tick marks indicate fifty counts. The excitation energies of the observed levels appear in Table IV. These energies are evaluated as described in Part III. The $E_d = 10$ MeV data uncertainties are also applicable to these data (only a 5% increase in beam frequency accompanies a 10% increase in beam energy); the final uncertainty is assumed to be 16 keV. In calculating the excitation energies, the ground state Q-value was assumed to be the 7.859-MeV value of Mattauch et al.(1965) since the ground state was not investigated in obtaining this data. The high resolution data yield excitation energies that exceed the low resolution values by -12, -8, and 19 keV for the 4.58, 4.63, and 4.75 MeV levels respectively (the only levels appearing in both sets of data). In view of the difficulty of determining the peak frequencies for the low resolution data, the high resolution data values alone are tabulated.

For each of the six angles the spectra were decomposed into eleven levels with characteristic shapes. Successful hand-calculated decomposition was possible when isosceles triangle shapes with rounded tops and the same FWHM for each level were assumed. The FWHM for each angle

separately is the average FWHM found in a preliminary data decomposition of each spectrum; this procedure left the peak height as a free parameter. The results are plotted in Figure 13 (after the usual laboratory to center-of-mass cross-section conversion). This figure shows the trends of the angular distributions. Typical error bars are based on the statistical errors of the number of counts in each peak (including background correction) and an independent 10% error for the error in the relative yields at each angle. The 10% value is determined primarily by the background subtraction involved in the low resolution normalizing angular distribution.

Inspection of the six spectra indicates the possibility of three unexplained groups at 20^{o}, two at 30^{o}, and one at 140^{o}. Only two of these groups are consistent with a K^{39} target nucleus, i.e., the groups at 20^{o} and 140^{o} (labeled number 27) that occur at approximately 5.14-MeV Ar^{37} excitation energy. On the basis of the data of Figure 12, no claim could be made concerning the existence of a level at this energy. In view of the results of the next section, however, it is interesting to plot on Figure 13 the 20^{o} and 140^{o} cross sections as well as upper limits for the cross section at other angles of a possible level at 5.14 MeV. For comparison purposes these cross sections are added (open circles) to the data plot for the weakest

of the eleven levels (4.89 MeV). The other unexplained groups occurring at 20^{o} and 30^{o} may be contaminant groups arising from the gold backing foil.

C. $Cl^{35}(He^{3},p)Ar^{37}$ EXPERIMENTAL DETAILS

The experimental aim of the work described in this section is to obtain spectra at several angles of the 5.0 MeV Ar^{37} excitation energy region with the $Cl^{35}(He^{3},p)Ar^{37}$ reaction. Two experimental techniques differ from those described in the preceding parts:

1) isotopically enriched targets were used, and

2) emulsions replaced the focal plane array of solid state detectors.

A brief preliminary investigation showed that $BaCl_2$ vacuum-evaporated on gold leaf could serve as satisfactory targets. Some beam deterioration of the target may have been present with a 0.3 μa beam of 10-MeV He^{3++}. Because of the large level density in Ar^{37}, Ar^{39} groups from the 24.5% natural abundance of Cl^{37} might have complicated the spectra severely. For this reason $BaCl_2$ enriched to a claimed 98.6% of Cl^{35} was obtained from Oak Ridge National Laboratory. In order to conserve the enriched isotope, the target-making procedure and testing of the emulsion system were carried out using natural $BaCl_2$.

The major problem encountered during target manufacture was breakage of the backing foils during the evapora-

tion process. The obvious solution, moving the foils farther from the "boat," was not satisfactory since it wasted $BaCl_2$. Thin carbon foils were not sufficiently strong to withstand evaporation (although this backing material was eliminated earlier because of the $C^{12}(He^3,p)N^{14}$ ground state contaminant). Commercial gold leaf was unsatisfactory since it was not homogeneous and failed repeatedly during the evaporation process. Gold foil is easy to prepare, however, by evaporation of a gold shaving from a bent tungsten wire onto microscope slides that have been previously coated with thin layers of $BaCl_2$ by evaporation (similar to the preparation of carbon backing foils). The $BaCl_2$ acts as a release agent and the gold foil floats free from the slide as the $BaCl_2$ dissolves. The foil is mounted on 2.5-mm tantalum holders with 8-mm diameter holes and secured with Glyptal.

In order to reduce the heating of the foil during evaporation, shields with 8- and 10-mm holes were placed over the tantalum boat which holds the $BaCl_2$ target material. This arrangement and the shape of the boat are shown in Figure 14. To make the boat, a 4.75-mm steel ball bearing is placed on a 0.5-mm tantalum sheet which is in turn placed on a lead block resting on the base of a hydraulic press. The ball is pressed into the soft lead (and the tantalum) by a steel block placed under the upper movable plate of the press. The tantalum material on two sides of

the depression is removed with a punch so that the depression is preferentially heated when a current is passed through the sheet.

Four targets are prepared simultaneously with one $BaCl_2$ evaporation. Two targets are placed 2.5 cm from the boat and the other two targets 3.5 cm from the boat. The geometry is such that the four target holders intercept virtually all the $BaCl_2$ that passes through the heat shields. Three enriched $BaCl_2$ evaporations, using 15, 15, and 20 mg of $BaCl_2$, were undertaken during the course of the experiment. None of the foils ruptured during the evaporation process.

Selection of target thickness was made using natural $BaCl_2$ and the detector array with 3.2-mm slits. The FWHM of an Ar^{37} level was measured using a thick target (so that the target thickness contribution dominated the FWHM value). The thickness desired for high resolution work was calculated as a fraction of the known thick target thickness. When identical evaporation geometries were used, the target thickness was assumed proportional to the weight of $BaCl_2$ evaporated. This assumption was verified by observing the yields from two different evaporations of known weight that produced targets thin in comparison to the slit resolution. The yield ratio of the two targets was within 15% of the weight ratio. The assumption was verified for samples of enriched and natural $BaCl_2$.

An 11.5-MeV He^{3++} beam was used to obtain data at the laboratory angles 10^{o}, 20^{o}, 30^{o}, and 80^{o} with natural $BaCl_2$ targets and 30^{o}, 40^{o}, 60^{o}, 80^{o}, and 150^{o} with enriched $BaCl_2$ targets. The spectra obtained for the last seven angles comprise Figures 15 and 16. For the natural target data and approximately one-half the 30^{o} and 80^{o} enriched target data, the analyzing magnet slits were 3.81 mm, and both the horizontal and vertical beam defining slits in front of the target chamber were 1.0 mm. These slits were reduced to 2.54, 1.0, and 0.8 mm respectively for the remainder of the enriched target data with no apparent increase in resolution. The resolutions in keV (FWHM) are approximately 25 keV for 30^{o}, 40^{o}, and 150^{o} data, 30 keV for the 60^{o} data and 35 keV for the 80^{o} data. All the data were obtained with spectrometer angular apertures of $\theta = 1.04^{o}$ and $\phi = 6.54^{o}$. An attempt was made to equalize the target thickness resolution and the angular aperture resolution. The approximate integration charges for natural Cl targets were 3000 μc for 10^{o}, 20^{o}, and 30^{o} and 13,500 μc for 80^{o}. For the enriched Cl^{35} targets the charges were 11,300 μc for 30^{o}, 13,500 μc for 40^{o}, 18,900 μc for 60^{o}, 14,400 μc for 80^{o}, and 24,800 μc for 150^{o}. Because of the problem of target deterioration, the beam current remained less than 0.2 μa.

The Ar^{37} level spectra were obtained with 2.54-cm x 15.2-cm x 100-micron Ilford K-2 emulsions located in the

spectrometer focal plane. The emulsion holder rotates to accommodate three emulsion plates, and two exposures may be made on each plate. Holder design and construction were supervised by R. Miller. Although the $Cl^{35}(He^{3},p)Ar^{37}$ spectra served as the first extensive test of this system, the developing and scanning procedure is straightforward enough so that no data were lost.

Scanning was carried out with an oil immersion lens; the number of events in successive 1/3-mm strips across the width of the plate was mentally summed, then written down at the end of each scan. Throughout the fourteen or fifteen days devoted to scanning, the scanning speed increased without reaching a plateau. After a week of scanning it was possible to scan approximately 15 cm of exposed plate per day. In the final form of the spectra (Figures 15 and 16), the data were summed to yield 2/3-mm steps along the abscissa. A 0.15-mm Al foil in front of the emulsions simplified scanning by eliminating tracks other than those caused by the passage of protons or deuterons. The deuterons were easily recognized by their shorter track lengths.

If the emulsion scheme is to be used extensively to detect protons in the future, a more sensitive emulsion than K-2 might be advisable, to increase the scanning speed. Reaction protons are easily distinguished from background events by their uniform angle of entrance and range, and

could be counted more rapidly with a denser track (as was seen in counting the dense alpha tracks in Po^{212} alpha exposures).

The major disadvantage of emulsion work is the scanning process. Although it is admittedly tedious, there is a definite advantage for high resolution work, i.e., the ability to collect all the data for a complete spectrum at one time. A prohibitive number of detectors is required to duplicate the data recorded by a single emulsion. For the sixteen-detector array, comparable resolution requires at least eight separate exposures. Target deterioration and/or contaminant build-up is often important over such long beam exposure times. Another consideration is that the sum of emulsion exposure time plus developing and scanning time is often far less than array exposure time.

The general approach to the extraction of excitation energy values from emulsion spectra is indicated in Appendix II. From the data of Table VII (Figure 24), the emulsion frequency factors are plotted versus plate distance (in the natural units of 2/3 mm). For each peak position, the frequency factor is then graphically obtained both for the observed plate distance and for this distance plus 2.5 distance units. The frequencies are then calculated and inserted into the Q-value computer program previously described. The result of this procedure is, therefore,

equivalent to both single detector data and array data analysis (with the additional possibility of observing the effect of emulsion plate position shift along the focal plane).

The uncertainties of excitation energy assignments are listed in Table III. The only new factors in this table are associated with the possible plate position shift. The $Cl^{35}(He^3,p)Ar^{37}$ spectra were collected for the purpose of observing the relative spacing of Ar^{37} levels. It was later evident that a plate with Po^{212} alpha exposures could serve as an absolute calibration if reasonable errors were allowed for any relative position shift between the data plate and the calibration plate. The positioning uncertainty may be separated into three parts:

1) the uncertainty of holder position relative to the vacuum box (0.6 mm)
2) the uncertainty of locating the data plate (1 mm)
3) the uncertainty of locating the calibration plate (1 mm).

For exposure, the plates were placed in the grooved holder (grooves along the 15-cm sides), pushed firmly against a brass stop, and secured with set screws. The scanning origin was the end of the plate at the stop. Since some of the slides fit tightly in the grooves, it was possible that the end of the slide was not always against the stop. The possibility also exists that a piece of chipped glass

would prevent the plate from resting against the stop. With the position uncertainties given above, the uncertainty assignment is 16 keV.

Clearly it would be preferable to calibrate the data slide itself with either a well-known reaction, like $Be^{9}(He^{3},p)B^{11}$, or with Po^{212} alphas (if a method of foil removal *in situ* could be devised). Because of the primary interest in relative level spacings, direct calibration was not pursued, although one unsuccessful attempt was made to use the $Be^{9}(He^{3},p)B^{11}$ reaction.

Energy losses of either the incident or outgoing reaction particles passing through the unknown backing foil thickness have not been included in the uncertainty calculations. Therefore the calculated uncertainties are applicable only to the "reflecting" geometry measurements at 80^{o} and 150^{o} (Figures 15d and e). Although the 30^{o}, 40^{o}, and 60^{o} spectra may not be used for determining the absolute excitation energies, they do contribute information about the relative level spacing.

Excitation energy calculations were based on the positions of levels 22 and 28, since these levels appear well resolved from background and other levels. The excitation energies were obtained by averaging the excitation energies calculated from the 80^{o} and 150^{o} data. They are listed in Table IV. The excitation energy values for the other levels

were obtained by:

1) calculating the excitation energies for each peak at each angle,

2) shifting (by subtraction of a number of keV) all the values obtained at a given angle (30^{o}, 40^{o}, or 60^{o}) by a constant amount so that the excitation energy values of levels 22 and 28 agree with the values listed in Table IV, and

3) averaging the values calculated for each level.

These excitation energies are also listed in Table IV. $Cl^{35}(He^{3},p)Ar^{37}$ excitation energies for levels 22 and 28 are 17 keV lower than the $K^{39}(d,\alpha)Ar^{37}$ energies.

D. DISCUSSION

Requirements for the use of a reaction comparison scheme to identify the lowest Ar^{37} $T=3/2$ level are more complex than is indicated in the Introduction. The problem may be discussed in three parts:

1) the probability that the $K^{39}(d,\alpha)Ar^{37}$ reaction at $E_d = 11$ MeV will populate only $T=\frac{1}{2}$ Ar^{37} levels;

2) the probability that the lowest $T=3/2$ level exists as a single unmixed level; and

3) the complications introduced by experimental problems.

(1) This part concerns the validity of isotopic spin selection rules for the $K^{39}(d,\alpha)Ar^{37}$ reaction at $E_d = 11$

MeV. The rules have been reviewed and discussed by Wilkinson (1956 a), Lane and Thomas (1958), and MacDonald (1960) and reference may be made to these works. For the specific reaction and energies under consideration, the relevant selection rule criterion depends on the characteristic time-dependent perturbation theory time $\hbar / H_c$ ($\hbar$, Planck's constant $/2\pi$; $\langle H_c \rangle$, an average coulomb matrix element between states that may mix appreciably) in which isotopic spin mixing occurs. If this time is long compared to the nuclear lifetime, $\hbar/\Gamma$ (Γ, the average total level width in the CN system), appreciable mixing will occur and the isotopic spin rules may be violated. If, however, the lifetime is short compared to the mixing time the degree of isotopic spin violation will be small (i.e., on the order of 1%) since the isotopic spin impurities of the K^{39} ground state, the deuteron, and the alpha are small. Wilkinson (1956a) treats the lifetime in terms of excitation energy of the compound nucleus. Noting that in general Γ increases with excitation energy, he estimates that between 15 and 25 MeV in light odd A nuclei Γ will have become sufficiently large for the isotopic spin rules to hold. DI mechanism reactions should follow the isotopic spin rules; in the O^{16} case the usual estimate of a lower limit for the CN lifetime as the time required for a nucleon to travel a distance equal to the nuclear diameter corresponds roughly to Wilkinson's

upper limit for selection rule validity. On the other hand, the isotopic spin rules may be severely violated if a CN model is applicable.

A detailed summary of the experimental work on isotopic spin rule validity is presented by Lane and Thomas (1958). This evidence has, of course, been expanded since 1958; in general the experimental work both before and after 1958 supports the above qualitative views. Three reviews of the rule validity in specific nuclei as a function of excitation energy are: O^{16} (Wilkinson 1956a) and F^{18} (Bromley) 1964, Carlson and Heikkinen 1965). At the higher excitation energies with which we are dealing almost complete violation of the selection rules is observed when the mechanism is predominantly CN. One of the most complete studies of this point is the work of Jänecke (1963) on the $Ca^{40}(d,\alpha)K^{38}$ reaction, previously cited in discussion of the $2I+1$ rule.

From the preceding discussion it is reasonable to expect the formation of the $T = 3/2$ level in $K^{39}(d,\alpha)Ar^{37}$ spectra only by means of a CN reaction mechanism. Since the $T = \frac{1}{2}$ levels may be formed through either a DI or CN mechanism, we require dominant DI $T = \frac{1}{2}$ cross sections in order to differentiate between the two isotopic spin states.

(2) Another consideration is possible final state iso-

topic spin mixing. In other reactions large suspected isotopic spin admixtures have led to apparent "violations" of the isotopic spin selection rules, e.g., $Ne^{20}(d,\alpha)F^{18}$ (Matous and Browne 1964) and $B^{10}(d,\alpha)Be^{8}$ (Erskine and Browne 1961). A meaningful calculation of this mixing requires a knowledge of the wave functions of nearby levels. It is difficult to construct a model yielding these wave functions; even the spins and parities have not been experimentally determined. There is, however, some experimental evidence that the mixing will be small. Goosman and Kavanagh (1965) have investigated K^{37} levels with the $Ar^{36}(p,p'\gamma_1)Ar^{36}$ and $Ar^{36}(p,\gamma)K^{37}$ reactions. The ratio of the cross sections from the population of individual K^{37} levels by the two reactions determines the quantity $\Gamma_\gamma/\Gamma_{p'}$. For the 5.04-MeV level this ratio is a factor of 10 greater than neighboring levels. On this basis we might expect some ($\sim 5\%$) $T = 3/2$ isotopic spin admixture in one of two closely spaced Ar^{37} levels, the other level containing the remainder of the $T = 3/2$ admixture.

(3) Experimental complications are a further consideration. Although increased resolution reduces the yield, owing to the necessity of thinner targets, smaller solid angle, and narrower collection slits, it will make possible the establishment of more accurate cross section values for weak and closely spaced levels (i.e., the 5.14-

MeV level and presently unresolved levels). With the present $K^{39}(d,\alpha)Ar^{37}$ data (Figure 12) it is possible to establish low relative cross section limits for the 5.14-MeV level. The peaks of the spectra of Figures 12 and 16 appear to be quite consistent with their single level assignments in that no significant peak shifts are apparent from one angle to another. These shifts might occur if the peaks were formed by unresolved levels with different angular distributions. Still, it is quite possible that not all levels have been identified; in many instances it would be impossible to identify two levels separated by 25 keV in the spectra of Figures 12 and 16. The possibility of unresolved levels is clearly a major disadvantage of the reaction comparison method--one that has been magnified by the high level density present at 5 MeV.

Some of the angular distributions in the 5-MeV region appear to reflect the DI mechanism. Others (Figure 13) do not display the forward peaking and asymmetry characteristic of the DI mechanism. The DWBA curves of Satchler (Jänecke 1963) show a decrease in these characteristics as higher transferred ℓ-values are considered. The angular distributions in the 5-MeV region that do not display the DI characteristics may be levels of high spin, with several competing high ℓ-values allowed. It is reasonable to assume that a DI reaction mechanism accounts for much of the observed alpha yield to states near 5-MeV excitation,

as it does at lower excitation energy.

E. CONCLUSION

There are no states seen in the $Cl^{35}(He^3,p)Ar^{37}$ reaction that are not also populated in the $K^{39}(d,\alpha)Ar^{37}$ reaction. Therefore, the most unambiguous evidence of the presence of a $T = 3/2$ level is lacking.

It is interesting to look for states weakly populated in the $K^{39}(d,\alpha)Ar^{37}$ reaction, since these transitions indicate that

1) the final state is a $T = 3/2$ level, populated through a CN mechanism (the CN mechanism is believed to be less likely than a DI mechanism) or

2) the final state is a $T = \frac{1}{2}$ level with a small probability of formation with this reaction.

The $K^{39}(d,\alpha)Ar^{37}$ cross section to the 5.13-MeV level is approximately 2.5 times less than that of any neighboring level (Figure 13). Furthermore, the angular distribution is consistent with the symmetry about 90° expected for the CN process, an argument supporting hypothesis (1) above. Of all the states observed in the Cl^{37} ground state region, the 5.13-MeV level most nearly displays the behavior expected of a $T = 3/2$ state.

F. OTHER EVIDENCE CONCERNING $T = 3/2$ LEVEL LOCATION

Since the work described in this thesis was initiated, three other studies have been made of Ar^{37} levels in the

5-MeV region.

(1) The $Cl^{37}(p,n)Ar^{37}$ reaction was investigated (Adelberger and Barnes 1965) in a search for Cl^{37} ground state analog level enhancement. This technique has been successfully used to find analog levels, e.g., Anderson et al. (1964) who used 18.5-MeV protons. Because of background problems, the $Cl^{37}(p,n)Ar^{37}$ reaction was investigated at a maximum E_p of 8.2 MeV. At this energy there was no apparent enhancement of any level in the 5-MeV region.

(2) Castro (1964) has studied the $Cl^{35}(He^3,p)Ar^{37}$ reaction. The spectrum shown in his thesis at $E_d = 6.5$ MeV, $\theta = 150^o$ indicates an experimental resolution of 40 keV. The targets are enriched AgCl evaporated on carbon backings and contaminant proton groups from carbon, nitrogen, and oxygen are present. Castro does not list the 5.13-MeV level (see Table IV) although a group is located at the 5.13-MeV position in the spectrum shown in his thesis.

(3) Wiza et al. (1965) have reported high resolution ($\sim$ 20 keV) observations of levels from the $Ar^{36}(d,p)Ar^{37}$ reaction. This reaction should populate only $T = \frac{1}{2}$ levels. Unfortunately, information on the 5-MeV region is unavailable except for the statement that transitions to their 5.07- and 5.16-MeV levels have "small cross sections" compared to their 5.11-MeV level (their levels correspond to this writer's 5.05-, 5.13, and 5.10-MeV levels; see Table IV). Observation of a strong transition to the 5.13 state in

the (d,p) reaction would cast grave doubt on the suggestion that this state has T = 3/2. Although the claimed experimental resolution is higher than that of the present experiment, no levels are seen that are not seen in this experiment.

The expected position of the lowest T = 3/2 level may be considered both in terms of three calculations and of the previously discussed K^{37} T = 3/2 experiments. Kavanagh and Goosman find at least the primary T = 3/2 component at 5.04-MeV K^{37} excitation energy. The T = 3/2 level should also appear at approximately this energy in the mirror Ar^{37} nucleus, a result which is consistent with the suggestion that the T = 3/2 level is at 5.13 MeV in Ar^{37}.

Calculations of the T = 3/2 level position are based on the relation

$$E_x(Ar^{37}) = (Cl^{37} + H^1 - Ar^{37} - n)c^2 + E_c(Ar^{37}) - E_c(Cl^{37})$$

where E_x is the excitation energy, the quantities multiplied by c^2 are the atomic mass excesses, and E_c is the coulomb energy.

(1) Assuming a uniform spherical charge distribution and the usual expression for the nuclear radius, $R = R_o A^{1/3}$,

$$E_c = \frac{3}{5} \frac{e^2}{R_o} \frac{Z(Z-1)}{A^{1/3}}$$

The quantity $\frac{3}{5} \frac{e^2}{R_o}$ is evaluated for the three mirror T = $\frac{1}{2}$ pairs closest to mass 37.

Mirror pair	$\frac{3e^2}{5R_o}$
K^{39} - Ca^{39}	650.2
Ar^{37} - K^{37}	641.8
Cl^{35} - Ar^{35}	649.0
average	647.0

From this table

$$E_c(Ar^{37}) - E_c(Cl^{37}) = 6602 \text{ keV}; \quad E_x(Ar^{37}) = 5.01 \text{ MeV}.$$

(2) This method (Wilkinson 1956b) considers only the mirror Cl^{35} - Ar^{35} pair; multiplication of the coulomb energy difference by $(1-2/A)^{1/3}$ allows for the increase in nuclear radius caused by the addition of two neutrons. This yields

$$E_c(Ar^{37}) - E_c(Cl^{37}) = 6621 \text{ keV}; \quad E_x(Ar^{37}) = 5.03 \text{ MeV}.$$

(3) De-Shalit and Talmi (1963) fit their three-parameter shell model expression for level positions to the experimental $d_{3/2}$ shell coulomb differences. From their expression

$$E_c(Ar^{37}) - E_c(Cl^{37}) = 6750 \text{ keV}; \quad E_x(Ar^{37}) = 5.15 \text{ MeV}.$$

The three predicted Ar^{37} excitation energies of 5.01, 5.03, and 5.15 MeV are consistent with the suggestion that the T = 3/2 level is at 5.13 MeV.

G. Ar^{37} LEVELS - NUCLEAR TEMPERATURE

A by-product of the search for the T = 3/2 level has been the observation of seventeen Ar^{37} excited states

(Table IV) between 4.5 and 5.9 MeV. An Ericson (1958, 1959, 1960) plot of the levels seen in this experiment is shown in Figure 17. From the plot of the number of levels below a given excitation energy, $N(E_x)$, vs. the excitation energy E_x, we extract the quantity Ericson has defined as the nuclear temperature, τ. This temperature,

$$\frac{1}{\tau} = \frac{d}{dE_x} \log N(E_x)$$

is found to be 1.4 MeV. Comparison of this plot with the more linear plots of other nuclei by Ericson (1959) and MacDonald and Douglas (1961) suggests that not all levels are resolved at the highest excitation energy. The temperature results cited by the above authors for nuclei with the same T_z (a dependence on T_z was suggested by the work of Bardeen and Feenberg (1938)) are: 2.2 MeV for Mg^{25}, 1.8 MeV for Si^{29}, and 1.6 MeV for S^{33}, consistent with the observed 1.4 MeV for Ar^{37}.

H. SUMMARY

The primary aim of the work described in this part was to determine the excitation energy of the lowest $T = 3/2$ level in Ar^{37} by comparing levels populated by the $K^{39}(d,\alpha)Ar^{37}$ and $Cl^{35}(He^3,p)Ar^{37}$ reactions. The lowest $T = 3/2$ Ar^{37} level is expected near 5.1-MeV excitation energy. In the region between 4.6 and 5.5 MeV, the same eleven levels were observed in both reactions. This leads

to three possibilities:

1) Isospin is not "conserved" in the (d,α) reaction, probably because of a CN mechanism

2) The T = 3/2 state has not been excited or observed in the (He^3,p) reaction

3) States in Ar^{37} have such large isospin mixtures that conservation rules offer no evidence of the character of the states.

The weak 5.13-MeV level has an angular distribution consistent with the CN mechanism and, of the eleven levels, this level displays most closely the characteristics expected for a T = 3/2 level.

Seventeen levels were found between 4.5- and 5.9-MeV excitation energy; they are tabulated in Table IV. An Ericson plot of the level density shows that unresolved levels may be present at the high excitation energies and that the level density (τ = 1.4 MeV) is in accord with similar plots for other light nuclei.

APPENDIX I: MAGNETOMETER

At the time of construction of the 61-cm spectrometer, three principal methods of monitoring the magnetic field were considered. The first method had been previously used in various forms in this laboratory (Lauritsen and Lauritsen 1948, Li 1951, and Bardin 1961). A coil pivoted in the magnetic field to be measured is displaced by a constant torque applied to the coil. This torque (and the angular displacement) is then canceled by an opposing torque created by passing a known current through the coil. The second method, utilizing the Hall effect, involves measuring the voltage developed across a semiconductor, placed in the field to be measured, through which a standard current flows. The third method employs a proton resonance magnetometer adapted to operate in the inhomogeneous $r^{-\frac{1}{2}}$ field of the spectrometer.

Of the three methods, only the nuclear magnetic resonance (NMR) device has the advantage of being "fail-safe," and for this reason was selected as the magnetometer for the 61-cm spectrometer. Although malfunctioning NMR apparatus may cause loss of the resonance signals, the field is uniquely determined if the signals are present, whereas defective equipment does not necessarily preclude a field indication in the apparatus of the first two methods. This criticism is particularly valid for the Hall magnetometer,

since even small variations in the current or temperature of the device will produce a spurious Hall voltage. Another advantage of the NMR method is the inherent accuracy of frequency measurements. A commercial frequency counter may be employed; in practice the spectrometer NMR uses the same frequency counter as does the NMR device used to measure the homogeneous field of the beam analyzing magnet.

Andrew's (1958) book is an excellent "review article" of the various designs and applications of NMR devices, and contains a detailed bibliography. The NMR device used as the magnetometer consists of a proton sample located inside a coil which forms the inductive component of an oscillator tank circuit. The axis of the coil is placed perpendicular to the magnetic field of interest. A variable capacitor controls the oscillator frequency. When the oscillator frequency (rf) equals the Larmor precession frequency of the protons, the proton system will absorb energy, since some of the protons undergo transitions to the excited state of

$$E = \frac{\mu H}{I}$$

where μ is the maximum measurable component of the magnetic moment, I is the proton spin, and H the magnetic field. Andrew points out that only a small population excess accounts for the absorption of energy at resonance, since the probability of stimulated de-excitation transitions and the relative population excess in the lower state may be given

by the Boltzman factor

$$\exp\left[\frac{2\mu H}{kT}\right] \approx 1 + \frac{2\mu H}{kT} = 1 + 4 \times 10^{-6}$$

for protons at room temperature in a field of 5000 gauss.

If the frequency and field satisfy the resonance condition for a long period of time, saturation will occur and it will no longer be possible to place a net amount of energy in the proton system. For this reason, a pair of series-connected coils approximating the Helmholtz geometry are placed around the sample so that an applied alternating current will produce an alternating field parallel to the field to be measured. The resonance condition is traversed twice on each complete cycle of the modulating field. Each time resonance occurs, the parallel resistance of the tank circuit decreases and the voltage across the tank circuit decreases (the oscillator is designed to serve as a constant current source). The resonance condition may be observed by sweeping an oscilloscope horizontally with the modulation frequency and by displaying vertically the audio frequency envelope of the rf voltage.

Figure 18 is a block diagram of the general method described above as it applies to the 61-cm spectrometer. The oscillator and detector circuits are shown in more detail in Figure 19. These circuits are slight modifications of the circuit described by Singer and Johnson (1959). This marginal oscillator is a simple one-transistor device

with only two free parameters available for operator adjustment; the variable capacitance of the tank circuit adjusts the frequency and the variable 2.5-kΩ regeneration potentiometer limits the amplitude of the voltage developed across the load. The single-detector stage rectifies the oscillator output and supplies the envelope of the rf to the audio amplifier. The oscillator frequency is stable to within a few parts in 10^5 over long periods of time.

Since the spectrometer $r^{-\frac{1}{2}}$ field creates a field inhomogeneity of approximately 1% per cm of radius, the method of Vincent, King, and Rowles (1959) was used to cancel the field gradient. As shown schematically in Figure 20, this method involves four series-connected coils placed around the sample coil; the magnitude of the current determines the amount of "compensating" field seen at the sample. The usual field plotting methods (in this case with uniform resistance paper and silver paint) were employed to investigate the field generated at the sample by four ideal compensating coils, i.e., four pairs of infinitely long thin wires. Only this ideal case may be treated using the incomplete analogy of the magnetostatic potential (Weber 1950) to the electrostatic potential. The results were compatible with the geometry used by Vincent et al and the dimensions of the final coils for the magnetometer were scaled from their coils. The presence of "ringing" after

the modulating field passes through the resonance condition demonstrates that this method successfully removes the field gradient. The "ringing" is seen as oscillations of the oscilloscope trace between ground and a smooth envelope of the resonance trace, and may be made plausible with the aid of the following classical picture (Bloembergen et al. 1948). At resonance, the spins precess in phase with the applied rf field. As the modulation field moves adiabatically past resonance, the spins continue to precess coherently--the rate changing as the field changes value--for a relaxation time characteristic of the sample. The magnetic moments beat with the H of the applied fixed frequency field, producing the "ringing" effect. Any variation of the field over the sample causes interference between the signals derived from the different parts of the sample, consequently reducing the magnitude of the ringing effect.

Andrew (1958) discusses in detail the factors affecting the signal-to-noise voltage ratio. The two factors of greatest importance to the design of the magnetometer are

1) the linear dependence on the number of protons within the effective volume of the coil, and

2) the dependence on $Q^{\frac{1}{2}}$, where $Q = \omega L/R$ with ω equalling the angular frequency of the applied field, L the sample coil inductance, and R the coil resistance.

The limitation on the volume of the sample is the gap width (the distance between the magnet pole pieces) and the distance into the $r^{-\frac{1}{2}}$ field that the brass probe container can project without intercepting useful beam. These dimensions determine the size of the compensating coils, which in turn determine the maximum sample diameter. Figure 21 shows the positions selected for the two probes. Since the magnetometer was constructed before the use of emulsions or a focal plane array of detectors was considered, it was placed at the detector end of the magnet so that the probes could project farther into the $r^{-\frac{1}{2}}$ field without restricting the maximum acceptance solid angle of the spectrometer (the object distance being greater than the image distance). The cylindrical brass containers have an inside diameter of 5.5 cm, and project beyond the inside surface of the vacuum chamber 3.4 cm (D in Figure 21) and 4.1 cm (E in Figure 21). The proton samples are 0.66 cm in diameter and 1.6 cm long, and are made by sealing mineral oil in thin-walled glass tubes.

The value of $Q^{\frac{1}{2}}$ is not as flexible a quantity as the sample volume in determining the signal-to-noise ratio. It is important to reduce the stray capacitance to a minimum, since

$$f^2 \propto L^{-1}C^{-1}$$

which yields

$$df \propto L^{-1/2}C^{-3/2}dC$$

and a given tuning capacitor (ΔC) must yield as large a range of frequencies (Δf) as possible. Two separate probes and oscillators (Figures 18 and 21) are required to span the range of spectrometer field. It is also desirable to reduce the stray capacitance of the high-frequency probe so that more turns of wire may be added to increase the volume of the sample coil. The capacitance was reduced by mounting the probe directly on the oscillator chassis, and an oscillator frequency range of 19.5 to at least 50 Mc/sec was obtained with a coil containing three and one-half turns of number 14 wire wound around a 0.66-cm diameter drill. As shown in Figure 21, the low frequency probe is mounted farther from the detector than the high frequency probe. Although less cable capacitance would be present if the probe positions were interchanged, the compensating coils of the low frequency probe require fewer turns of wire and can be placed in the brass container which projects a shorter distance into the vacuum chamber. This distance is, of course, subject to the condition that the sample must be in a portion of the field with a uniform gradient. The low frequency probe is mounted at the end of a hand-made coaxial brass tube which has approximately one-half the capacitance of commercial RG-62 coaxial cable. The coil is formed from a single winding of number 17 wire around a 0.66-cm diameter drill and has ten turns over its 1-cm length. This

gives a frequency range of 5.8 to 12.0 Mc/sec. In order to cover completely the frequency range of 6 to 45 Mc/sec a middle (mid) frequency range has been obtained by placing an inductive coil in parallel with the sample coil of the low-frequency oscillator. This shunt is placed in the circuit by a relay in order to meet the requirement of remote operation of the magnetometer.

The two free parameters of the oscillator circuits (capacitor and regeneration resistance, Figure 19) are operated remotely by two selsyns which in turn operate two worm gears, each of which operates two gears leading to the potentiometers or capacitors of both the high and low frequency oscillators. Tuning the "frequency" selsyn in the control room thus tunes the variable capacitors of both the high and low frequency oscillators simultaneously. A schematic illustration of the gear box is shown in Figure 21. A switch in the control room actuates relays which select the frequency range--low, middle, or high--of the experimenter's choice. These relays serve to

1) turn on the power for the appropriate oscillator chassis,

2) connect this chassis with the common audio amplifier,

3) connect the chassis with the frequency meter,

4) turn on the proper compensating coils,

5) turn on the audio amplifier, and

6) turn on cooling for the compensating coils.

The items listed above have been previously described, except for the compensating coil cooling. Because of the heat generated by the compensating coils enclosed in the brass canisters, low-pressure air is fed into and out of the canisters, thus maintaining a flow of air around the coils. The air pressure also expands brass bellows which actuates a microswitch. If the pressurized air supply should fail, the magnetometer is turned off and a warning light appears on the operating console.

At present the limitation of the frequency range is the heat developed by the compensating coils. The somewhat arbitrary maximum of 45 Mc/sec, determined by this heat generation, is close to the maximum practical frequency of 48 Mc/sec. This latter frequency maximum is dictated by the incomplete inhomogeneous field cancellation of the compensating coils (assuming the compensating coils are always supplied with the optimum current). The remaining field inhomogeneity is a fixed percentage of the average magnetic field. Therefore an increase in the frequency increases the magnitude of the field inhomogeneity across the sample volume. Since different parts of the sample achieve resonance at different times of the modulating field cycle, the resonance traces broaden. In practice there is a noticeable trace broadening above 45 Mc/sec; above 48

Mc/sec the resonance condition becomes difficult to locate.

The major difficulty with the construction of the magnetometer was the signal-to-noise ratio. Copper shielding did not appear to affect the noise level. The signal-to-noise ratio was increased to a usable level by reducing the detector inductances (D in Figure 19) to a minimum, and orienting the two identical inductances so that any field picked up in one would be canceled in the other. Difficulties presented by microphonics were largely overcome by isolating the selsyns from the gear box with rubber connectors and by supporting most of the electronics on a brass plate securely bolted to the outer return of the magnet. At a preliminary stage of the magnetometer's development, the signal-to-noise ratio of the transistorized circuitry was compared with that of another device employing the same circuitry as the commercial NMR used with the tandem analyzing magnet. There was no significant difference in the operation of the two devices.

Perhaps the most important of the magnetometer's qualities is its accuracy. The lack of a noticeable uniform drift of either frequency or the resonance traces after a fifteen-minute waiting period indicates that thermal effects are minimal. Po^{212} alpha source measurements are reproducible within one part in 25000 after hysteresis effects have been minimized and thermal equilibrium has

been reached (Groce 1963). This reproducibility implies that any difference between the field at the probes and the central field owing to saturation or different thermal coefficients of the materials which determine the probe position may be included in the calibration of the spectrometer (Figure 6).

If the compensating coils are not aligned properly with respect to the sample, an additive field, dependent on the strength of the compensating current, may be present at the sample. This effect will also be included as part of the calibration of the magnetic field-to-frequency relationship (Figure 6) and will not affect the accuracy of operation unless the signals remain visible over a range of compensating current values wide enough to change the additive field appreciably. This has been investigated and found to produce an error of less than one part in 10^4 in magnetic field. Since the experimenter should always "peak" the magnitude of the traces, this figure is not a limitation of the accuracy of the magnetometer. With the smallest modulating coil current setting, 2.5 mm on the oscilloscope corresponds to approximately $1/10^4$ in magnetic field at a field of 2 Kg. Although in practice the traces can usually be located to within ± 1 mm, the magnet current regulation dictates a ± 2.5 mm tolerance on trace position.

Other than the periodic changing of the oscillator and audio amplifier batteries, the only maintenance necessary in three years of operation has been the replacement of one relay, and a tube in the oscilloscope. However, the apparatus underwent several revisions as it was being built and could still be improved. The rubber couplings from the selsyns to the gear box produce an annoying backlash. The rubber couplings might be eliminated by a pair of small motors. If the compensating and modulating coils were potted in epoxy, another two or three megacycles would be added to the usable frequency range without overheating the coils. Although the oscillator batteries last approximately a year, replacement of the amplifier batteries occurs every few months, with the increased use of the spectrometer, and it would be helpful to replace these with a DC power supply.

APPENDIX II: DETECTOR ARRAY

A. INTRODUCTION

A focal plane array of sixteen solid state detectors has been constructed to supplement the single detector device initially installed on the spectrometer. In many experiments the array permits accumulation of the data for a given spectrum with reduced total bombardment charge, using less machine time. The advantages of the latter are obvious--experiments may be conducted that would otherwise require prohibitive amounts of machine time. Reduced bombardment causes less target deterioration for a given spectrum. The array is the first multi-detector device used in conjunction with a spectrometer in this laboratory, and it is expected that experience with this array will provide the basis for improved future designs. The initial design criteria were developed by W. Whaling, D. Groce, and this writer; the final detailed designs of the array and associated electronics were completed by V.F. Ehrgott and L.J. Graham respectively; and the equipment was constructed in this laboratory. The detectors were obtained from Oak Ridge Technical Enterprises, Inc.

B. MECHANICAL DESIGN

Figure 22a is a reduction of the array assembly drawing. The focal plane angle, 41^{o} to the central ray, is derived from ray tracing measurements (Groce 1963). Two con-

trol rods outside the vacuum chamber operate two movable foil holders, which allow three absorber thicknesses (the foils inserted independently or simultaneously) to be placed in front of the detectors. The foil holders (Figure 22b) are mounted near the detectors to minimize small angle scattering displacements. The array design assumes an active area of 6.3 mm by 6.3 mm for each detector. Each surface barrier detector has a 300 micron depletion depth (nominally n-type silicon with 4000 ohm-cm resistivity and 85 volts bias). Since each detector is mounted at 41^{o} to the incident beam, its effective depth is 450 microns, the range of a 7.5 MeV proton.

Figure 22c is a cross section view showing some of the slit and detector dimensions. The slits initially installed in the array were milled from 0.51-mm thick tantalum sheet; the slit edges were normal to the detector surface. Data collected by passing a low-intensity proton beam through a 0.2-mm pinhole and exploring the detector surfaces and slit edges revealed energy losses in the neighborhood of the slit edges. This led to the replacement of these slits with the slits shown in Figure 22c. Sixteen individual slits were formed, each by plunging a 3.18-mm end mill ($\Delta p/p = 1/720$) into a 0.79-mm thick brass plate at an angle of 41^{o}. The center-to-center distance between slits is 5.80 mm; i.e., the center-to-center distance is 1.82 times the slit width and the detector active areas cover approxi-

mately one-half the focal plane over the length of the array. Since these slits do not present a tapered edge to the particles, the energy spectra of the detectors show little energy loss due to slit edge penetration or scattering.

For some experiments it is desirable to use narrower slits that will provide resolution greater than the 3.18-mm slits of Figure 22c. Slits of width 1.84-mm (measured perpendicular to the central ray, $\Delta p/p = 1/1250$) were made by forming a ladder with a 3.96-mm diameter brass rungs spaced 8.84 mm apart. The overall dimensions of the ladder are compatible with the dimensions of the foil holder closest to the detectors; in use the ladder replaces this foil holder. The 1.84-mm slits may therefore be remotely inserted or withdrawn without disturbing the calibration of the more generally used 3.18-mm slits. Since the ladder is thicker than the foil holder it replaces, the present foil holders cannot be used in conjunction with the new slits. Foils are often fastened directly to the ladder.

C. ARRAY ELECTRONICS

A block diagram of the array electronics is shown in Figure 23. Each of the sixteen detectors has its own preamplifier-amplifier-routing system. The output pulses from the sixteen amplifier systems are combined by a common summing amplifier whose output is examined and stored in a

Nuclear Data Pulse Height Analyzer (ND-160). The analyzer operates in a 16 x 64 mode; i.e., sixteen independent 64-channel analyzers. The routing pulses from each detector system select the proper group of sixty-four channels which then record the analysis of the pulse height obtained from the same detector system.

The charge-sensitive preamplifiers are adaptations of the RIDL 31-17 amplifier with conversion gains of 0.1 volt per MeV of particle energy. For detectors with 100 pf or less capacitance the electronic noise will contribute less than a 50-keV energy resolution to the detected particle group. At saturation the preamplifier output pulse is 1.2 volts. A toggle switch provides the preamplifier with two gain settings; the preamplifier saturates with either a 12-MeV or a 48-MeV energy loss in the detector.

The linear amplifier gain may be varied from 0 to 10 with a variable resistor accessible to the experimenter. This amplifier (and the summing amplifier) are adaptations of portions of the RIDL 31-12 circuitry. The linear amplifier saturates at 10 volts. In order to reduce spurious routing, a threshold bias stage rejects pulses of less than 1.5 volts amplitude from proceeding through the routing circuitry. The bias level is controlled by a potentiometer not readily accessible to the experimenter.

A standard 4 μsec 8 volt square wave is generated by the routing section, a trigger generator biased at 0.5

volts. With the usual threshold bias and linear amplifier settings, the array is insensitive to energy losses in the detector of less than 2 MeV. If special settings are used, the array will properly record energy losses greater than 1.5 MeV. The routing pulse is processed by a binary coder whose output routes the coincident linearly amplified pulse to the proper group of sixty-four channels. The detectors are numbered consecutively from 1 to 16, with increasing spectrometer radius. If no routing pulse is present (0000), the "linear" pulse is stored as a pulse from detector 1, a 0001 routing pulse as detector 2, 0010 as detector 3, etc.

Before the linear pulse reaches the analyzer it passes from the linear amplifier through a summing amplifier (gain = -1) which produces an output pulse

$$e_o = (-1)\sum_{i=1}^{16} e_i$$

The pulse size is adjusted to conform with the 0-2.7 volt acceptance range of the analyzer by an attenuator at the analyzer input.

Bias is applied to all detectors equally through a control which may be located either at the spectrometer or in the tandem control room. Individual detector bias adjustments and measurement points have been removed because of noise pickup problems.

D. DATA REDUCTION

The basic relation for describing a particle travel-

ling in a plane perpendicular to a magnetic field is the familiar

$$B R = P/Q$$

where B is the magnetic field, R the radius of curvature, P the momentum, and Q the charge.

Data collected by magnetic spectrometers can be regarded as belonging to one of two categories:

1) B is held constant - R is varied to examine the P spectra

2) R is held constant - B is varied to examine the P spectra

The first category usually includes data from broad-range spectrometers with their relatively long focal planes. The second category usually includes data from spectrometers (including double-focuing spectrometers) with one fixed-position detector placed in the focal plane. With the inhomogeneous field of the double-focusing spectrometer, only the central ray will have a constant R in the basic equation above. However, the data may still be related to the basic equation, as we show below.

Spectrometer data analysis in this laboratory is treated within the framework of category (2) (Snyder, Rubin, Fowler, and Lauritsen 1950) since the double-focusing spectrometers have each had single detectors. It is therefore logical and convenient to treat spectra from an array of

detectors by transforming the array spectra into a form equivalent to data taken by a single detector at the central ray position, thereby retaining the category (2) methods. The transformation of array spectra will be considered in two parts: if a certain counting rate, N, is obtained by detector x at a given field setting (corresponding to magnetometer frequency f) we must find

1) the frequency setting f' at which the central ray detector accepts the same particle momentum as accepted by detector x at frequency f

2) the counting rate N' that would be observed by the single central ray detector at frequency f'.

For brevity the transformation factors (1) will be called frequency factors and (2) will be called yield factors.

The detector array was designed so that detector 8 is very close to the central ray position. We consider detector 8 as the single central ray detector and relate the data from the other detectors to it. Detector 8 is calibrated with a Po^{212} alpha source at the target position; the magnetometer frequency written in the experimenter's notebook as he takes data is the frequency corresponding to detector 8. Of course, any other detector could be considered as the "reference" detector, and all calibrations would then be made with respect to that detector. When comparing any spectra taken with both the single detector and the array,

however, it is less confusing to have detector 8 as the reference detector.

Frequency factors were obtained by changing the spectrometer field so that the Po^{212} alpha group is moved across each of the sixteen detectors. The frequency recorded for detector x ($f_{x\alpha}$) is the frequency of detector 8 such that the known alpha momentum passes through the center of detector x. Since we wish to relate all data to detector 8, we note that the fixed alpha momentum is defined by $f_{8\alpha}$. Therefore, when the magnetometer reads $f_{x\alpha}$, $f_{8\alpha}$ is the frequency (momentum) accepted by detector x. Clearly, the frequency (momentum) observed by detector x ($f_{8\alpha}$) equals the measured frequency of detector 8 ($f_{x\alpha}$) times the ratio $f_{8\alpha} / f_{x\alpha}$. If for any fixed momentum

$$f_{8\alpha} / f_{x\alpha} = f_{8p} / f_{xp}$$

then, for any field,

$$f_x = f_8 \, (f_{8\alpha} / f_{x\alpha})$$

where f_x is the equivalent detector 8 frequency observed by detector x for a measured (notebook) frequency f_8 (which is also, of course, the frequency of detector 8).

This last hypothesis has been verified experimentally by scattering protons and deuterons from a thin gold foil. The spectrometer field has been varied and the frequency of the p and d groups recorded for each of the representative detectors 1, 4, 7, 10, 13 and 16 at four different beam mom-

enta. Table V is a tabulation of the frequencies of detector 7, and the ratios of the other detectors to detector 7. Within the experimental uncertainties, the ratios are independent of the field value. Detector 8 was not functioning at the time of this measurement, but the data implies that f_{8p}/f_{7p} will be independent of field. Since f_{xp}/f_{7p} (or f_{7p}/f_{xp}) is constant, f_{8p}/f_{xp} should also be a constant independent of field, and the Po^{212} alpha values of $f_{8\alpha}/f_{x\alpha}$ can be utilized to find f_x for any value of f_8; i.e.,

$$f_x = f_8\left(\frac{f_{8\alpha}}{f_{x\alpha}}\right)$$

The statement that f_{8p}/f_{xp} is independent of field is equivalent to the statement that the dispersion is constant. To show this we define the dispersion D as:

$$D \equiv \frac{\Delta r/r_8}{\Delta p/p_8} = \frac{\Delta r/r_8}{\Delta f/f_8}$$

where the subscripted quantities are evaluated at detector 8 and Δr is the radial displacement of a ray for a momentum or frequency displacement Δp or Δf, respectively. If f_{8p}/f_{xp} is independent of p then

$$\frac{f_{8p}}{f_{xp}} = \frac{f_x}{f_8}\bigg|_{\text{at } p} = \frac{f_8 + f_{8-x}}{f_8}\bigg|_p = 1 + \frac{f_{8-x}}{f_8}\bigg|_p = 1 + \frac{1}{D}\frac{r_{8-x}}{r_8}\bigg|_p$$

is independent of p and D is independent of p. The conclusion that the dispersion is independent of the field con-

curs with the ray tracing data obtained at several fields below 11 Kg in a two-cm range on either side of the central ray (Groce 1963).

Table VI presents the frequency factor data obtained by changing the field so that the Po^{212} alpha group moved across each of the sixteen detectors. The frequency of the alpha peak for each detector is used to find the frequency factor values. Both of these quantities are tabulated. Po^{212} source measurements with full aperture, $\phi = 11.2^{o}$ $\theta = 4.2^{o}$, and $\phi = \theta = 2^{o}$ yield the same frequency factors within experimental errors, indicating that the frequency factors are not a function of solid angle of the spectrometer. The frequency values are plotted in Figure 24.

Yield factors were obtained by finding the yield (y_{xf}) of detector x at a given frequency, $f_x = f$ and the yield (y_{8f}) of detector 8 with the field set at $f_8 = f_x = f$. Clearly, the yield (Y_{xf}) of detector x normalized to detector 8 (or, in other words, the yield that detector 8 would have at f) equals y_{xf} times the ratio $y_{8f}/\ y_{xf}$. If for any fixed momentum p

$$y_{8f}/\ y_{xf} = y_{8p}/\ y_{8f}$$

then, for any field,

$$Y_x = y_x(y_{8f}/\ y_{xf})$$

The data of Table V, described earlier in this section, show that $y_{8p}/\ y_{xp}$ is independent of p. If the mag-

net analyzes a spectrum at momentum p, with N counts per unit frequency and unit beam charge, then $y_{xp} = Nq \Delta f_{xp}$, where q is the charge and Δf_{xp} is the frequency range accepted by detector x at momentum p. Δf_{xp} may be expressed as $f_{xp1} - f_{xp2}$ where the subscripts refer to the frequencies at the slit edges (r_{x1} and r_{x2}) of detector x. Since Table V, within the experimental uncertainties, shows no frequency dependence of f_{xp}/f_{7p} for any of the array detectors investigated, we conclude that at positions r_{x1} and r_{x2} there will also be no frequency dependence of f_{xp1}/f_{7p} and f_{xp2}/f_{7p}. Therefore for any field the yield factors

$$\frac{y_{8p}}{y_{xp}} = \frac{Nq}{Nq}\,\frac{f_{8p1}-f_{8p2}}{f_{xp1}-f_{xp2}} = \frac{f_{8p1}-f_{8p2}}{f_{7p}} \cdot \frac{f_{7p}}{f_{xp1}-f_{xp2}}$$

$$= \left(\frac{f_{8p1}}{f_{7p}} - \frac{f_{8p2}}{f_{7p}}\right)\left(\frac{f_{xp1}}{f_{7p}} - \frac{f_{xp2}}{f_{7p}}\right)^{-1}$$

are independent of field.

The spectrum of particles elastically scattered from the interior of a clean tantalum sheet is used to evaluate the yield factors. It is convenient to obtain these factors in the frequency region two or three array frequency widths ($f_{16} - f_1$) below the calculated frequency position of elastic scattering from the surface nuclei; in this region the spectrum approximates a straight line.

1) y_{xf} values ($f = f_x$) are obtained in this frequency region for the sixteen detectors by a single array

exposure.

2) y_{8f} values are obtained by detector 8 exposures with f_8 equal to several frequencies throughout the frequency interval $f_{16} - f_1$ of the first exposure.

A smooth curve (in practice, a straight line) through the y_{8f} values provides a means of determining the y_{8f} value for each of the sixteen f_x of the first exposure. The yield factors are simply the ratios y_{8f}/ y_{xf}.

Figure 25 shows yield factor values as determined by L. Cocke. In all cases these factors differ from unity by less than 15%. The solid curve in this figure was derived from the data of Table VI, assuming that all of the sixteen slits were identical in width and spacing and that the detectors would register all particles that pass both the spectrometer solid angle slits and the collector slits. A smooth curve is fit to a plot of the frequency spacing between detectors. The ratios of these frequency spacings, as found from the curve, are the yield factors (discussed above). The deviation of the measured yield factors from the values indicated by the solid curve is not surprising. The effective solid angle changes along the focal plane. Owing to the difficulty of plunging a thin end mill through a brass plate inclined at 41^{o} to the end mill axis, the slits are not identical although a steel guiding jig was used. Very few of the detectors satisfy the design specifi-

cations placed on active area location. The wide deviation of detector 2 from the solid curve, for example, is the result of some particles passing through the slits and striking a dead area of the detector.

Unfortunately, the failure of the active detector areas to meet specifications also means that the beam (object) must be accurately located in the z (parallel to the field) direction in order that the image be contained by the maximum available active area of each detector. Object sizes should be limited in the z direction to 1.9 mm with respect to the beam axis or else the beam image will fall partially on the dead area of several detectors. Particular caution should be exercised with gas targets, since the object size may be quite large unless it is carefully collimated.

The yield factors depend on the ø angular entrance aperture of the spectrometer. Figure 26 shows data obtained with detector 16 by scattering protons from a gold foil. The lower ø slit has been placed at a reading of 0 and the upper ø slit placed at four different settings. The areas of the spectra are measures of the probability of the magnetometer canisters' intercepting particle rays passing into the spectrometer (Figure 26). Since the area indicates an obstruction for angle settings greater than 15 (3.28^{o}), most data are collected with slit settings of ø = 15;

measurements of yield factors have been made with $\phi = 15$ settings only.

The treatment of emulsion spectra is similar to the treatment of array spectra. The data of Table VII are used to transform the scale of plate position to the frequency scale of an equivalent single detector (detector 8). The data were obtained by exposing an emulsion to Po^{212} alphas at eleven different fields. Alpha group plate position is tabulated as a function of the field frequencies. The emulsion data are, of course, equivalent to the array data of Table VI and Figure 24. They are also plotted in Figure 24. It is most convenient to convert the emulsion spectra into single detector frequency spectra (category 2) rather than to work directly from plate position (category 1). This permits the use of the frequency Q-value program and emulsion spectra are then compatible with both array and single detector spectra.

E. ARRAY PERFORMANCE

The array has undergone continuous improvement since its construction, and the electronics system has been frequently revised. The first routing system utilized the two-dimensional mode of the Nuclear Data analyzer with each detector system producing a routing pulse of characteristic height. This system was abandoned when electronic drifts frequently created routing problems. The binary routing

system has also been revised and further modifications will probably be made to eliminate noise-generated routing pulses.

High counting rates create routing errors. The pulse height analyzer requires $10 + \frac{n}{2}$ microseconds (n ranges from 0 to 64 and equals the channel number) to analyze and store an incoming pulse. If a second pulse occurs within the processing time of an initial pulse, misrouting to another group of 64 channels may occur. Assuming that a one per cent misrouting is permissible, an order of magnitude calculation for the maximum counting rate N yields

$$N = \frac{.01}{2 \times 26 \times 10^{-6}} = 200$$

particles per second. Use of a blocking pulse from the analyzer to prevent further routing pulses from reaching the analyzer during processing of an initial pulse would, of course, eliminate this problem. Detection of weak particle groups in the presence of elastically scattered beam particles will require this modification. With use of a blocking pulse the only effect of a high counting rate will be the increase in the analyzer dead time.

For some applications it would be desirable to have an array of lower resistivity detectors. For example, the separation of low energy (2-3 MeV) doubly-charged alpha particles from protons is difficult with the present detectors since the bias must be reduced to the contact bias of

the detector, which varies from one detector to another. Low-resistivity detectors will have the required depletion depth at a bias of 5 or 10 volts. Insertion of foils to degrade preferentially the alpha energy is not possible because the proton and alpha peaks cannot be separated well enough. A detector system with a higher focal plane ratio of live detector area to dead area (between detectors) would be advantageous, particularly with experiments requiring higher resolution ($\leq$ 2-mm slits). Suitable array detectors are difficult to obtain. Since Ortec will not furnish replacement detectors of the original design, a source of new high-resistivity detectors will soon have to be found in order to maintain the present array efficiency.

An examination of the detector requirements of future spectrometer experiments is in order at this point. The array has resulted in an order of magnitude increase in the data output of the spectrometer for some experiments, and the idea of a focal plane array of detectors has been shown to be practical. It is time to consider refinements (different detector resistivity, geometry, positioning, and type (including position-sensitive detectors)) that will extend the increased array efficiency to a larger number of experiments. The rate of data collection with the array requires automatic methods of data handling.

APPENDIX III: Q-VALUE CALCULATION

For convenience the subscripts 1,2,3, and 4 refer to the usual reaction labeling convention of incident, target, observed, and residual nuclei, respectively. The frequencies of the beam analyzing and spectrometer magnets are f_1 and f_3, respectively.

The momenta, $P_{1,3}$, and total energies, $E_{1,3}$, of particles 1 and 3 are evaluated with the relations

$$P^2_{1,3} = E^2_{1,3} - M^2_{1,3} = k^2_{1,3} A f^2_{1,3} Z^2_{1,3} ,$$

where M is the approximate mass, Z is the charge, and A is a constant chosen equal to 2 M_p. Letting A = 2 M_p yields values of k_1 and k_3 equal to the k_a and k_s obtained with the approximate expression of Marion (1960) that is used in this laboratory; i.e.,

$$T \approx k f^2 Z^2 \left(\frac{M_p}{M}\right)\left(1 - \frac{T}{2M}\right),$$

where T is the kinetic energy.

The expression for

$$Q = M_1 + M_2 - M_3 - M_4$$

in terms of the known M_1, M_2, M_3, E_1, E_3, P_1, P_3 and θ_3 follows from the conservation of momentum

$$P^2_4 = P^2_1 + P^2_3 - 2P_1P_3\cos\theta_3$$

and the conservation of energy

$$E_1 + E_2 = E_3 + E_4 .$$

$$Q = M_1+M_2-M_3-[M^2_1+M^2_2+M^2_3-2E_3(E_1+M_2)+2E_1M_2+2P_1P_3\ \cos\theta_3]^{\frac{1}{2}} .$$

REFERENCES

Abuzeid, M.A., Baranik, A.T., El-Zaiki, M.I., Gontchar, V.J., Morsy, S.M., and Zaloubovsky, I.I. 1964, Nuc. Phys. 60, 264.

Adelberger, E. and Barnes, C.A. 1965, private communication.

Anderson, J.D., Wong, C., McClure, J.W., and Walker, B.D. 1964, Phys. Rev. 136, B118.

Andrew, E.R. 1958, Nuclear Magnetic Resonance, Cambridge University Press.

Bahcall, J.N. 1964a, Phys. Rev. Letters 12, 300.

Bahcall, J.N. 1964b, Phys. Rev. 135, B137.

Bahcall, J.N. 1964c, presented at the Second Texas Symposium on Relativistic Astrophysics (Amer. Phys. Soc., New York).

Bahcall, J.N., Fowler, W.A., Iben, I. Jr., and Sears, R.L. 1963, Astrophys. J. 137, 344.

Bardeen, J. and Feenberg, E. 1938, Phys. Rev. 54, 809.

Bardin, R.K. 1961, Ph.D. Thesis. California Institute of Technology.

Bethe, H.A. 1937, Rev. Mod. Phys. 9, 69.

Bloembergen, N., Purcell, E.M., and Pound, R.V. 1948, Phys. Rev. 73, 679.

Bromley, D.A. 1964, Nuclear Spectroscopy with Direct Reactions, (Argonne National Laboratory), ANL-6878, II, 353.

Brown, A.B., Snyder, C.W., Fowler, W.A., and Lauritsen, C.C. 1951, Phys. Rev. 82, 159.

Butler, S.T. and Hittmair, O.H. 1957, Nuclear Stripping Reactions (Wiley, New York).

Carlson, R.R. and Heikkinen, D.W. 1965, U. of Iowa--Physics 65-19 (to be published).

Castro, M.M. 1964, M.S. Thesis, Massachusetts Institute of Technology.

Cassagnou, Y., Iori, I. Levi, C., Mayer-Kuckuk, T., Mermaz, M., and Papineau, L. 1963, Phys. Lett. 6, 209.

Cosper, S.W. and Johnson, O.E. 1965, Phys. Rev. 138, B610.

Cusson, R.Y. 1964, private communication.

Davies, J.W. and Barnes, C.A. 1964, private communication.

Davis, R. Jr. 1964, Phys. Rev. Letters 12, 302.

Davison, P.W., Buchanan,J.O. and Pollard, E. 1949, Phys. Rev. 76, 890.

Demirlioglu, D. and Whaling, W. 1962 unpublished.

de Shalit, A. and Talmi, I. 1963, Nuclear Shell Theory (Academic Press, New York).

Endt, P.M. and Van der Leun, C. 1962, Nuc. Phys. 34, 1.

Ericson, T. 1958, Nuc. Phys. 8, 265.

Ericson, T. 1959, Nuc. Phys. 11, 481.

Ericson, T. 1960, Adv. Phys. 9, 425.

Erskine, J.R. and Browne, C.P. 1961, Phys. Rev. 123, 958 (1961).

Ferguson, A.T.G. and Paul, E.B. 1959, Nuc. Phys. 12, 426.

Fisher, T.R. and Whaling, W. 1964, Phys. Rev. 133, B1502.

Fowler, W.A. 1960, Mém. Soc. R. Sci. Liège, Ser. 5, 3, 207.

Gadioli, E., Marcazzan, G.M. and Pappalardo, G. 1964, Phys. Lett. 11, 130.

Goosman, D.R. and Kavanagh, R.W. 1965, private communication.

Groce, D.E. 1963, Ph.D. Thesis, California Institute of Technology.

Hansen, O., Koltay, E., Lund, N., and Madsen, B.S. 1964, Nucl. Phys. 51, 307.

Hardy, J.C. and Verrall, R.I. 1964, Phys. Rev. Lett. 13, 764

Harrison, W.D., and Whitehead, A.B. 1963, Phys. Rev. 132, 2607.

Hinds, S., Middleton, R., and Litherland, A.E. 1961, Proc. Rutherford Int. Jubilee Conf., Manchester (Heywood, London), 305.

Jahns, M.F., Nelson, J.B. and Bernstein, E.M. 1964, Nuc. Phys. 59, 314.

Jänecke, J. 1963, Nuc. Phys. 48, 129.

Kavanagh, R.W. and Goosman, D.R. 1964, Phys. Lett. 12, 229.

Kavanagh, R.W. and Goosman, D.R. 1965, private communication.

Lane, A.M. and Thomas, R.G. 1958, Rev. Mod. Phys. 30, 257.

Lauritsen, C.C. and Lauritsen, T.L. 1948, Rev. Sci. Inst. 19, 916.

Li, C.W. 1951, Ph.D. Thesis, California Institute of Technology.

MacDonald, W.M. 1960, Nuclear Spectroscopy Part B (Academic Press, New York), 932.

MacDonald, N. 1962, Nuc. Phys. 33, 110.

MacDonald, N. and Douglas, A.C., 1961, Nuc. Phys. 24, 614.

Marion, J.B. 1960, 1960 Nuclear Data Tables, Part 3 (U.S. Gov't. Printing Office, Washington, D.C.) 176.

Matous, G.M. and Browne, C.P. 1964, Phys. Rev. 136, B399.

Mattauch, J.H.E., Thiele, W., and Wapstra, A.H. 1965, Nuc. Phys. 67, 1.

Micheletti, S. and Mukherjee, P. 1965, Nuc. Phys. 63, 504.

Naqib, I.M., Gleyvod, R., and Heydenburg, N.P. 1965, Nuc. Phys. 66, 129.

Nelson, J.W., Carter, E.B., Mitchell, G.E., and Davis, R. H. 1963, Phys. Rev. 129, 1723.

Parker, P.D.M., Bahcall, J.N., and Fowler, W.A. 1964, Astrophys. J. 139, 602.

Pearson, J.D. 1963, Ph.D. Thesis, California Institute of Technology; and private communication.

Pellegrini, R. 1961, Nuc. Phys. 24, 372.

Rawlins, J.A., Riley, P.J., and Shin, Y.M. 1964, Bull. Amer. Phys. Soc. 9, 667.

Reeder, P.L., Poskanzer, A.M., and Esterlund, R.A. 1964, Phys. Rev. Lett. 13, 767.

Robertson, M.M., Mack, J., Cohen, V.W., and Davis, R. 1960, Bull. Am. Phys. Soc. 5, 411.

Robertson, M.M., Mack, J., and Cohen, V.W. 1965, Phys. Rev. (to be published).

Rosner, B., and Schneid, E.J. 1964, Bull. Amer. Phys. Soc. 9, 553.

Rosner, B., and Schneid, E.J. 1965, Phys. Rev. 139, B66.

Sears, R.L. 1960, Memoires Soc. R. Sci. Liege, Series 5, 3, 479.

Sears, R.L. 1964, Astrophys. J. 140, 477.

Sheline, R.K. and Nielsen, H.L. 1959, Nuc. Phys. 14, 140.

Singer, J.R. and Johnson, S.D. 1959, Rev. Sci. Inst. 30, 92.

Snyder, C.W., Rubin, S., Fowler, W.A., and Lauritsen, C.C. 1950, Rev. Sci. Instr. 21, 852.

Sun, C.R. and Wright, B.T. 1958, Phys. Rev. 109, 109.

Vincent, C.H., King, W.G., and Rowles, J.B. 1959, Nucl. Inst, and Methods 5, 254.

Wapstra, A.H. 1964, Nuc. Phys. 57, 48.

Weber, E. 1950, Electromagnetic Fields Vol. I, (Wiley, New York).

Weimer, P.K., Kurbatov, J.D. and Pool, M.L. 1944, Phys. Rev. 66, 209.

Wilkinson, D.H. 1956a, Phil. Mag. [8] 1, 379.

Wilkinson, D.H. 1956b, Phil. Mag. [8] 1, 1031.

Wiza, J.L., Hewka, P.V., and Holbrow, C.H. 1965, Bull. Amer. Phys. Soc. 10, 39; and private communication.

Woytowich, W. 1962, private communication.

Yamamoto, S.S., and Steigert, F.E. 1961, Phys. Rev. 121, 600

Yanabu, Yamashita, Nakamura, Takamatsu, Masaike, Kakigi, Nguyen, and Takimoto 1962, Jour. Phys. Soc. Japan 17, 914.

Yoshida, S. 1962, Nuc. Phys. 33, 685.

Zucker, A., and Watson, W.W. 1950, Phys. Rev. 80, 966.

TABLE I: SOLAR NEUTRINO FLUX

Number	Reaction	Q-value (MeV)	Flux
1	$H^1 + H^1 \rightarrow H^2 + e^+ + \nu$	0.420	10^{11}
2	$B^8 \rightarrow Be^{8*} + e^+ + \nu$	14.06	10^7
3	$N^{13} \rightarrow C^{13} + e^+ + \nu$	1.20	10^9
4	$O^{15} \rightarrow N^{15} + e^+ + \nu$	1.74	10^9
5	$Li^4 \rightarrow He^4 + e^+ + \nu$	18.8	-
6	$H^1 + H^1 + e^- \rightarrow H^2 + \nu$	1.44	10^8
7	$He^3 + e^- \rightarrow H^3 + \nu$	-0.018	10^6
8	$Be^7 + e^- \rightarrow Li^7 + \nu$	0.861 0.383	10^{10} 10^9
9	$O^{15} + e^- \rightarrow N^{15} + \nu$	2.76	10^5
10	$N^{13} + e^- \rightarrow C^{13} + \nu$	2.22	10^5
11	$B^8 + e^- \rightarrow Be^8 + \nu$	15.08	1

All flux values are order of magnitude values in units of number cm^{-2} and sec^{-1}. Reactions 1-4 produce continuous neutrino energy spectra with the approximate upper ν energy indicated. Reaction 5 produces an uncertain small flux value. Reactions 6-10 produce nearly monoenergetic neutrinos, the energy widths being determined by the thermal spread of the solar electrons. The neutrino energy spectra of reactions 2 and 11 reflect the 2 MeV breadth of the Be^8 state. (See page 1ff.)

TABLE II: Q-VALUE UNCERTAINTIES

	$Ca^{40}(p,\alpha)K^{37}$		$Ca^{40}(p,p)Ca^{40}$	
	Δf (kc/sec)	ΔQ (keV)	Δf (kc/sec)	ΔQ (keV)
Beam Analyzing Magnet ($f_a \sim 20$ Mc/sec)				
Entrance and exit slit width = 2.54 mm $\pm \frac{1}{4}$ FW gives $\Delta r/r = \pm 1/1360$	±8.6		±5.9	
Calibration constant $k_a = (19881 \pm 5) \times 10^{-6}$	±3.0		±2.0	
Current regulation (field drift) $\Delta I/I = \pm 1/7000$	±3.0		±3.0	
RMS subtotal	±9.6	±8.6	±7.0	±4.4
Spectrometer ($f_s \sim 20$ Mc/sec)				
Calibration constant $k_s = (11361.5 \pm 5) \times 10^{-6}$	±4.4		±4.4	
Current regulation (field drift) $\Delta I/I = \pm 1/10{,}000$	±2.0		±2.0	
Location of step midpoint	±4.0		±4.0	
RMS subtotal	±6.3	±3.5	±6.3	±3.0
Spectrometer angle ($\pm 0.05^{\circ}$)		±0.5		±0.2
RMS total		±9.4		±5.3

(See page 20).

TABLE III: EXCITATION ENERGY UNCERTAINTIES FOR Ar^{37} LEVELS

	$\left(\frac{\Delta f}{kc}\right)$ sec	ΔE_x (keV)
$K^{39}(d, \alpha)Ar^{37}$		
Analyzing magnet ($f_a \sim 32$ Mc/sec)		
Full slit width = 3.8 mm ($\Delta r/r = \pm 1/910$)	±18	
Calibration constant $k_a = (19881 \pm 5) \times 10^{-6}$	± 4	
Current regulation ($\Delta I/I = \pm 1/6000$)	± 5	
Subtotal	±19	±12
Spectrometer ($f_s \sim 34$ Mc/sec)		
Calibration constant ($\sim 11380 \pm 5) \times 10^{-6}$	± 7	
Current regulation ($\Delta I/I = \pm 1/10{,}000$)	± 4	
Typical peak frequency determination	±10	
Subtotal	±13	±11
Spectrometer angle ($\pm 0.05^{o}$)		± 1
Total		±16
$Cl^{35}(He^{3}, p)Ar^{37}$		
Analyzing magnet ($f_a \sim 20.8$ Mc/sec)		
Full slit width = 2.54 mm ($\Delta r/r = \pm 1/1360$)	± 8	
Calibration constant $k_a = (19881 \pm 5) \times 10^{-6}$	± 3	
Current regulation ($\Delta I/I = \pm 1/4000$)	± 5	
Subtotal	±10	±10
Spectrometer		
Calibration constant	± 8	
Current regulation	± 4	
Typical peak frequency determination ($\pm \frac{2}{3}$ mm)	± 5	
Error in holder position (± 0.6 mm)	± 4	
Plate position - data (± 1 mm)	± 6	
Plate position - calibration (± 1 mm)	± 6	
Subtotal	±14	±12
Spectrometer angle ($\pm 0.05^{o}$)		± 1
Total		±16

(See pages 26, 58).

TABLE IV: EXCITATION ENERGIES OF Ar^{37} LEVELS(∠5.9 MeV)

Ar^{37} level excitation energies are listed that have been reported since the compilation (column 8) of Endt and Van der Leun (1962). (See pages 4f., 28, 50, 66, 69f.)

TABLE IV: EXCITATION ENERGIES OF Ar^{37} LEVELS (≤5.9 MeV)

Level Number	McNally $K^{39}(d,\alpha)Ar^{37}$ ± 16 keV	McNally $Cl^{35}(He^3,p)Ar^{37}$ ± 16 keV	Castro (1964) $Cl^{35}(He^3,p)Ar^{37}$ ~± 5 keV	Wiza et al. (1965) $Ar^{36}(d,p)Ar^{37}$ ~± 10 keV	Rosner and Schneid (1965) $Ar^{36}(d,p)Ar^{37}$	Nelson et al. (1963) $S^{34}(\alpha,n)Ar^{37}$ ± 50 keV	Endt and Van der Leun (1962)
0	0.000		0.000	0.000	0.00	0.00	0.00
1	1.408		1.406	1.417	1.40	(0.70)	1.42
2	1.617		1.607	1.618	1.60	1.54	1.61
3	2.217		2.213				2.25
							2.41
4	2.498		2.484	2.501	2.50	2.56	2.54
5	2.797		2.792	2.807	2.80		
6	3.173		3.167		(3.18)		
7	3.273		3.266				
8	3.525		3.515	3.528	3.55	3.50	3.55
9	3.614		3.593				
10	3.711		3.693	3.717	3.74		
11	(3.751)						
12	(3.90)						
13	3.937		3.930	3.994			
14	4.020		(4.003)	4.047	4.04		
15	(4.215)		4.188	4.213	4.18		
16	4.282		4.277	4.284			
17	4.320						
18	4.402		4.385	4.421		4.40	4.40
19	4.451		(4.435)	4.466	4.49		
20	4.582		(4.562)				
21	4.634	4.623	4.613	4.657	4.68	4.63	4.63
22	4.750	4.733	4.729	4.764	4.81		
23	4.894	4.877	((4.83))	4.909	4.90		
24	4.991	4.976	4.978	5.010			
25	5.055	5.035	(5.036)	5.070			
26	5.110	5.087	(5.105)	5.110	5.18		5.07
27	(5.14)	5.122		5.158			
28	5.221	5.204	5.203	5.241	5.30		
29	5.354	5.338	5.341	5.376	5.43		
30	5.417	5.400	(5.401)	5.439			
31	5.460	5.426		5.467			
32		5.533					
33		5.568	5.574	5.565			
34		5.664	5.662	5.701			
35		5.762	5.761	5.802			
36		5.840	5.846	5.870			5.85

TABLE V: f_{xp}/f_{7p}

p [f_{7p} Mc/sec]	f_{1p}/f_{7p}	f_{4p}/f_{7p}	f_{10p}/f_{7p}	f_{13p}/f_{7p}	f_{16p}/f_{7p}
17.087	1.01626	1.00801	0.99256	0.98536	0.97881
27.781	1.01630	1.00795	0.99247	0.98544	0.97876
28.035	1.01655	1.00795	0.99250	0.98541	0.97866
35.132	1.01630	1.00796	0.99251	0.98542	0.97876
41.945	1.01623	1.00793	0.99260	0.98557	0.97894

f_{xp} equals the central frequency of the group observed in detector x. All measurements in a given row were made with particles of the same momentum. Ratios at f_{7p}=17.087 were obtained with protons scattered from gold. Ratios at f_{7p} = 27.781 were obtained with Po^{212} alphas. All other data were obtained with deuteron scattering from gold. Errors are approximately ± 1/40 FWHM (± 1 kc/sec for the 28.035 data); this yields an error of ± 5 x 10^{-5}. No significant change with frequency is observed in the vertical columns. (See pages 91ff.)

TABLE VI: FREQUENCY FACTORS

Detector Number	Frequency (Mc/sec) $\phi = \theta = 2^\circ$	Frequency Factors $\phi = \theta = 2^\circ$	Frequency (Mc/sec) $\phi = 6^\circ$ $\theta = 3.6^\circ$	Frequency Factors $\phi = 6^\circ$ $\theta = 3.6^\circ$
1	28.234	0.98148	28.226	0.98151
2	28.157	0.98416	28.150	0.98416
3	28.078	0.98693	28.069	0.98700
4	28.002	0.98961	27.994	0.98964
5	27.926	0.99230	27.917	0.99237
6	27.852	0.99494	27.845	0.99494
7	27.781	0.99748	27.774	0.99748
8	27.711	1.00000	27.704	1.00000
9	27.640	1.00257	27.635	1.00250
10	27.572	1.00504	27.566	1.00501
11	27.505	1.00749	27.499	1.00745
12	27.441	1.00984	27.435	1.00980
13	27.377	1.01220	27.370	1.01220
14	27.314	1.01453	27.307	1.01454
15	27.250	1.01692	27.246	1.01681
16	27.191	1.01912	27.186	1.01905

The frequency in the second column is the central frequency of the Po^{212} alpha line observed by the detector listed in the first column, with an acceptance angle $\phi = \theta = 2^\circ$. The third column lists $f_{8\alpha} / f_{x\alpha}$ for each detector. The last two columns list the same measurements for a different acceptance angle: $\phi = 6^\circ$, $\theta = 3.6^\circ$. Errors are approximately ± 1/40 FWHM (± 1 kc/sec); this yields an error of $\pm 5 \times 10^{-5}$. (See pages 92, 94; Figure 24.)

TABLE VII: EMULSION DISPERSION DATA

Frequency of Po^{212} alphas (Mc/sec)	Frequency Factors $f_{8\alpha} / f_{x\alpha}$	Plate Position (2/3 mm)
27.200	1.01838	19.5
27.300	1.01465	42.0
27.400	1.01095	62.7
27.500	1.00727	83.3
27.600	1.00362	100.3
27.700	1.00000	121.4
27.800	0.99640	140.8
27.900	0.99283	159.4
28.000	0.98929	176.9
28.100	0.98577	194.6
28.200	0.98227	211.5

The central positions of Po^{212} alpha groups on an emulsion are listed in the third column. The magnetometer frequencies of these groups are listed in the first column with the corresponding frequency factors ($f_{8\alpha}/f_{x\alpha}$) listed in the second column. Plate position is measured from the end of the emulsion plate at the largest spectrometer radius. (See pages 57, 96; Figure 24.)

FIGURE 1: INITIALLY ASSUMED LEVEL SCHEMES

The unbracketed quantities are tabulated in Endt and Van der Leun (1962). Quantities bracketed [ ] indicate additional assumptions made by Bahcall in order to carry out the flux-cross section calculations described in the Introduction. The number to the left of the Ar^{37}, K^{37}, and Ca^{37} ground states is the relative energy difference between the ground states of the nuclei on either side of the number. The branching ratios are the result of calculations by Bahcall. (See pages 4, 22.)

Figure 1

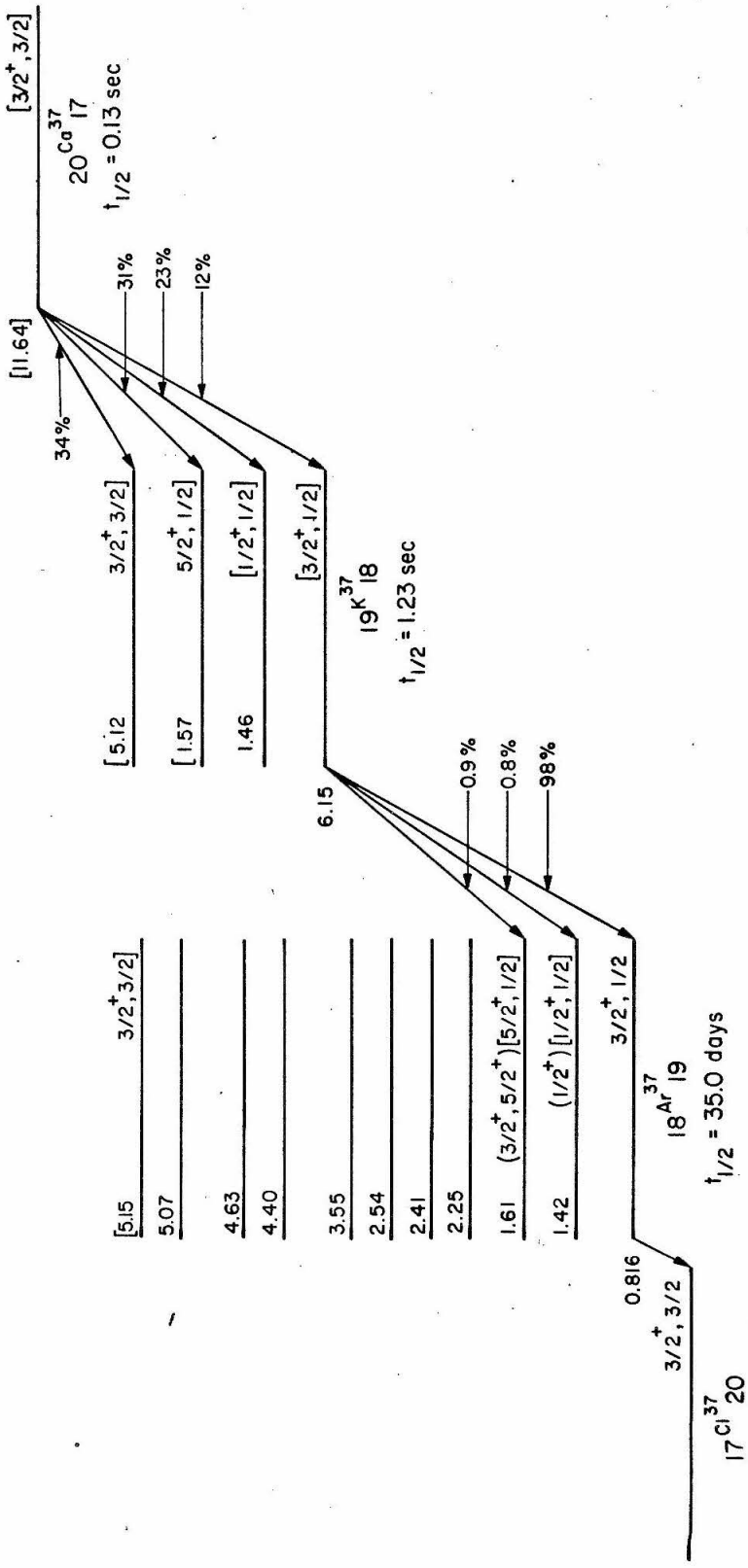
[3/2+,3/2]
20Ca37 17
t1/2 = 0.13 sec
[11.64]
34%
31%
23%
12%
[5.12 3/2+,3/2]
[1.57 5/2+,1/2]
1.46 [1/2+,1/2]
[3/2+,1/2]
19K37 18
t1/2 = 1.23 sec
6.15
0.9%
0.8%
98%
[5.15 3/2+,3/2]
5.07
4.63
4.40
3.55
2.54
2.41
2.25
1.61 (3/2+,5/2+)[5/2+,1/2]
1.42 (1/2+)[1/2+,1/2]
3/2+,1/2
18Ar37 19
t1/2 = 35.0 days
0.816
3/2+,3/2
17Cl37 20

FIGURE 2: LEVELS OF Ar^{37}

The Ar^{37} levels found in this experiment are shown in the level diagram. Dashed lines and numbers in parenthesis indicate tentative level assignments. To the right of the diagram are spins and parities found by Rosner and Schneid (1964, 1965), Goosman and Kavanagh (1965), and Robertson et al (1960, 1965). The level diagram may be compared with the levels tabulated by Endt and Van der Leun (1962), shown in Figure 1. (See page 28; Table IV.)

Figure 2

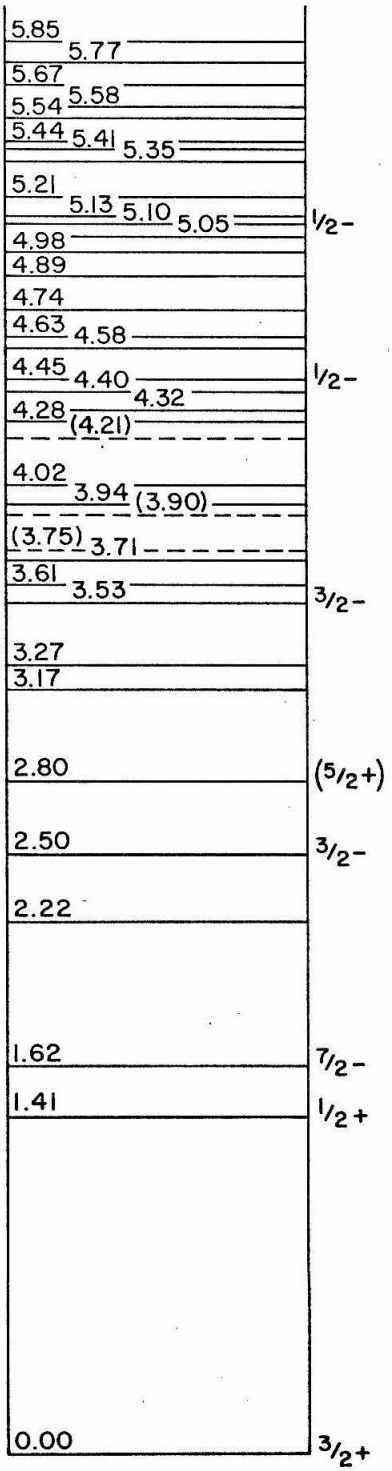

Ar^{37}

FIGURE 3: THICK TARGET SPECTRA FOR THE $Ca^{40}(p,\alpha)K^{37}$ GROUND STATE Q-VALUE

The order of data collection is the order illustrated [a), b) and c)] with a change to a thinner target between a) and b). Experimental conditions are shown on each spectrum. Crosses mark the half-height frequency (f_s). A 4-kc/sec uncertainty is assigned to f_s. Three contributions to the resolution are shown: δr_c, the collector slit resolution; $\delta \theta$, the kinematic resolution due to solid angle; and δr_a, the beam energy resolution due to the total analyzing slit width. (See pages 10f., 14.)

Figure 3
(a)

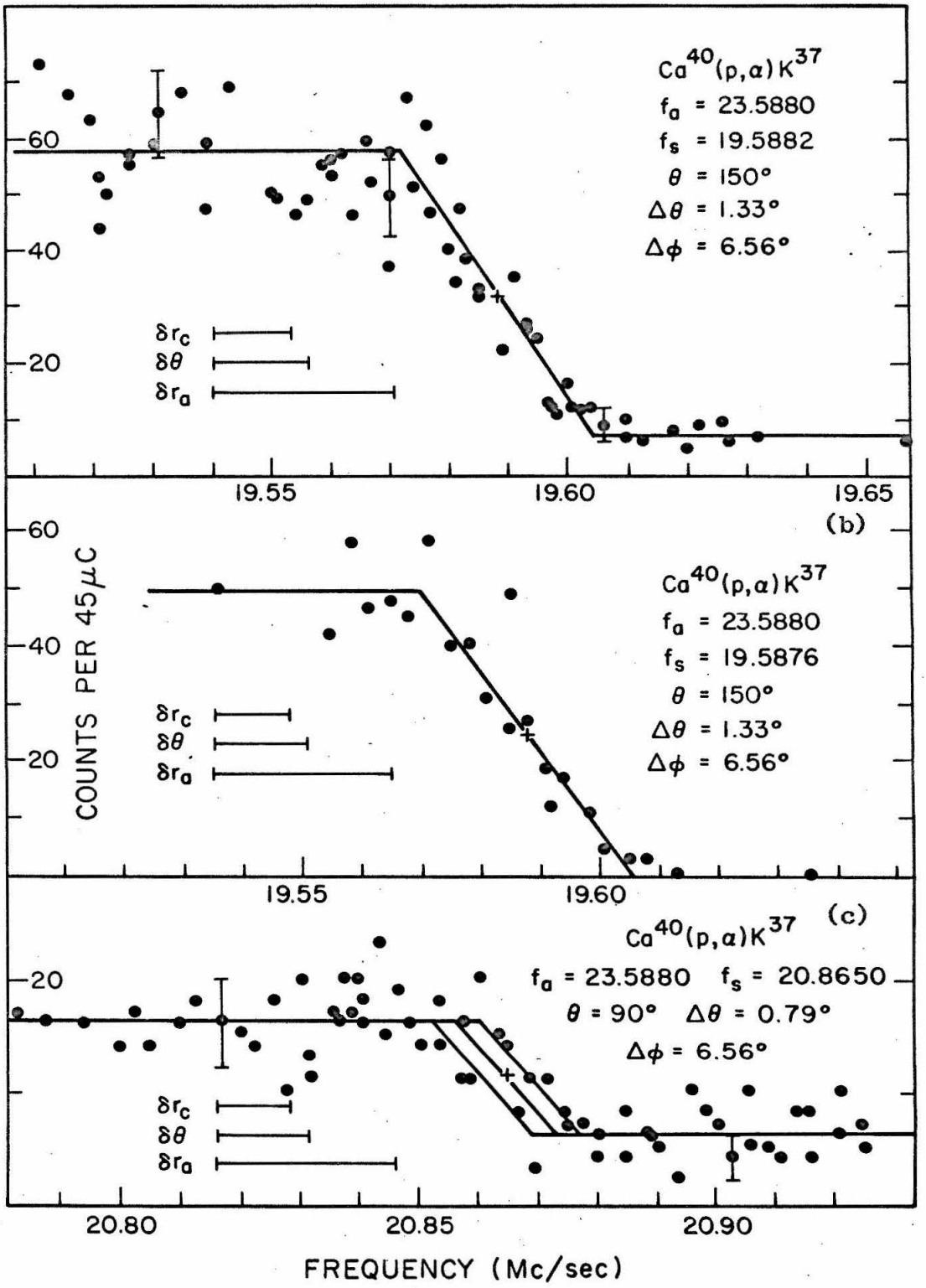
$Ca^{40}(p,\alpha)K^{37}$
f_a = 23.5880
f_s = 19.5882
θ = 150°
$\Delta\theta$ = 1.33°
$\Delta\phi$ = 6.56°
δr_c
$\delta\theta$
δr_a
60
40
20
19.55
19.60
19.65
(b)
COUNTS PER 45 μC
$Ca^{40}(p,\alpha)K^{37}$
f_a = 23.5880
f_s = 19.5876
θ = 150°
$\Delta\theta$ = 1.33°
$\Delta\phi$ = 6.56°
(c)
$Ca^{40}(p,\alpha)K^{37}$
f_a = 23.5880 f_s = 20.8650
θ = 90° $\Delta\theta$ = 0.79°
$\Delta\phi$ = 6.56°
20.80
20.85
20.90
FREQUENCY (Mc/sec)

FIGURE 4: THICK TARGET SPECTRA FOR $Ca^{40}(p,p)Ca^{40}$ ELASTIC SCATTERING

The order of data collection is the order illustrated [a), b), and c)] with a change to a target of approximately the same thickness between a) and b). Figure notations are the same as Figure 3. The approximate expected step position of $Ca^{42}(p,p)Ca^{42}$ and $Ca^{44}(p,p)Ca^{44}$ contributions are indicated. (See pages 11, 14.)

Figure 4-

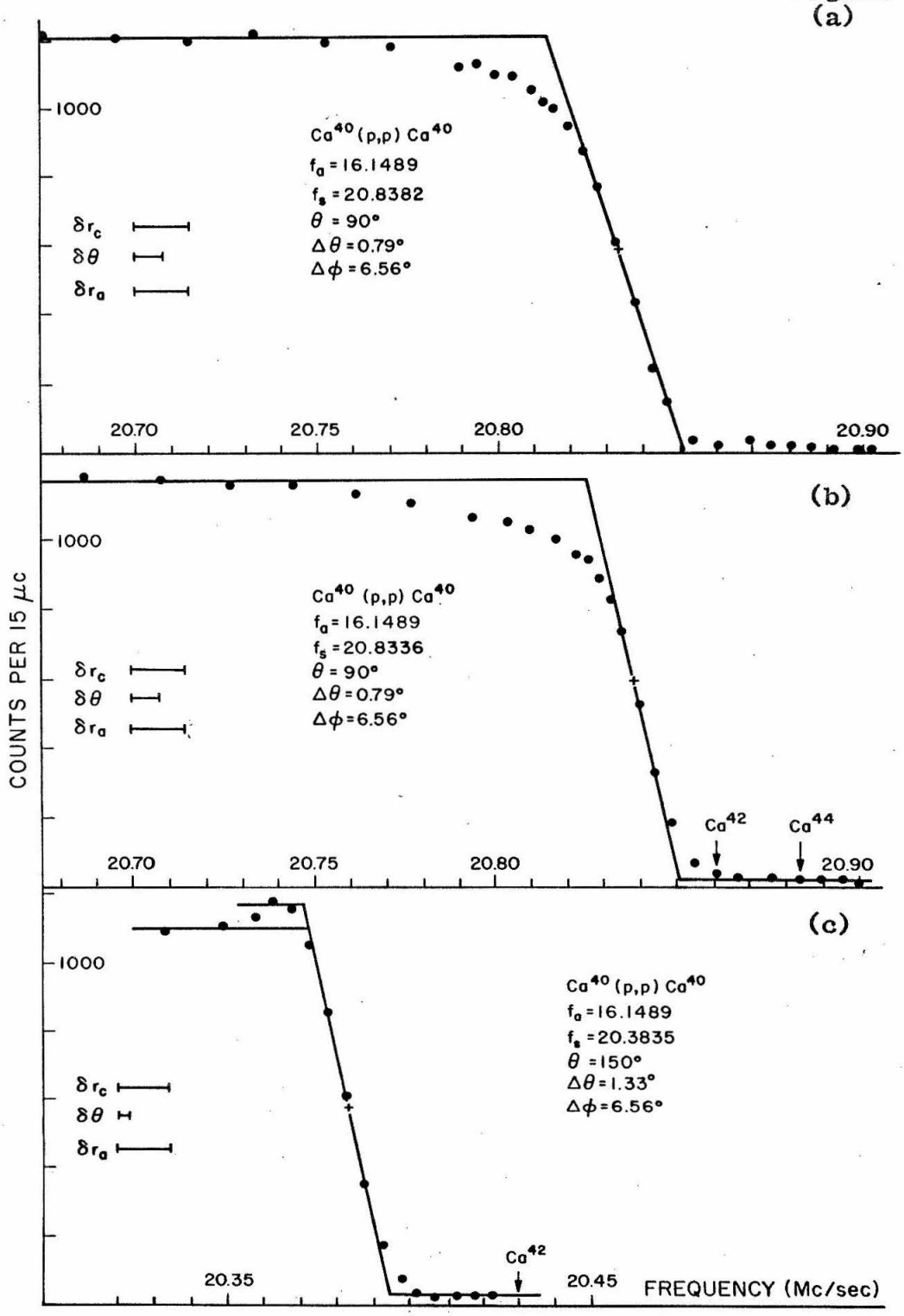
(a)
1000
Ca^{40} (p,p) Ca^{40}
f_a = 16.1489
f_s = 20.8382
θ = 90°
$\Delta\theta$ = 0.79°
$\Delta\phi$ = 6.56°
δr_c
$\delta\theta$
δr_a
20.70
20.75
20.80
20.90
(b)
1000
Ca^{40} (p,p) Ca^{40}
f_a = 16.1489
f_s = 20.8336
θ = 90°
$\Delta\theta$ = 0.79°
$\Delta\phi$ = 6.56°
δr_c
$\delta\theta$
δr_a
Ca^{42}
Ca^{44}
20.70
20.75
20.80
20.90
COUNTS PER 15 μc
(c)
1000
Ca^{40} (p,p) Ca^{40}
f_a = 16.1489
f_s = 20.3835
θ = 150°
$\Delta\theta$ = 1.33°
$\Delta\phi$ = 6.56°
δr_c
$\delta\theta$
δr_a
Ca^{42}
20.35
20.45
FREQUENCY (Mc/sec)

FIGURE 5: DATA FOR SPECTROMETER CALIBRATION CURVES

The ratio of spectrometer frequency (f_s) to analyzing magnet frequency (f_a) is plotted for various spectrometer frequencies (f_s). He^{4+}, He^{4++}, and p beams were used. The experimental arrangement is described in the text. The Po^{212} alpha line shown is necessary to obtain absolute calibration constants. (See pages 16f.)

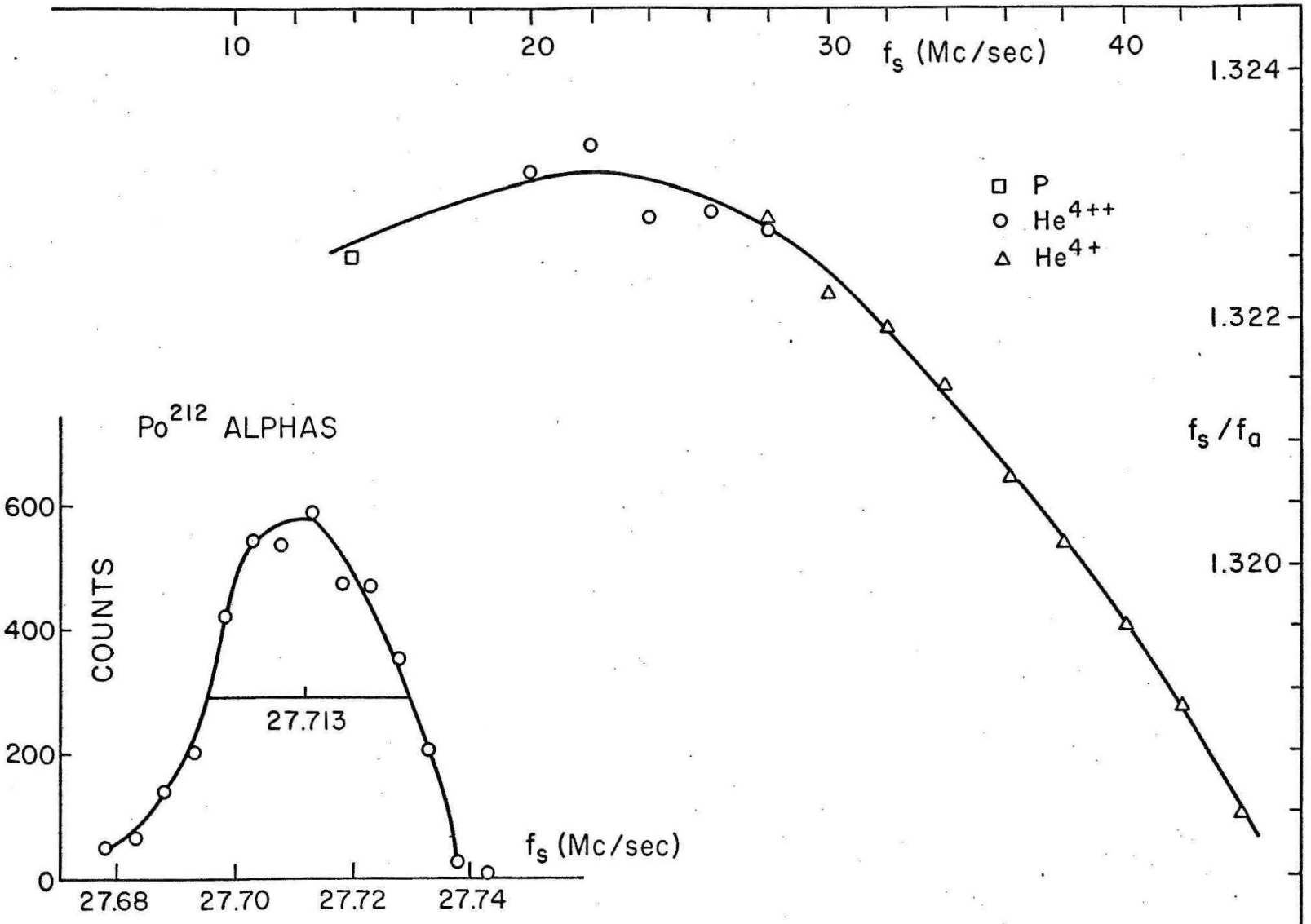
10
20
30
f_s (Mc/sec)
40
1.324
1.322
1.320
f_s/f_a
P
He^{4++}
He^{4+}
Po^{212} ALPHAS
COUNTS
600
400
200
0
27.713
f_s (Mc/sec)
27.68
27.70
27.72
27.74

Figure 5

FIGURE 6: SPECTROMETER CALIBRATION CURVES

These curves are obtained from the data of Figure 5 for two different collector slit positions such that the Po^{212} alpha line appears at spectrometer frequencies of 27.707 Mc/sec and 27.712 Mc/sec respectively. (See pages 18, 26, 81.)

Figure 6

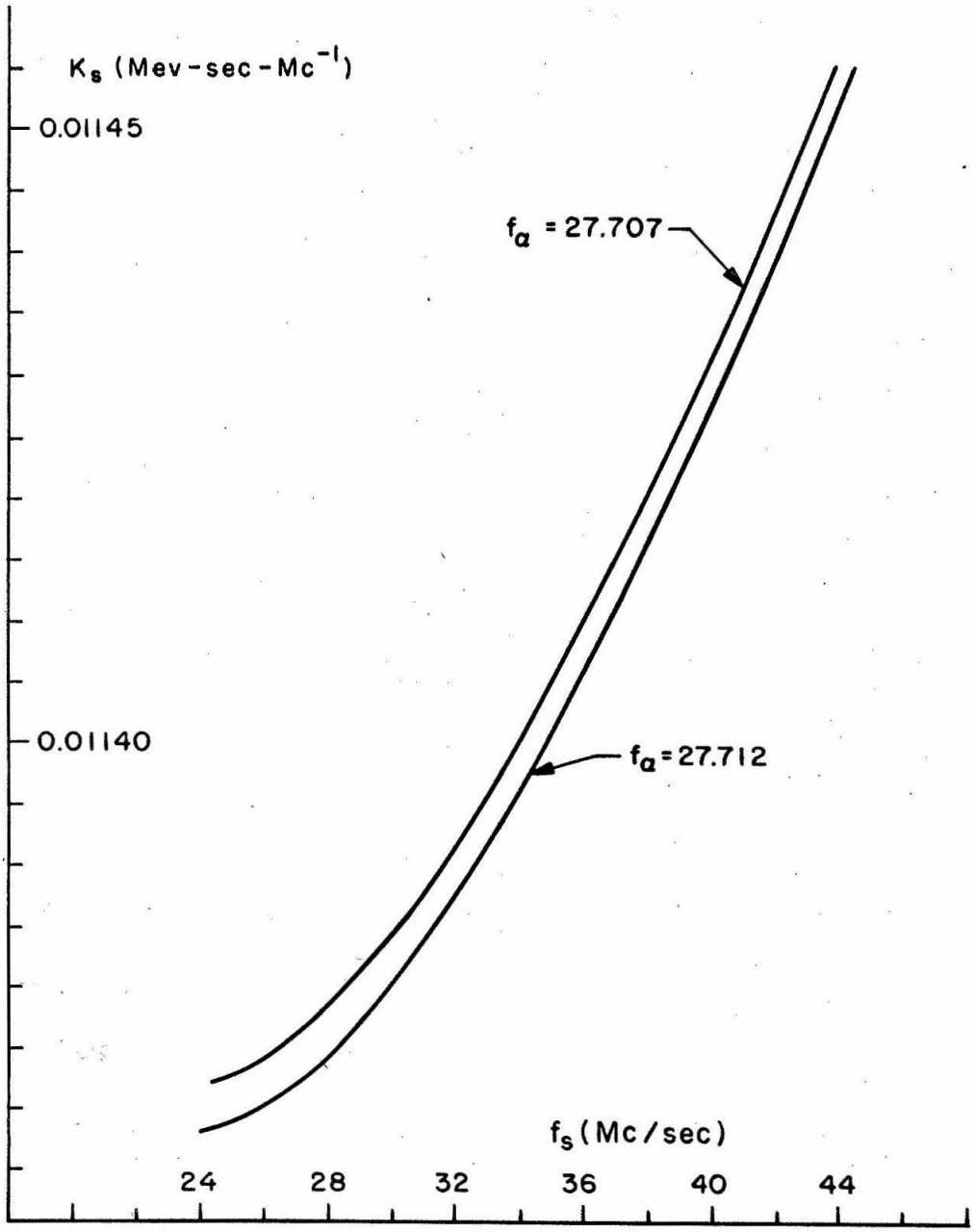
K_s (Mev-sec-Mc^{-1})
0.01145
0.01140
f_α = 27.707
f_α = 27.712
f_s (Mc/sec)
24
28
32
36
40
44

FIGURE 7: SAMPLE DATA OF A k_a DETERMINATION

Figure 7a shows a Bi^{212} alpha calibration used in conjunction with the He^{3++} pinhole data of Figure 7b to obtain a value for the analyzing magnet calibration constant (k_a). (See page 18.)

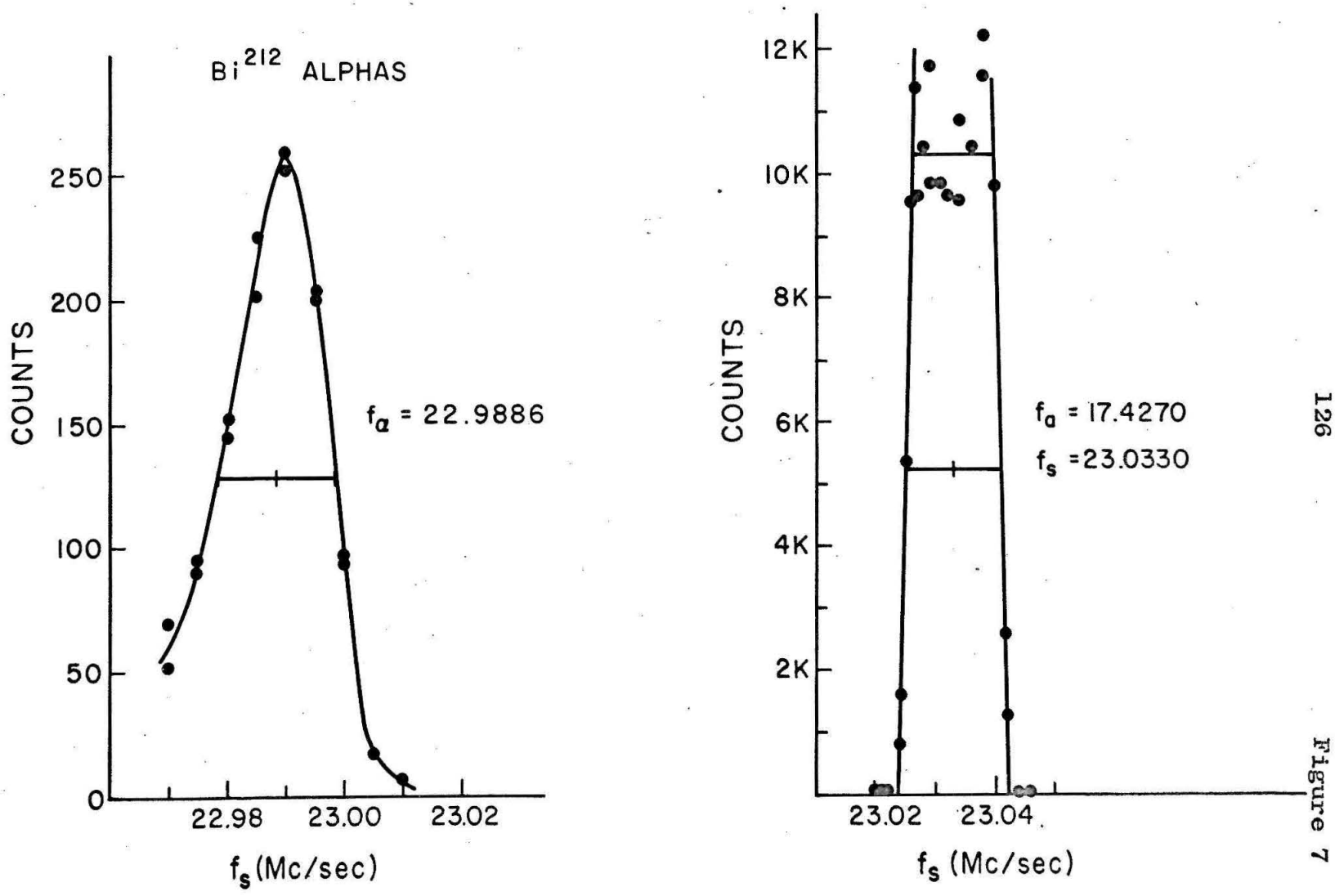
Bi^{212} ALPHAS
COUNTS
250
200
150
100
50
0
22.98
23.00
23.02
f_s (Mc/sec)
f_α = 22.9886
12K
10K
8K
6K
4K
2K
23.02
23.04
f_α = 17.4270
f_s = 23.0330

Figure 7

FIGURE 8: $K^{39}(d, \alpha)Ar^{37}$ SPECTRA SHOWING Ar^{37} EXCITED STATES $\lesssim$ 4.5 MeV

$K^{39}(d, \alpha)Ar^{37}$ alpha spectra at 30° and 150° showing Ar^{37} excited states between 0 and 4.5 MeV are shown in Figure 8a. Figure 8b shows spectra of the same resolution at 60°, 90°, 120°, and 140° for the excitation region between 3.5 and 4.5 MeV. Typical experimental resolutions are indicated on the 150° spectra. The ordinate marks indicate 50-count intervals. In Figure 8a the 30° and 150° spectra abscissas have been shifted to align Ar^{37} states vertically. The additional frequency shift for an Ar^{39} state between 30° and 150° is 180 kc/sec; if the ground state of Ar^{37} seen at 30° were an Ar^{39} state, the state would appear at the arrow labeled X at 150°. The position of a level at 2.41 MeV in Ar^{37} is indicated by the arrow labeled 2.41. (See pages 24ff., 46, 48.)

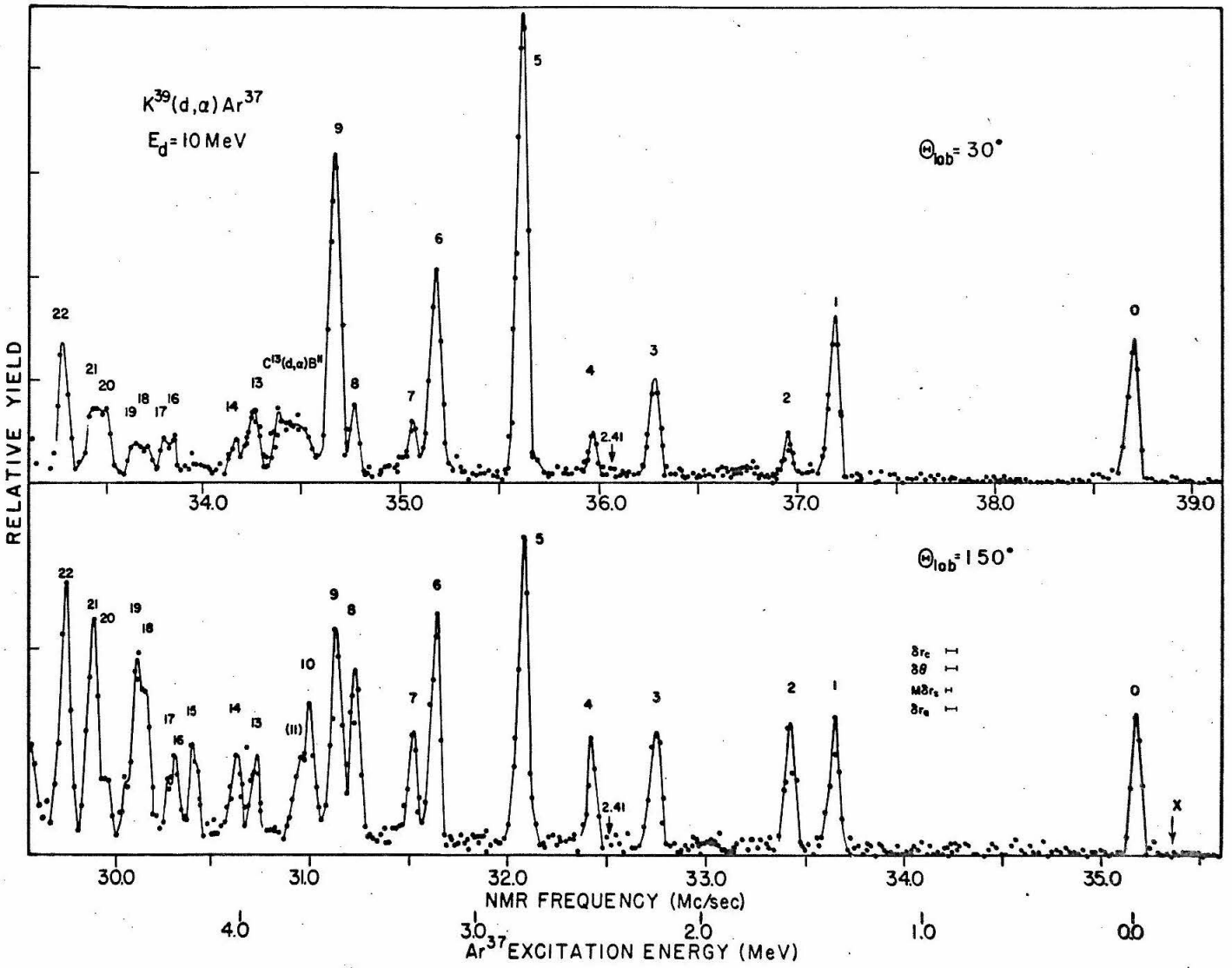
$K^{39}(d,\alpha)Ar^{37}$
E_d = 10 MeV
Θ_{lab} = 30°
Θ_{lab} = 150°
$C^{13}(d,\alpha)B^{11}$
2.41
RELATIVE YIELD
NMR FREQUENCY (Mc/sec)
Ar^{37} EXCITATION ENERGY (MeV)
δr_c
$\delta\theta$
$M\delta r_c$
δr_a

Figure 8a

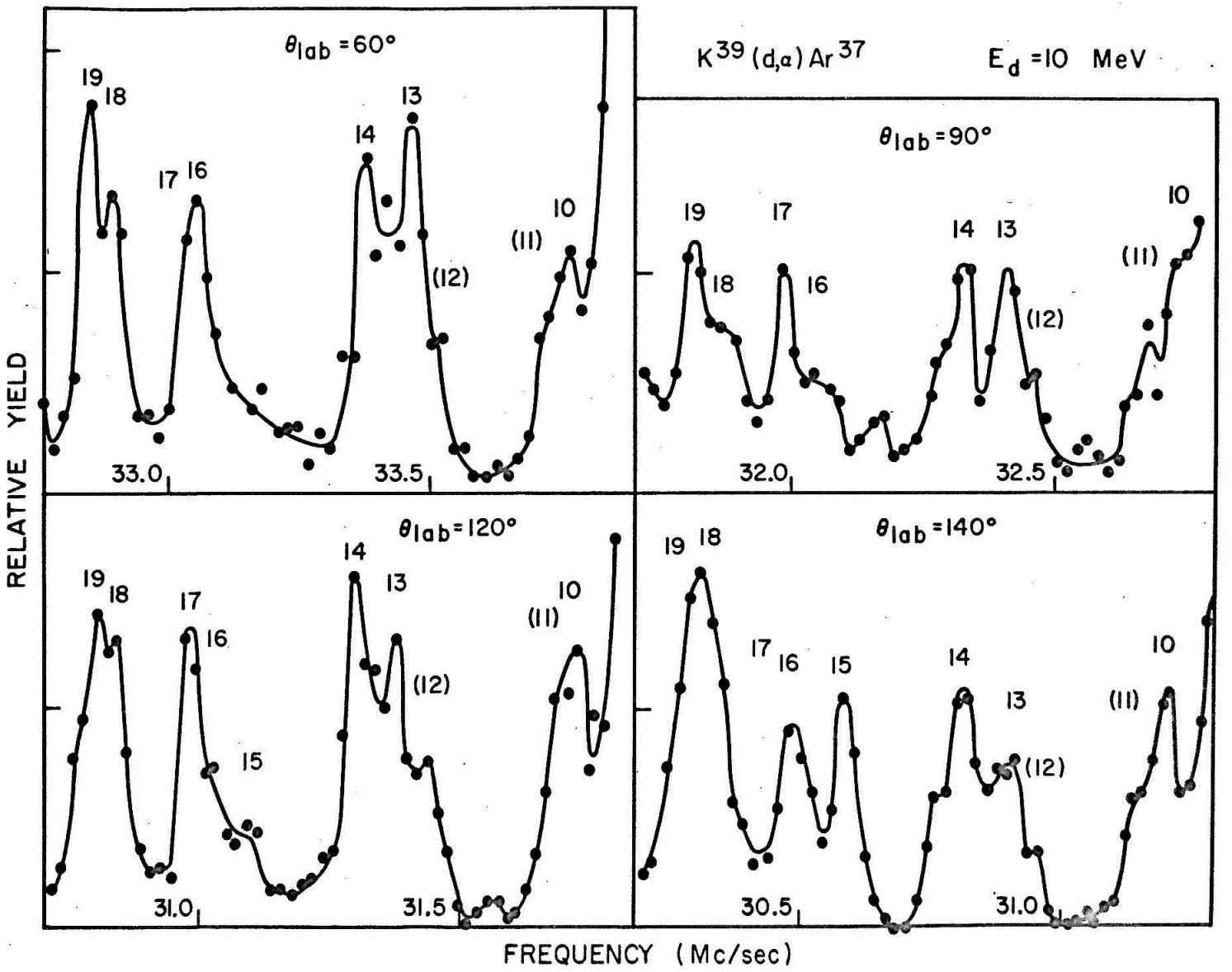
$K^{39}(d,\alpha)Ar^{37}$
E_d =10 MeV
θ_{lab} =60°
θ_{lab} =90°
θ_{lab} =120°
θ_{lab} =140°
RELATIVE YIELD
FREQUENCY (Mc/sec)
33.0
33.5
32.0
32.5
31.0
31.5
30.5
31.0

Figure 8b

FIGURE 9: SCHEMATIC TOP VIEW OF SCATTERING CHAMBER

The shaded areas indicate the angles at which the detector was placed in order to obtain the $K^{39}(d,\alpha)Ar^{37}$ angular distributions at $E_d = 10$ MeV. No change of target position is required for data taken at any angle. The KBr target surface was closest to the incoming beam; the carbon backing was closest to the beam catcher. (See page 32.)

Figure 9

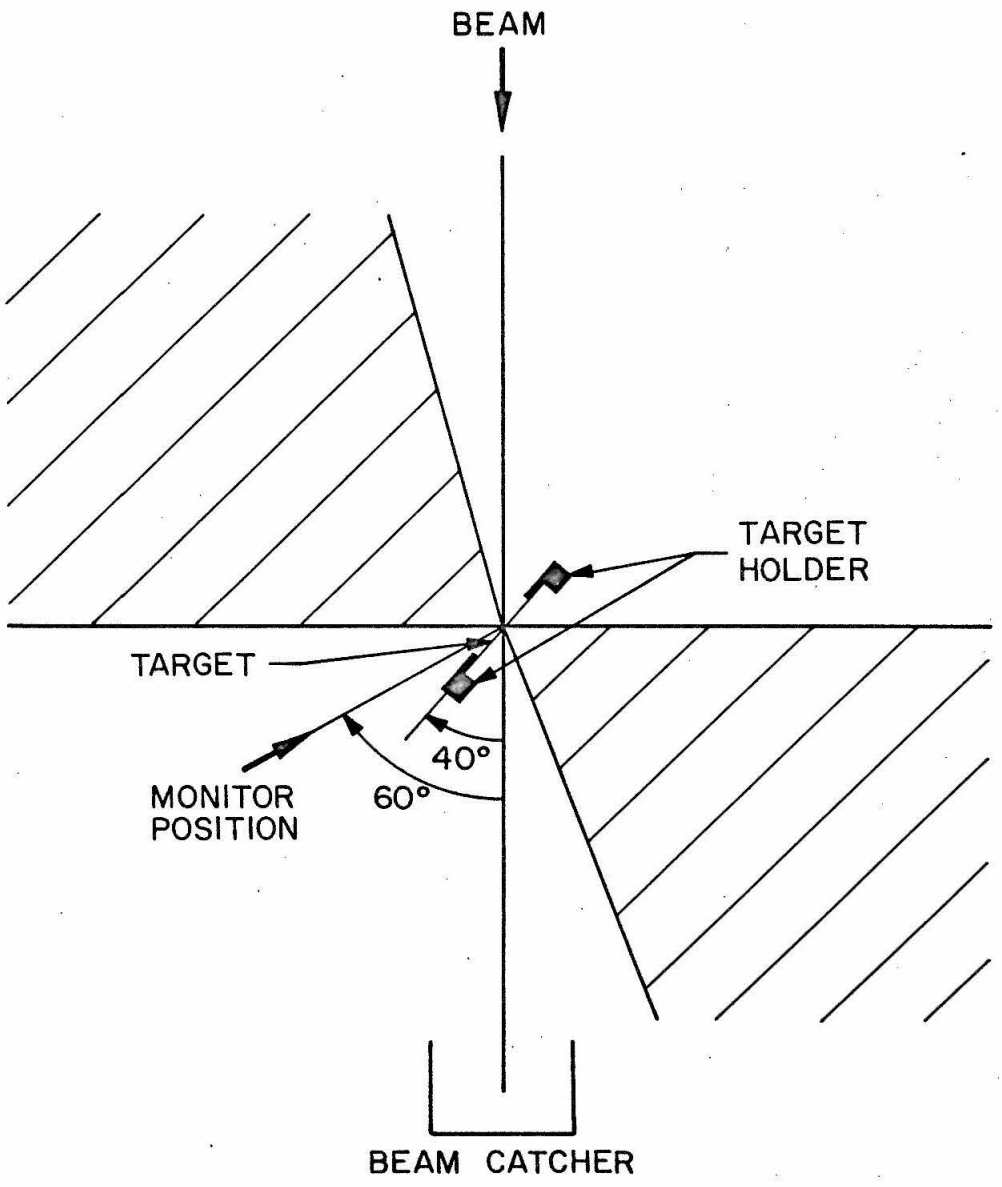
BEAM
TARGET HOLDER
TARGET
40°
60°
MONITOR POSITION
BEAM CATCHER

FIGURE 10: SOLID STATE DETECTOR SPECTRUM

The angular distributions of the lowest six Ar^{37} levels were derived from this and similar spectra extending from $20^{o} \leq \theta_{lab} \leq 165^{o}$. (See page 32.)

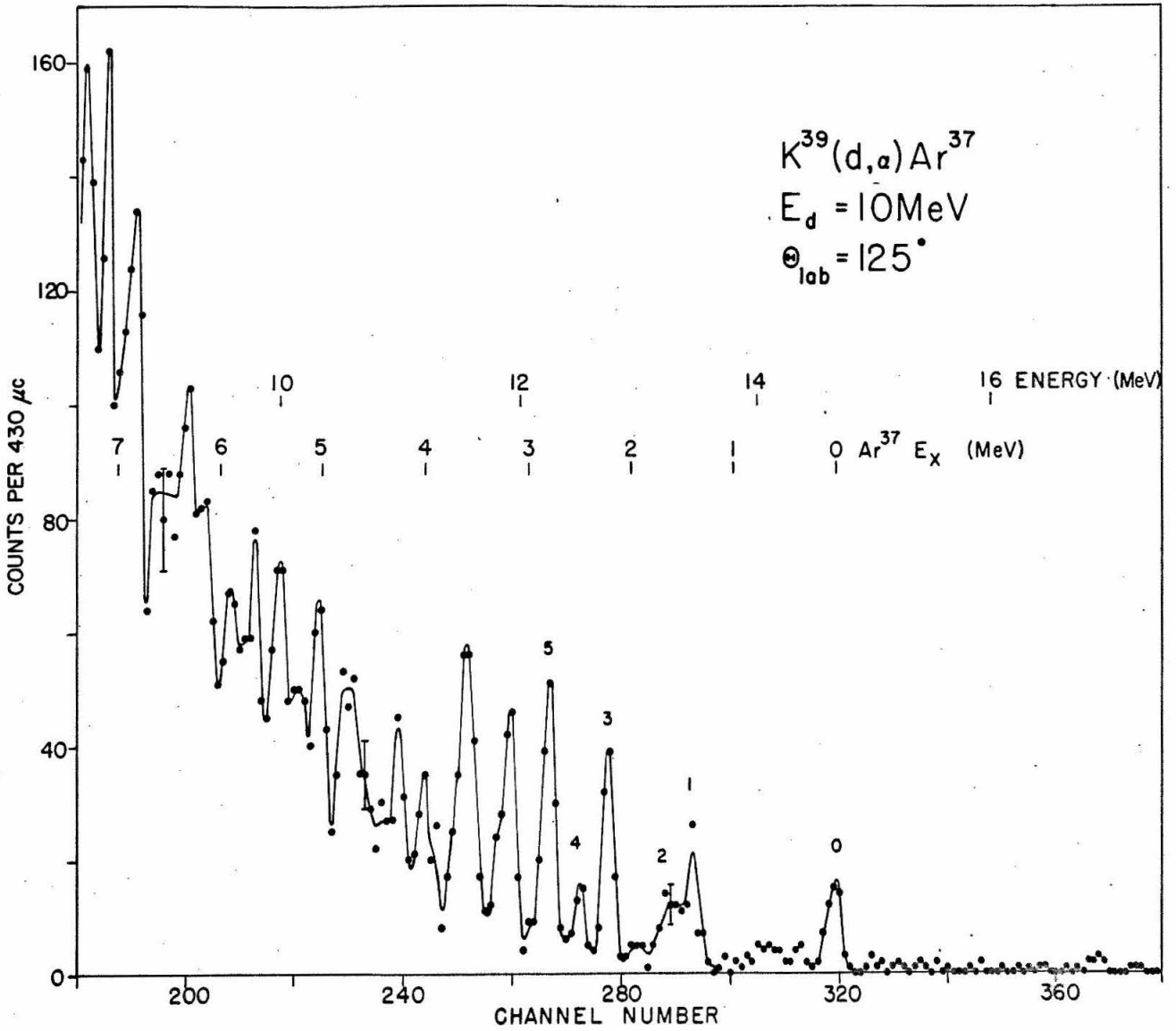
$K^{39}(d,\alpha)Ar^{37}$
E_d = 10MeV
Θ_{lab} = 125°
COUNTS PER 430 μc
CHANNEL NUMBER
ENERGY (MeV)
Ar^{37} E_x (MeV)
160
120
80
40
0
200
240
280
320
360
10
12
14
16
7
6
5
4
3
2
1
0
5
3
4
2
1
0

Figure 10

FIGURE 11: $K^{39}(d,\alpha)Ar^{37}$ ANGULAR DISTRIBUTIONS OF THE LOWEST SIX Ar^{37} LEVELS AT $E_d = 10$ MeV.

The ordinates of each of the six plots are the same. Each ordinate mark represents approximately one hundred detected events. The solid curves are drawn to aid the eye and typical error bars are shown. Open circled data points have larger uncertainties owing to contaminant background subtraction. (See pages 34f.)

Figure 11

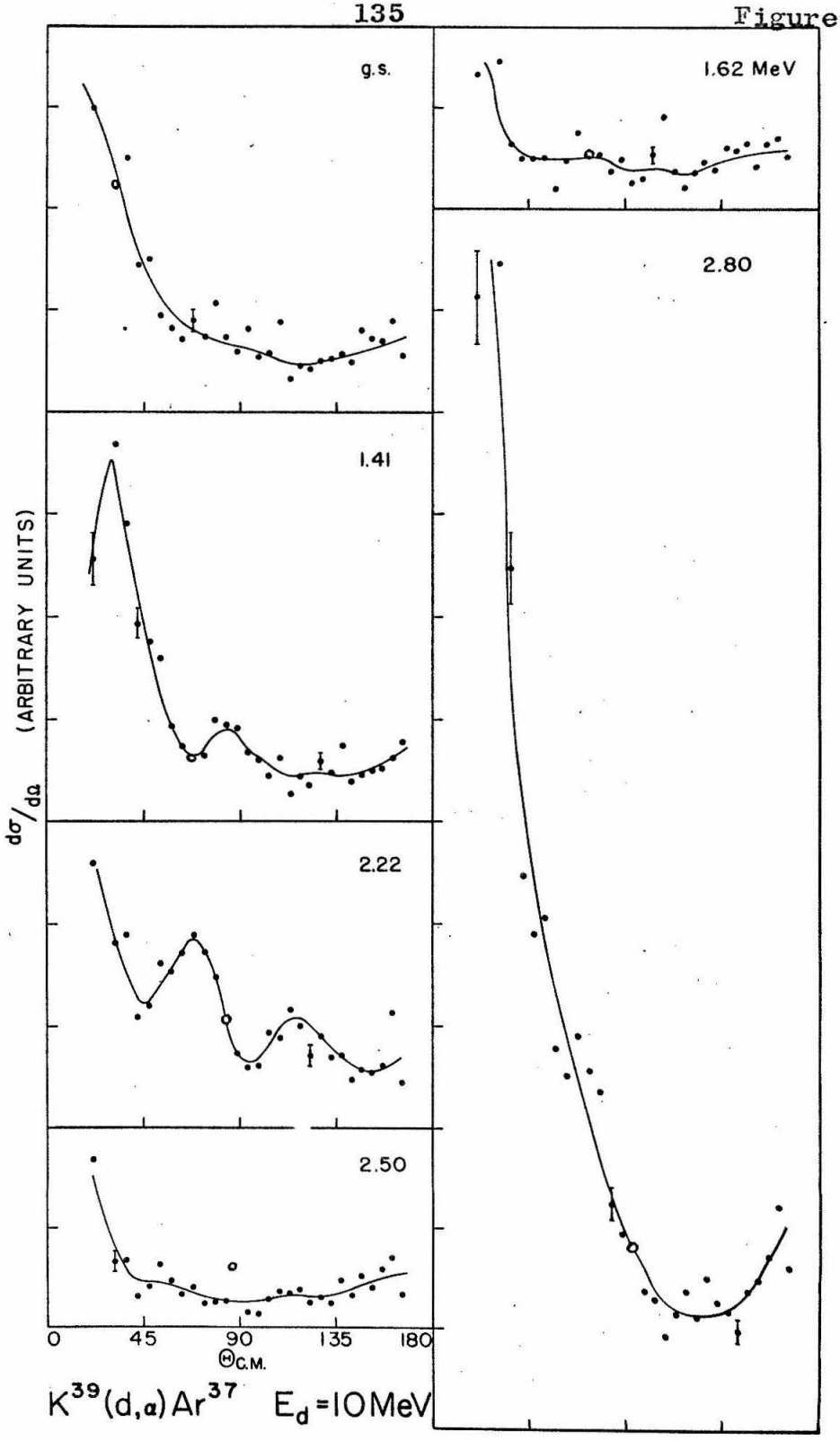
g.s.
1.62 MeV
2.80
1.41
2.22
2.50
dσ/dΩ (ARBITRARY UNITS)
0
45
90
135
180
Θc.m.
K39(d,α)Ar37 Ed=10MeV

FIGURE 12: $K^{39}(d,\alpha)Ar^{37}$ LEVELS - $4.5 < E_x < 5.5$ MeV

Ar^{37} level data, collected using the $K^{39}(d,\alpha)Ar^{37}$ reaction, are shown in this figure. The six alpha spectra were obtained at $\theta_{cm} = 20^{\circ}$, 30°, 40°, 70°, 110°, and 140°. The approximate excitation energy scale is indicated on the 20° spectrum. Yield factor corrections have been made. Levels are numbered as in Table IV. Unidentified groups are labeled X. The peaks that are reduced by a factor of 3 in the 20° and 30° spectra are caused by the contaminant $O^{16}(d,\alpha)N^{14}$ ground state reaction. Two triangles from the cross section decomposition have been included in the 70° spectrum. (See pages 28, 50f., 64.)

Figure 12
(a)

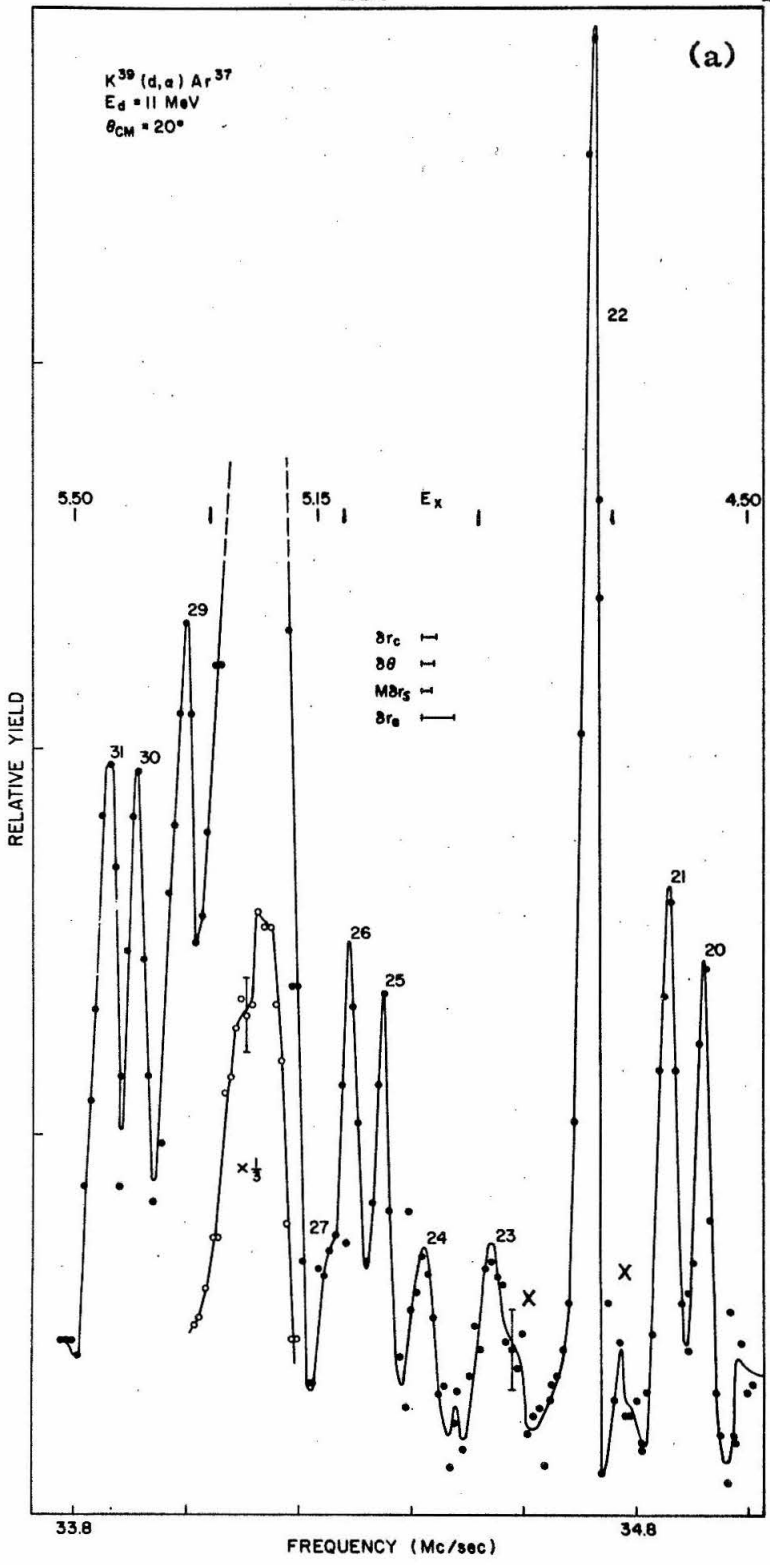
(a)
$K^{39}(d,\alpha)Ar^{37}$
E_d = 11 MeV
θ_{CM} = 20°
5.50
5.15
E_x
4.50
δr_c
$\delta\theta$
$M\delta r_S$
δr_a
RELATIVE YIELD
FREQUENCY (Mc/sec)
33.8
34.8
22
29
31
30
26
25
27
24
23
21
20
X
X
X 1/3

Figure 12
(b)

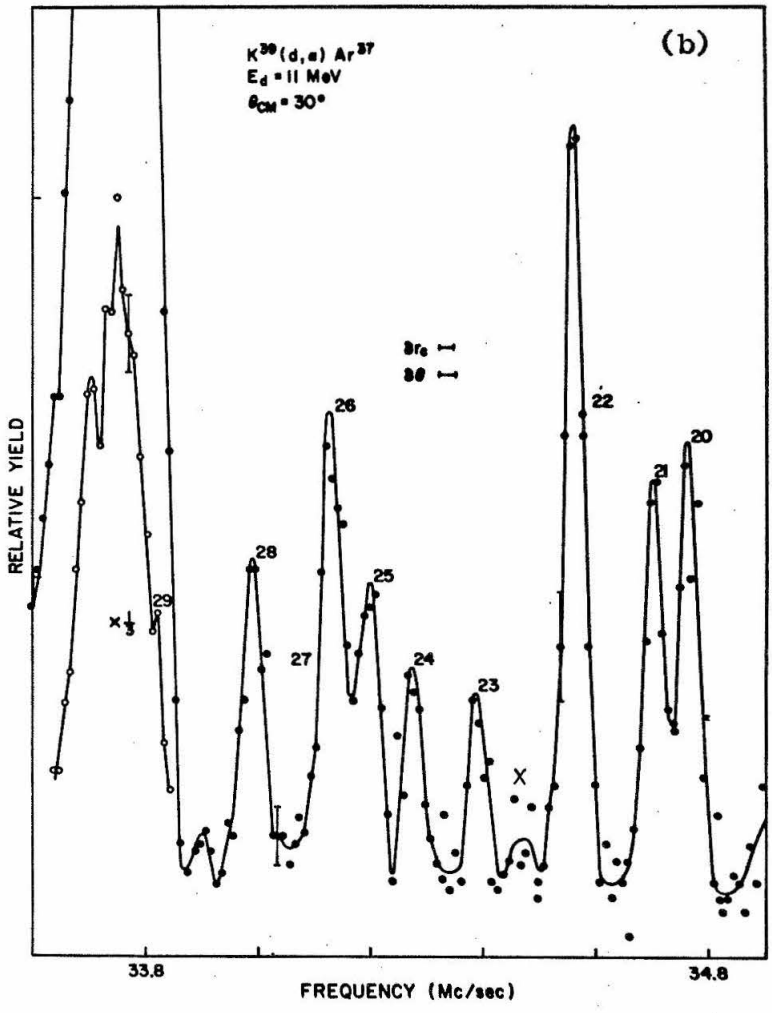
(b)
$K^{39}(d,\alpha)\ Ar^{37}$
E_d = 11 MeV
θ_{CM} = 30°
δr_c
$\delta\theta$
RELATIVE YIELD
FREQUENCY (Mc/sec)
33.8
34.8
×1/3
20
21
22
23
24
25
26
27
28
29
X

Figure 12
(c) & (d)

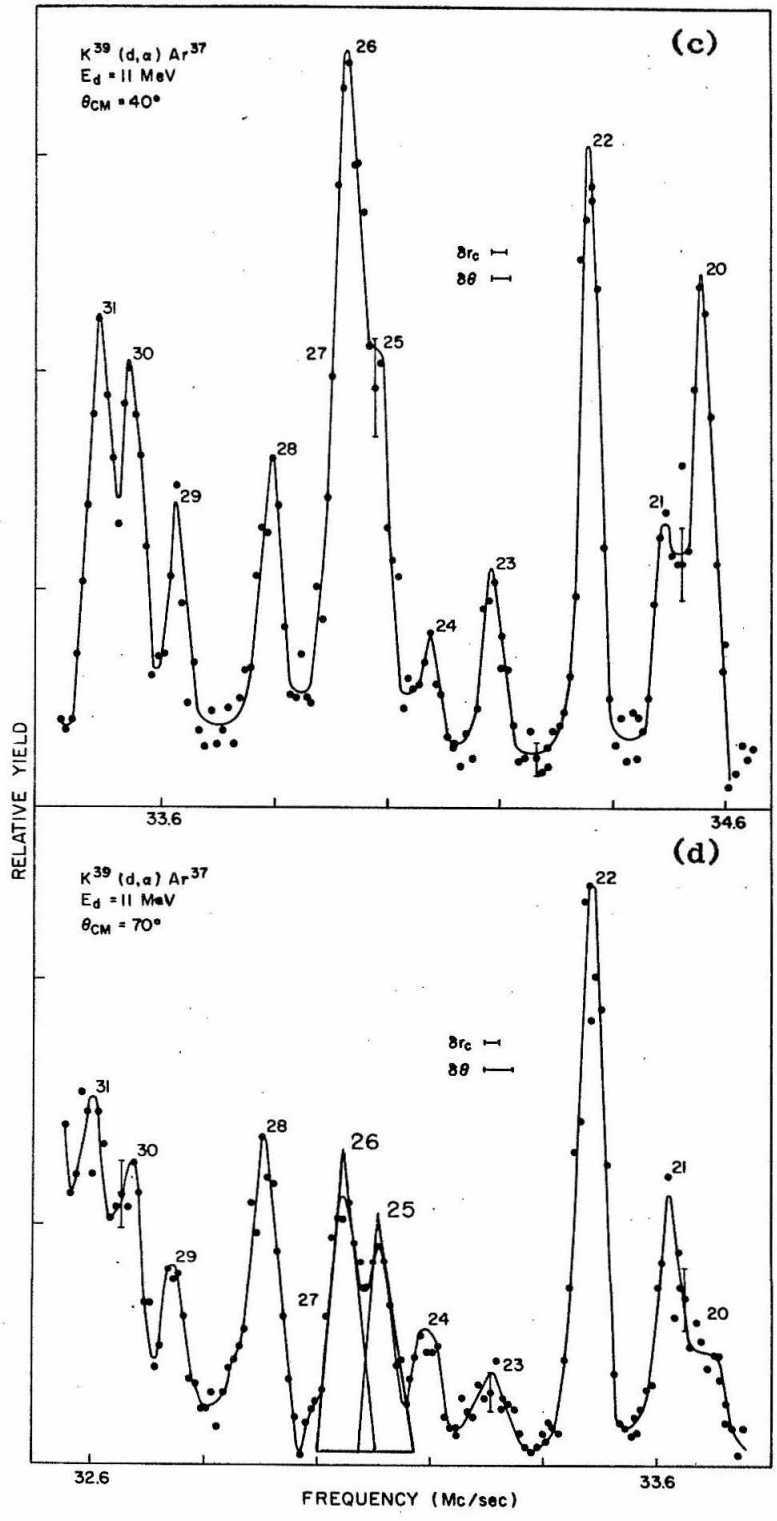
(c)
K39 (d,α) Ar37
Ed = 11 MeV
θCM = 40°
δrc
δθ
31
30
29
28
27
26
25
24
23
22
21
20
33.6
34.6
(d)
K39 (d,α) Ar37
Ed = 11 MeV
θCM = 70°
δrc
δθ
31
30
29
28
27
26
25
24
23
22
21
20
32.6
33.6
RELATIVE YIELD
FREQUENCY (Mc/sec)

Figure 12
(e) & (f)

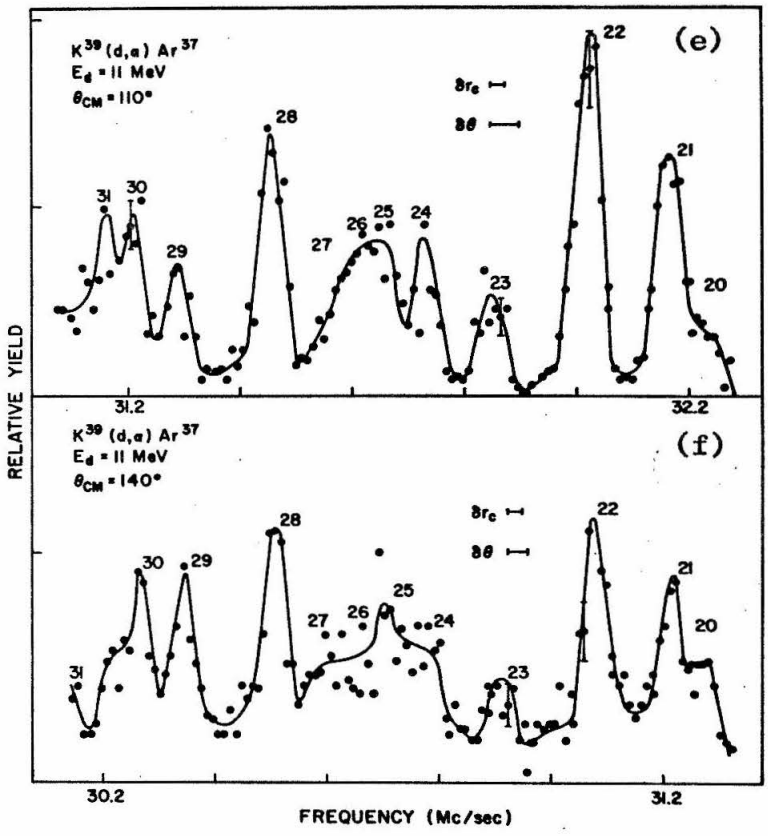
K39 (d,α) Ar37
Ed = 11 MeV
θCM = 110°
δrc
δθ
(e)
31
30
29
28
27
26
25
24
23
22
21
20
31.2
32.2
K39 (d,α) Ar37
Ed = 11 MeV
θCM = 140°
(f)
30.2
31.2
RELATIVE YIELD
FREQUENCY (Mc/sec)

FIGURE 13: $K^{39}(d,\alpha)Ar^{37}$ ANGULAR DISTRIBUTIONS OF Ar^{37} LEVELS $4.5 < E_x < 5.5$ MeV AT $E_d = 11$ MeV

The relative differential cross sections extracted from the spectra of Figure 12 are shown. The levels are numbered as in Figure 12 (Table IV).

Level number	Ar^{37} energy
20	4.58
21	4.63
22	4.75
23	4.89
24	4.99
25	5.06
26	5.11
27	5.14
28	5.22
29	5.35
30	5.42
31	5.46

Solid curves connect the data points. The data for the 5.14-MeV level (open circles)are plotted with the level of smallest cross section. The open-circled points are measured cross sections for 20° and 140° and upper limits for the remaining angles. (See pages 51, 65.)

Figure 13

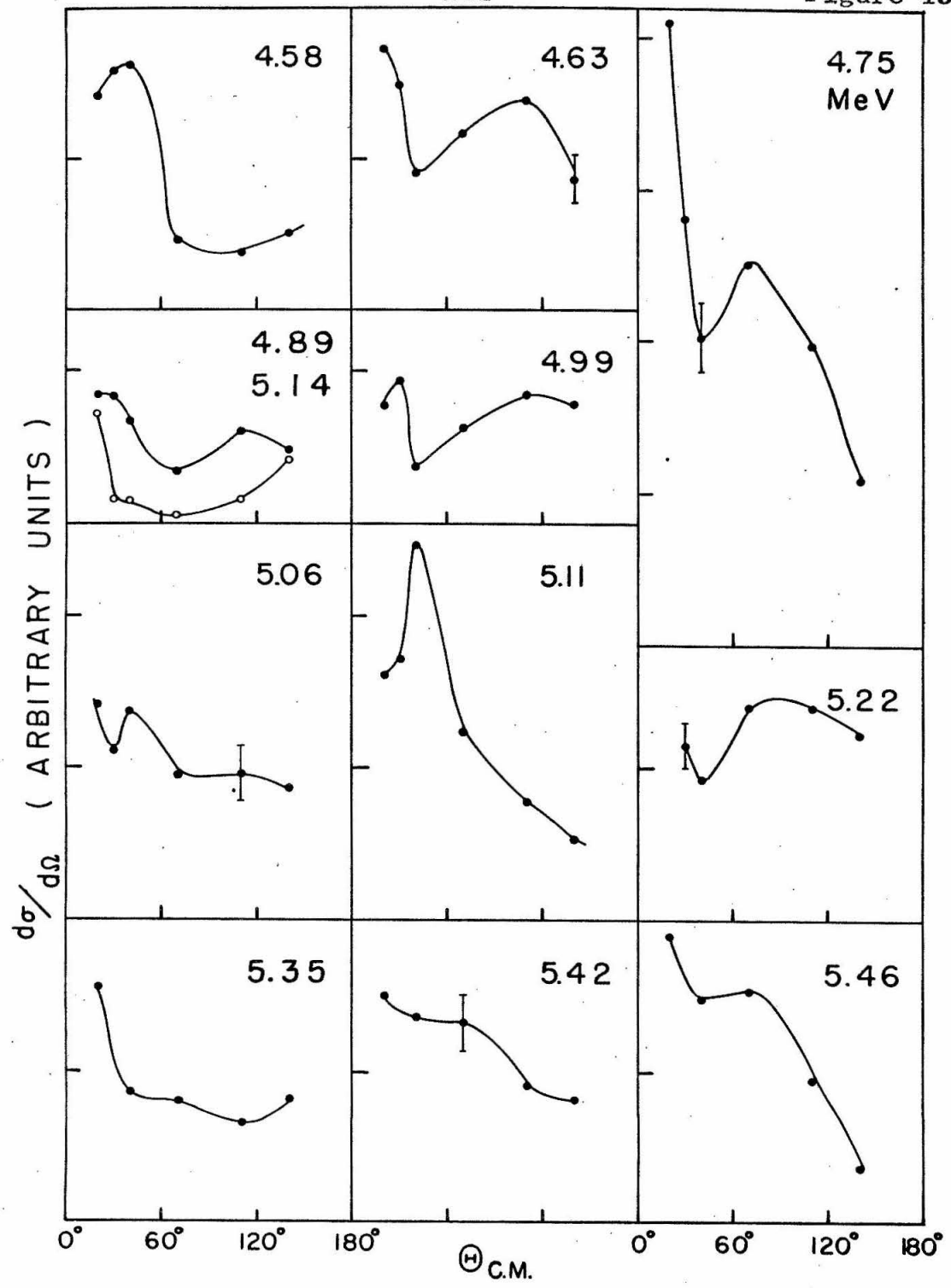
4.58
4.63
4.75
MeV
4.89
5.14
4.99
5.06
5.11
5.22
5.35
5.42
5.46
dσ/dΩ (ARBITRARY UNITS)
0°
60°
120°
180°
Θ C.M.

FIGURE 14: VACUUM EVAPORATION OF $BaCl_2^{35}$

The tantalum $BaCl_2^{35}$ holder is shown in (a). The reservoir is pressed into the sheet with a ball bearing. Notches provide local heating of the reservoir. (b) shows the holder and heat shields in position between the electrodes. The target holders are located 2.5 and 3.5 cm above the holder. (See pages 53f.)

Figure 14

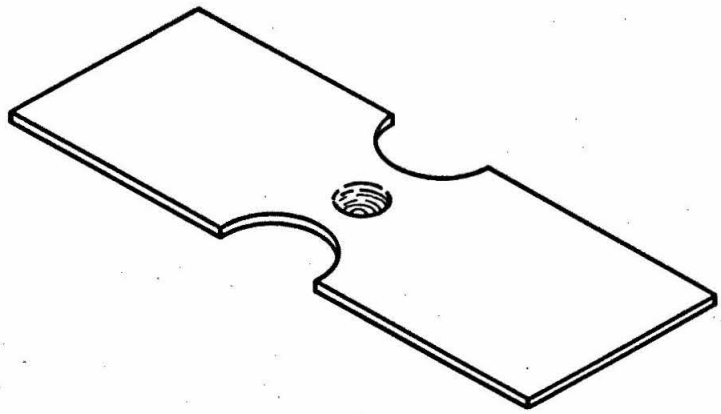

(a)

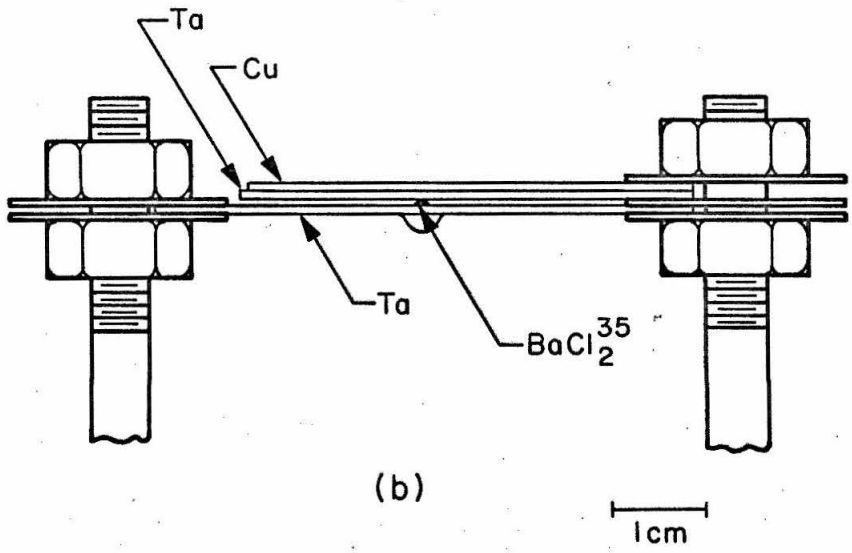

(b)

FIGURE 15: $Cl^{35}(He^{3},p)Ar^{37}$ $4.6 < E_x < 5.9$ MeV

Ar^{37} level data collected using the $Cl^{35}(He^{3},p)Ar^{37}$ reaction with natural chlorine targets are shown in this figure. The two proton spectra were obtained at $\theta_{lab} = 30^{o}$ and 80^{o}. The approximate excitation energy scale is indicated on the 30^{o} spectrum. Levels are numbered as in Table IV. Ordinate tick marks indicate one hundred counts. (See page 55.)

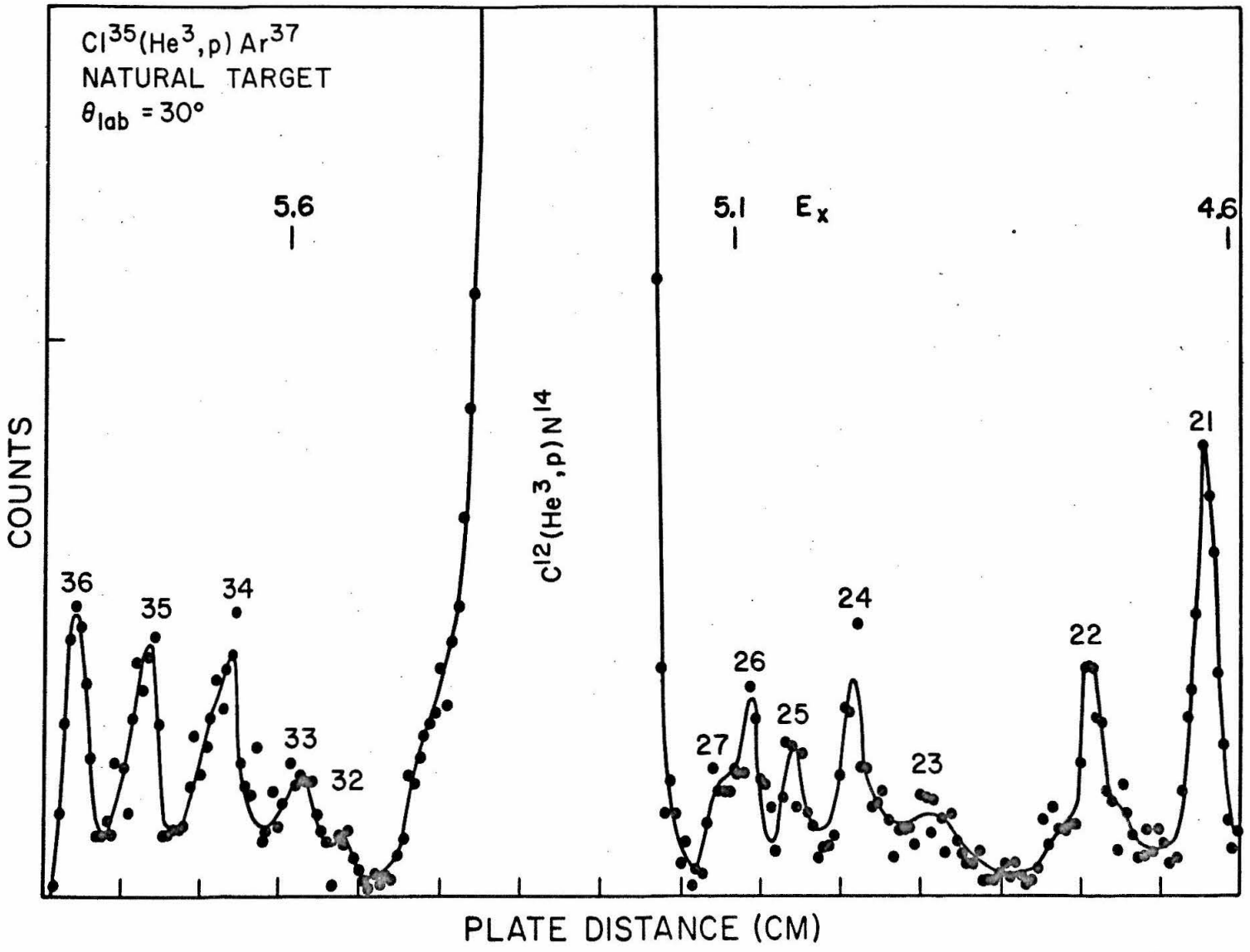
Cl35(He3,p) Ar37
NATURAL TARGET
θlab = 30°
5.6
5.1
Ex
4.6
C12(He3,p)N14
COUNTS
PLATE DISTANCE (CM)
36
35
34
33
32
27
26
25
24
23
22
21

Figure 15a

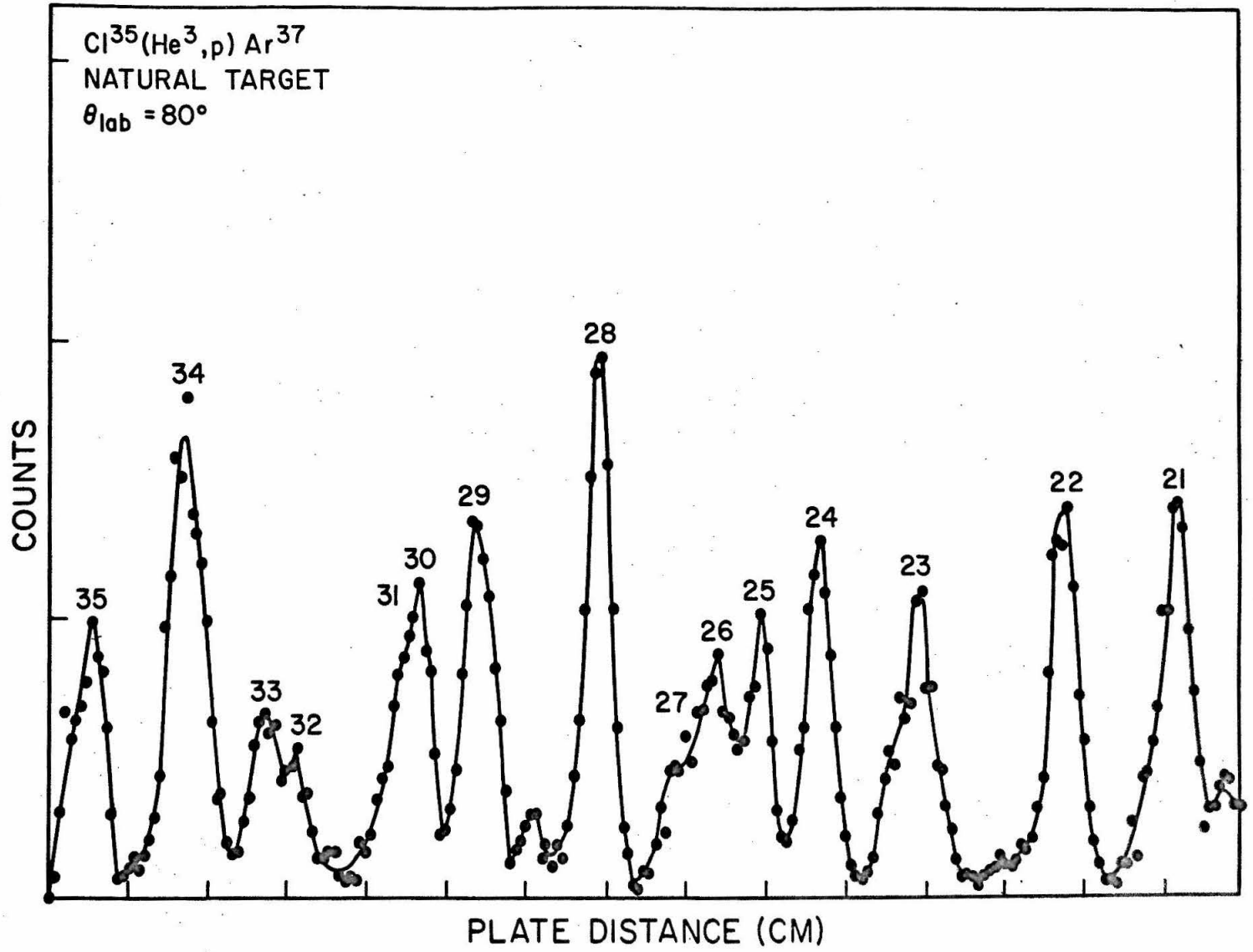
$Cl^{35}(He^3,p)\,Ar^{37}$
NATURAL TARGET
$\theta_{lab} = 80°$
COUNTS
PLATE DISTANCE (CM)
35
34
33
32
31
30
29
28
27
26
25
24
23
22
21

Figure 15b

FIGURE 16: $Cl^{35}(He^{3},p)Ar^{37}$ $4.6 < E_x < 5.9$ MeV

Ar^{37} level data collected using the $Cl^{35}(He^{3},p)Ar^{37}$ reaction with enriched targets are shown in this figure. The five spectra were obtained at $\theta_{lab} = 30^{o}$, 40^{o}, 60^{o}, 80^{o}, and 150^{o}. The 30^{o} and 80^{o} spectra may be compared with the similar natural target spectra of Figure 15. The approximate excitation energy scale is indicated on the 30^{o} spectrum. Levels are numbered as in Table IV. Ordinate tick marks indicate one hundred counts. (See pages 55 and 64.)

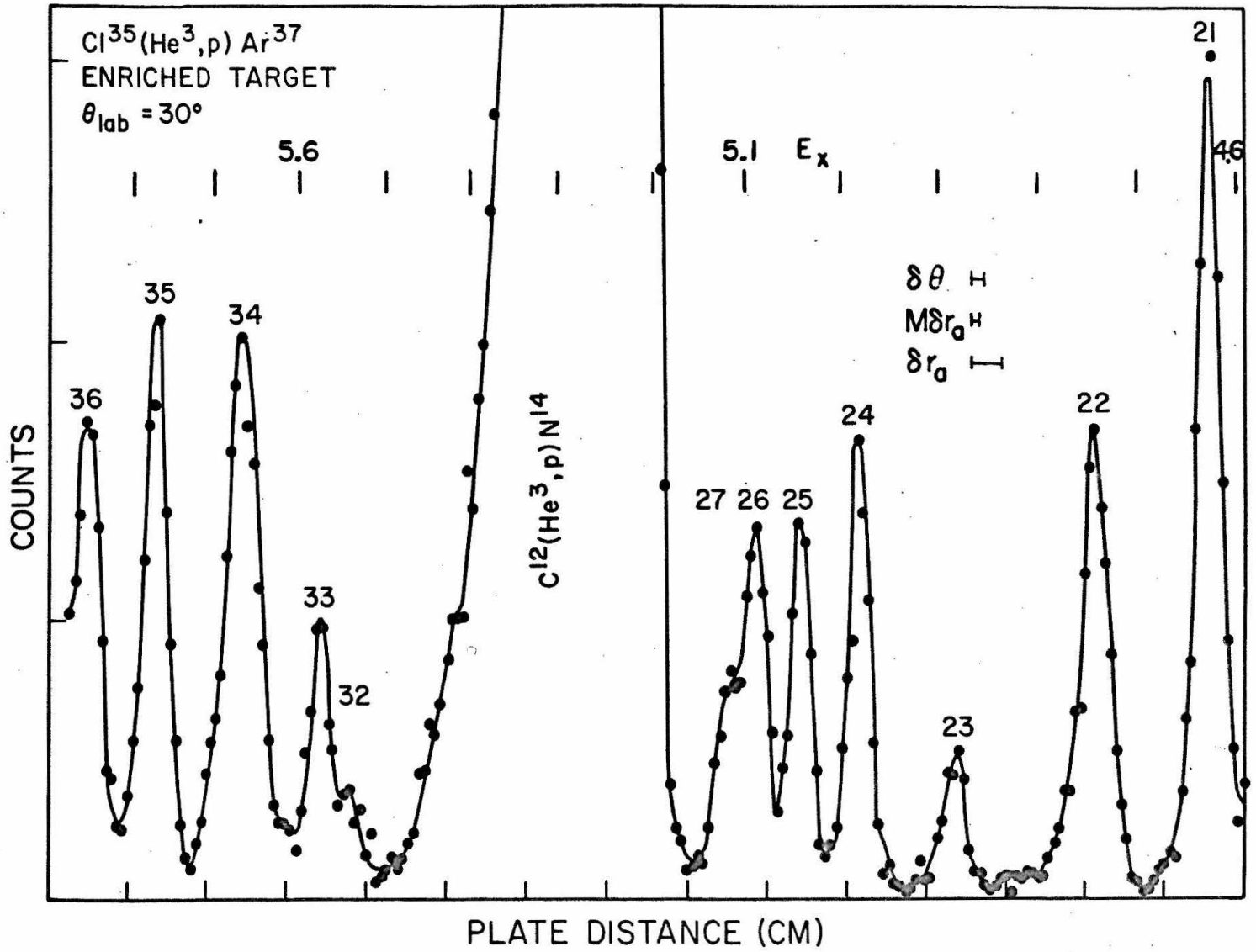
Cl35(He3,p) Ar37
ENRICHED TARGET
θlab = 30°
5.6
5.1 Ex
δθ
Mδra
δra
36
35
34
33
32
C12(He3,p)N14
27 26 25
24
23
22
21
46
COUNTS
PLATE DISTANCE (CM)

Figure 16a

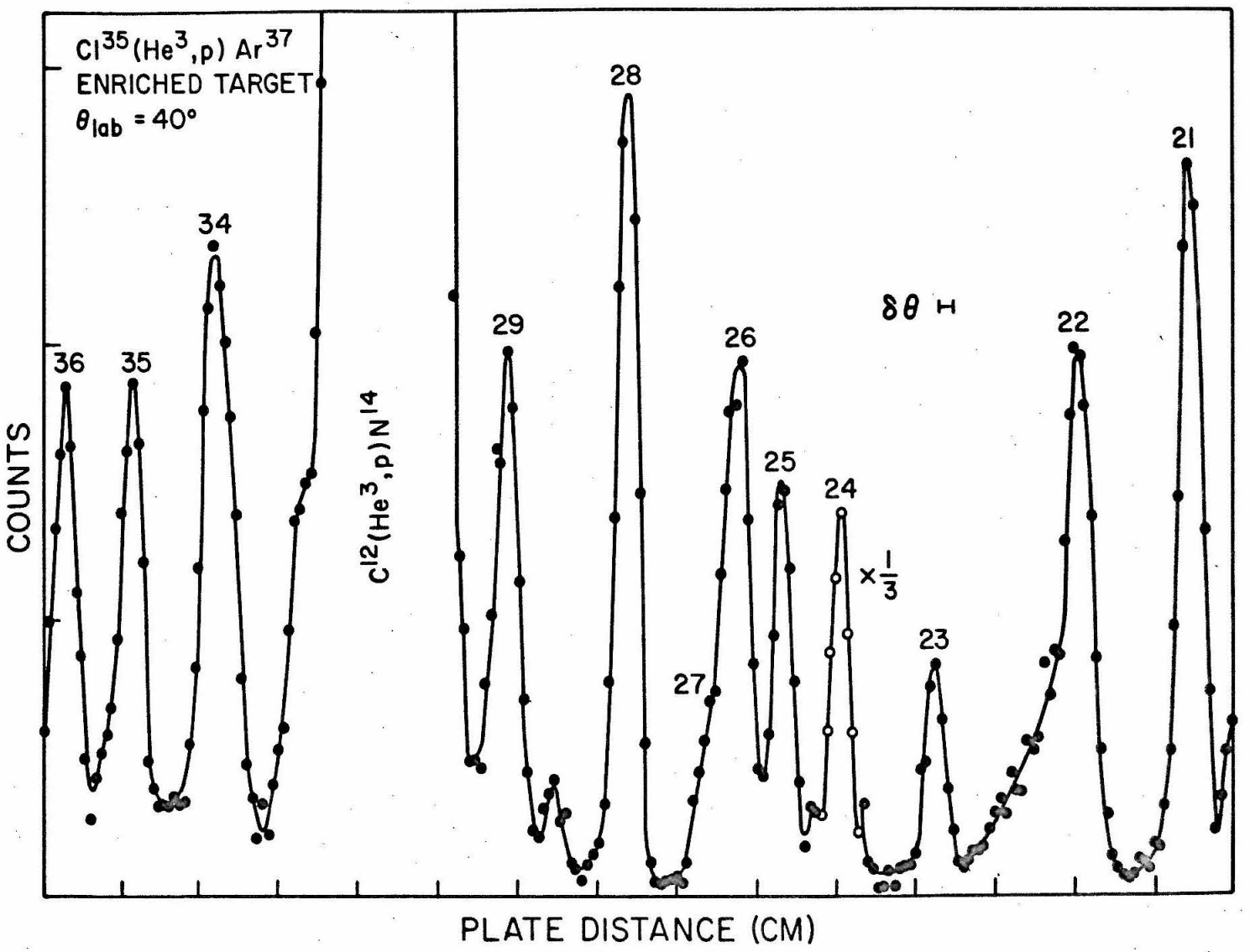
Cl35(He3,p) Ar37
ENRICHED TARGET
θlab = 40°
C12(He3,p)N14
δθ H
×1/3
COUNTS
PLATE DISTANCE (CM)
36
35
34
29
28
27
26
25
24
23
22
21

Figure 16b

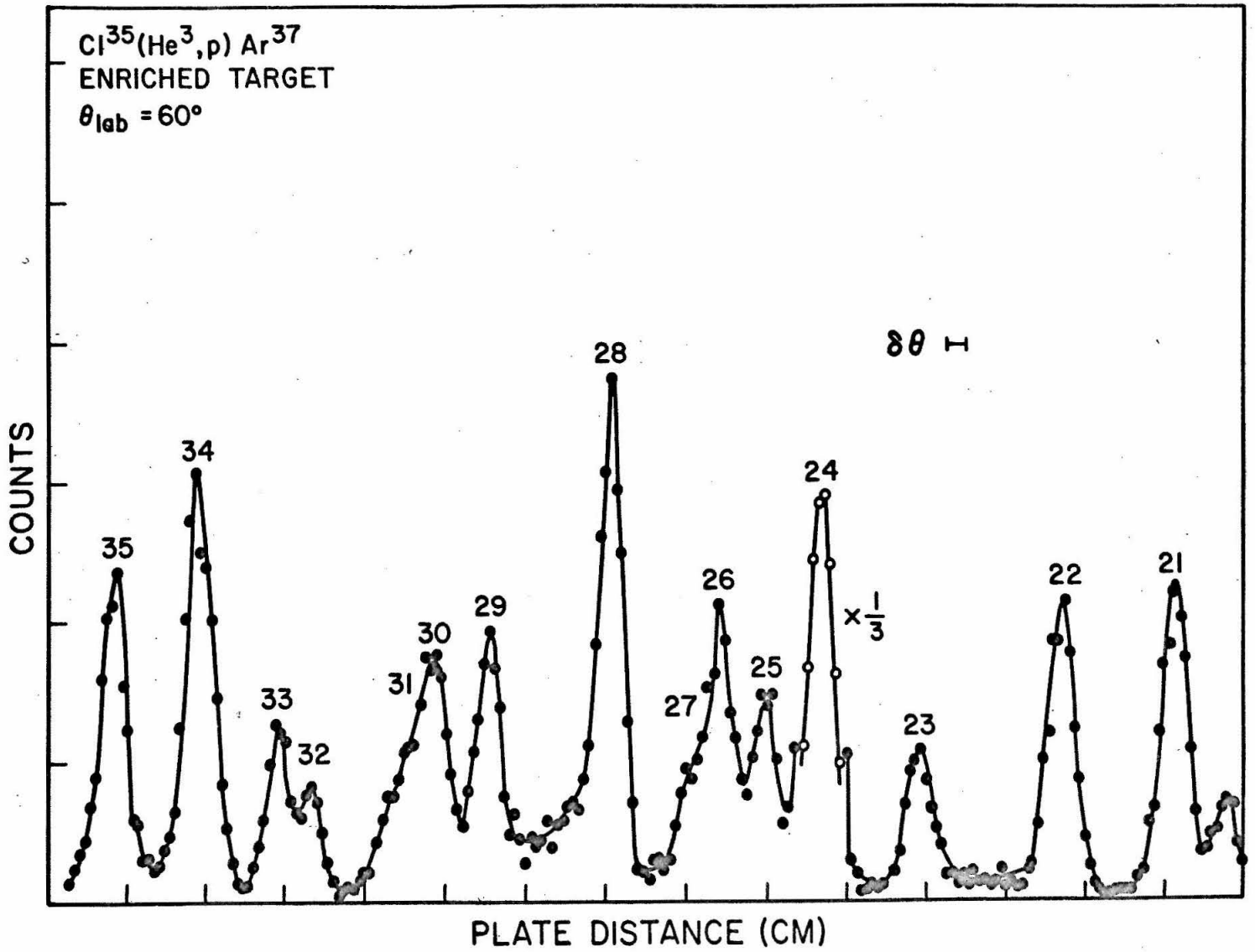
Cl35(He3,p) Ar37
ENRICHED TARGET
θlab = 60°
δθ I
COUNTS
PLATE DISTANCE (CM)
35
34
33
32
31
30
29
28
27
26
25
24
x 1/3
23
22
21

Figure 16c

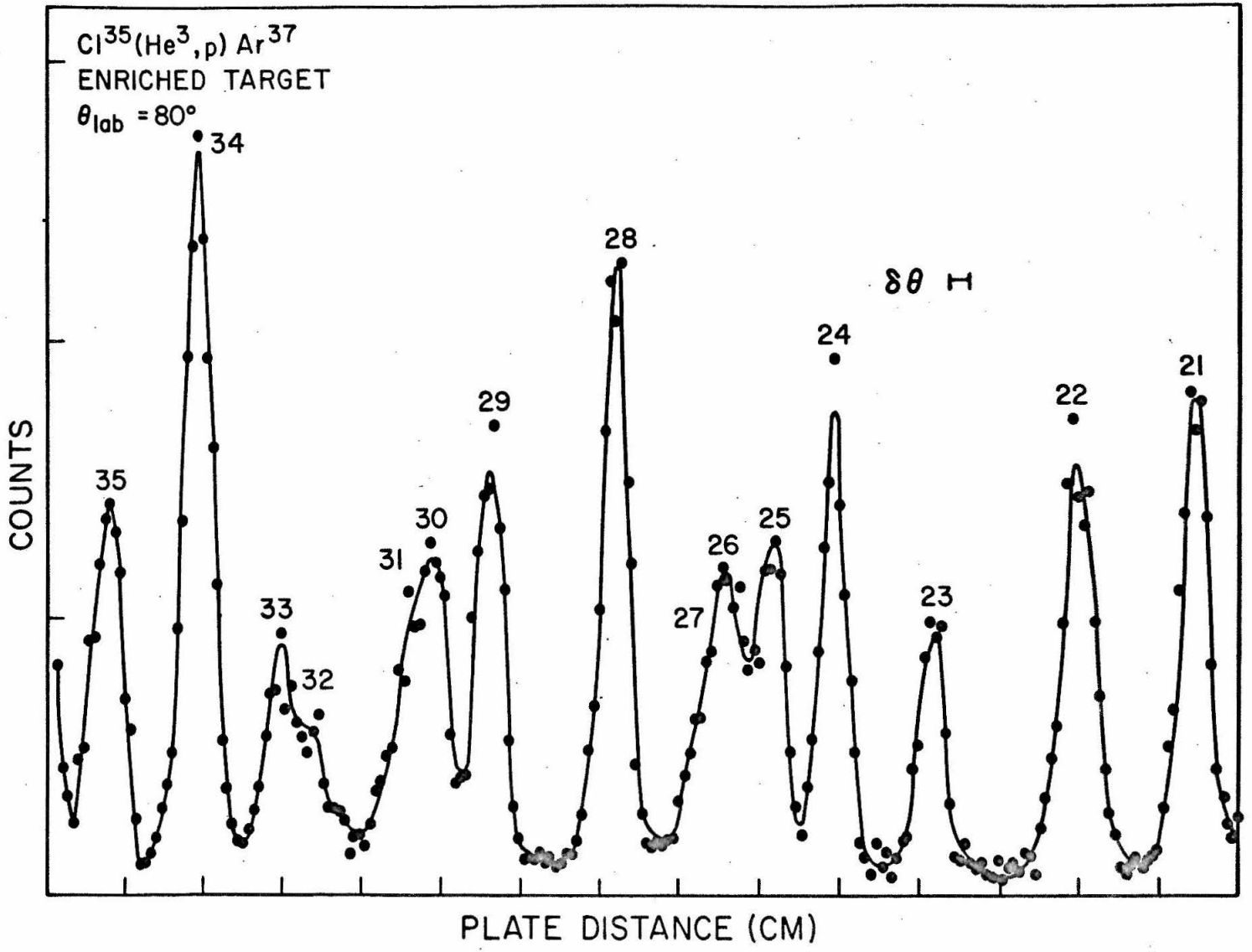
$Cl^{35}(He^3,p)\,Ar^{37}$
ENRICHED TARGET
$\theta_{lab} = 80°$
δθ
COUNTS
PLATE DISTANCE (CM)
35
34
33
32
31
30
29
28
27
26
25
24
23
22
21

Figure 16d

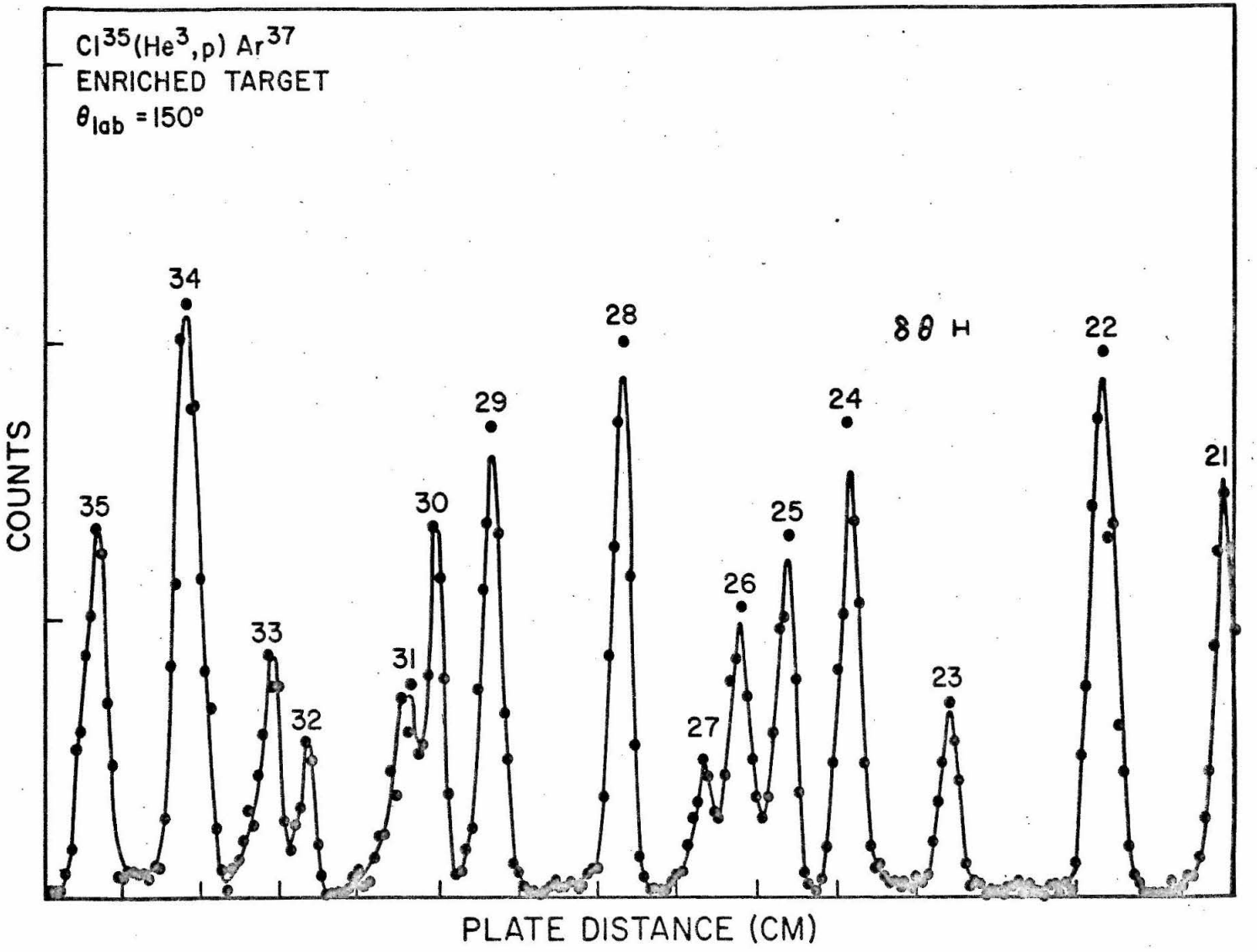
$Cl^{35}(He^3,p)\ Ar^{37}$
ENRICHED TARGET
$\theta_{lab} = 150°$
COUNTS
PLATE DISTANCE (CM)
δθ H
35
34
33
32
31
30
29
28
27
26
25
24
23
22
21

Figure 16e

FIGURE 17: ERICSON PLOT OF Ar^{37} LEVELS

An Ericson plot shows the number of Ar^{37} levels below a given excitation energy for the levels observed in this experiment listed in Table IV. The nuclear temperature determined from this plot is 1.4 MeV with temperatures of 1.2 and 1.6 MeV also shown. (See page 69.)

Figure 17

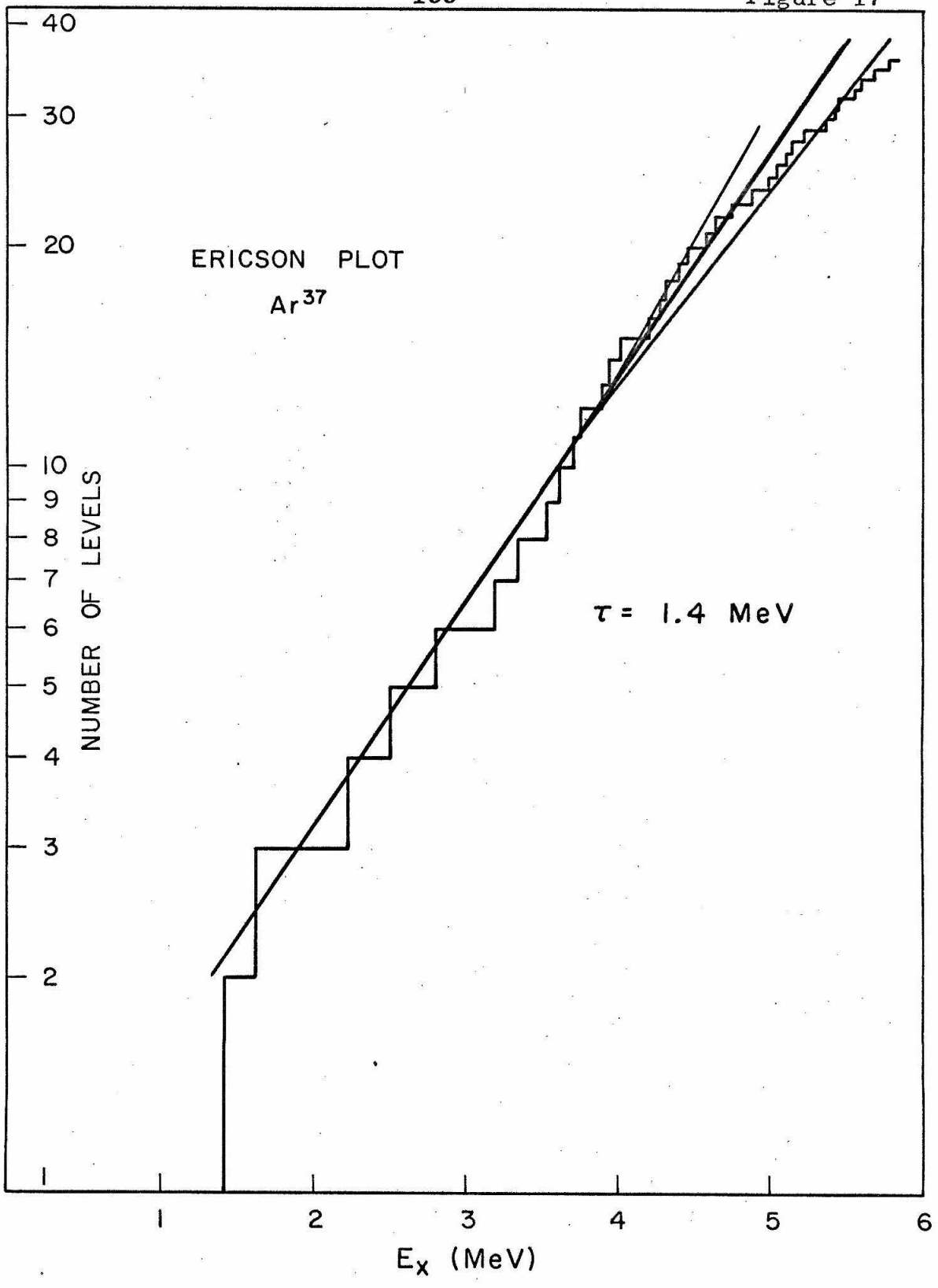
ERICSON PLOT
Ar37
τ = 1.4 MeV
NUMBER OF LEVELS
40
30
20
10
9
8
7
6
5
4
3
2
1
1
2
3
4
5
6
Ex (MeV)

FIGURE 18: BLOCK DIAGRAM OF NMR MAGNETOMETER

Two separate circuits are required to cover the spectrometer magnetic field range commonly used. These two circuits are designated as "high" and "low" in the figure referring to the higher and lower frequency ranges respectively. Solid lines differentiate apparatus located at the spectrometer from the apparatus located in the control area, which is indicated by broken lines. (See pages 73, 77.)

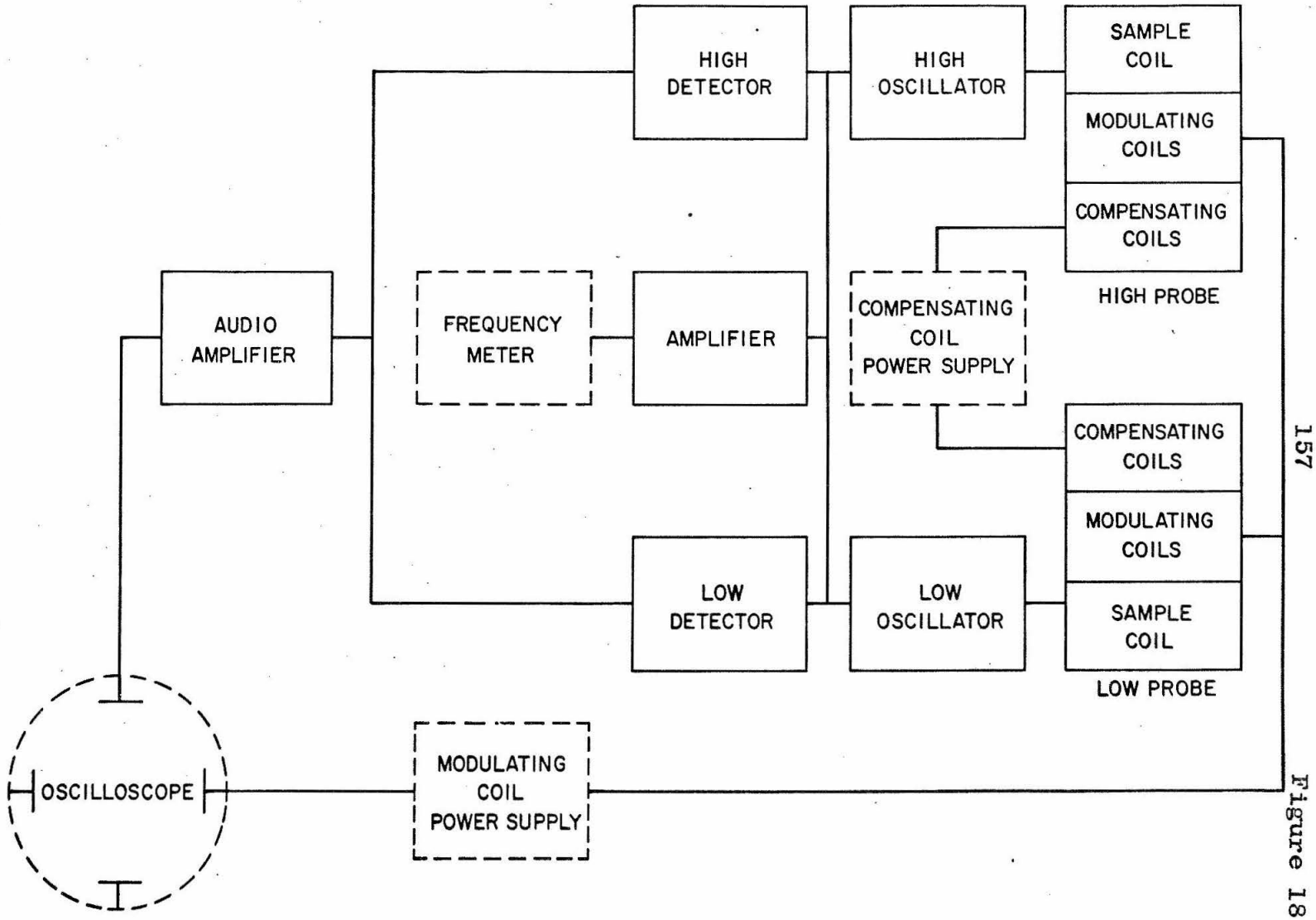
HIGH DETECTOR
HIGH OSCILLATOR
SAMPLE COIL
MODULATING COILS
COMPENSATING COILS
HIGH PROBE
AUDIO AMPLIFIER
FREQUENCY METER
AMPLIFIER
COMPENSATING COIL POWER SUPPLY
COMPENSATING COILS
MODULATING COILS
SAMPLE COIL
LOW PROBE
LOW DETECTOR
LOW OSCILLATOR
OSCILLOSCOPE
MODULATING COIL POWER SUPPLY
157

Figure 18

FIGURE 19: OSCILLATOR AND DETECTOR CIRCUITS OF NMR MAGNETOMETER

The output of the single stage marginal oscillator is adjusted in frequency by the variable capacitor and in amplitude by the regeneration resistor. The detector stage supplies the rectified rf envelope to the audio amplifier. The table lists the different parameters used for the high and low frequency ranges (see Figure 1.) (Refer to pages 73, 78, 80.)

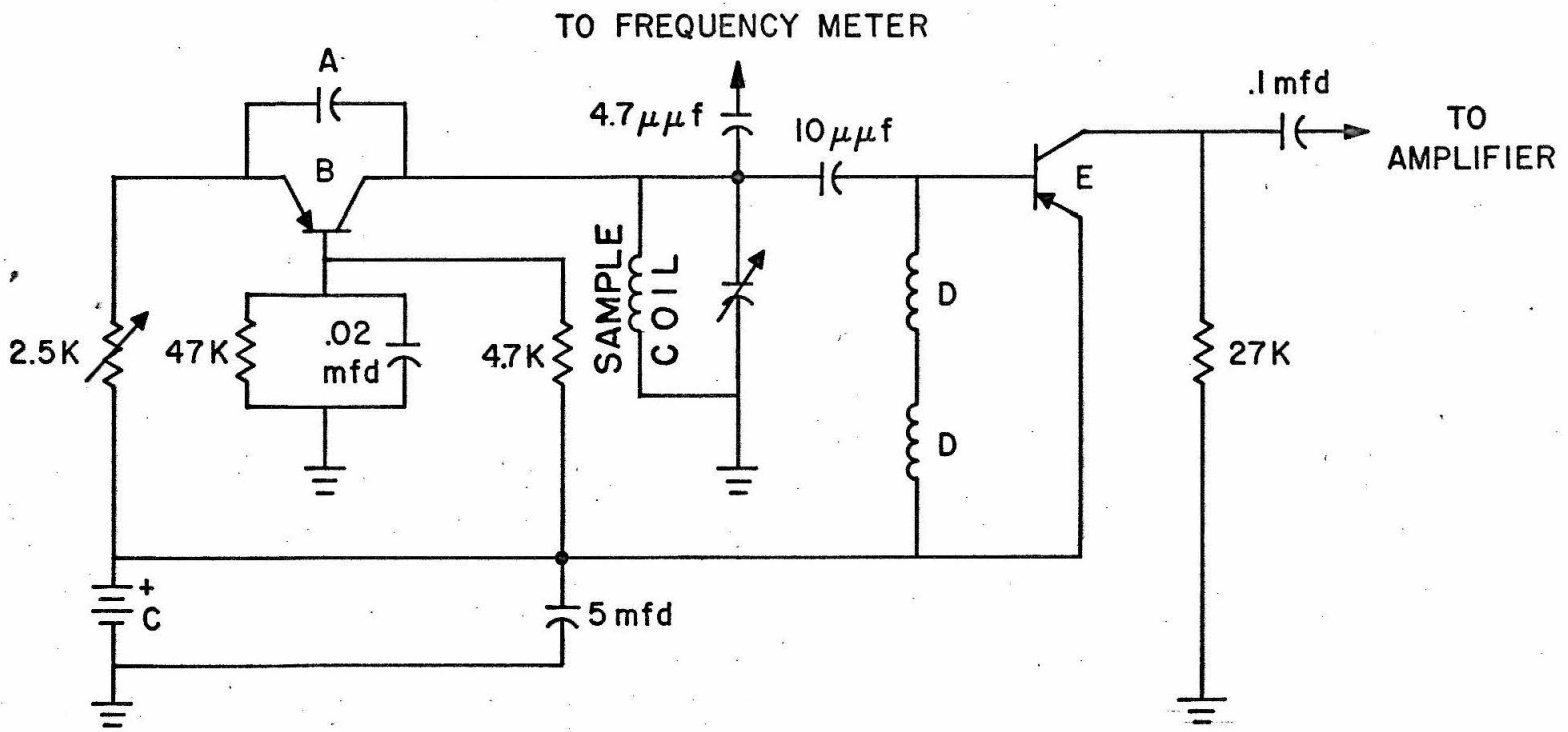

COMPONENT	LOW	HIGH
A	10μμf	22μμf
B	2N247	2N384
C	8V	12V
D	470μh	60μh
E	2N247	2N501

Figure 19

FIGURE 20: SCHEMATIC DRAWINGS OF MAGNETOMETER COMPENSATING COILS

The isometric sketch shows the relative positions of (A) the sample coil, (B) the modulating field coils, and (C) the compensating coils. Section A-A displays a cross section of the compensating coils and the volume occupied by the sample with the approximate scale of the drawing indicated by the 1-cm reference line. The field directions are shown; over the sample volume the field gradient is uniform, and both opposite and approximately equal to the external field gradient. The compensating coils ideally contribute no field to the center of the sample volume. (See page 74.)

Figure 20

(a)

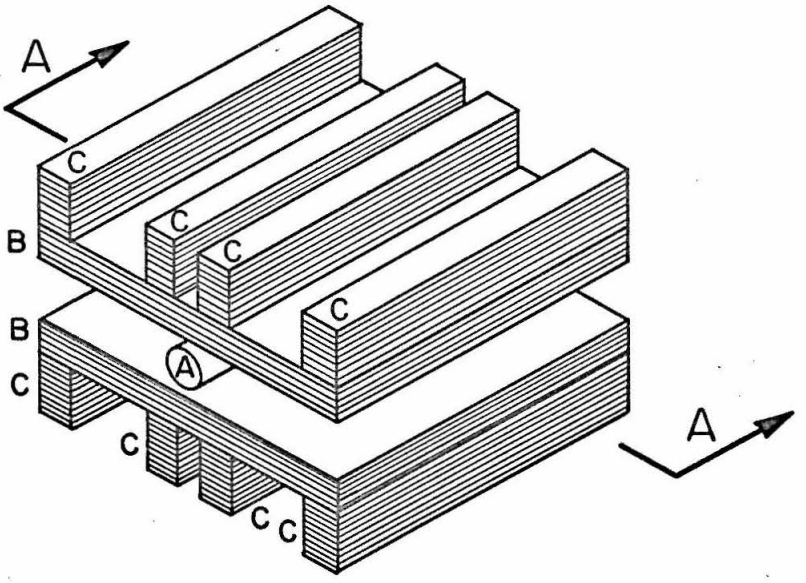

(b)

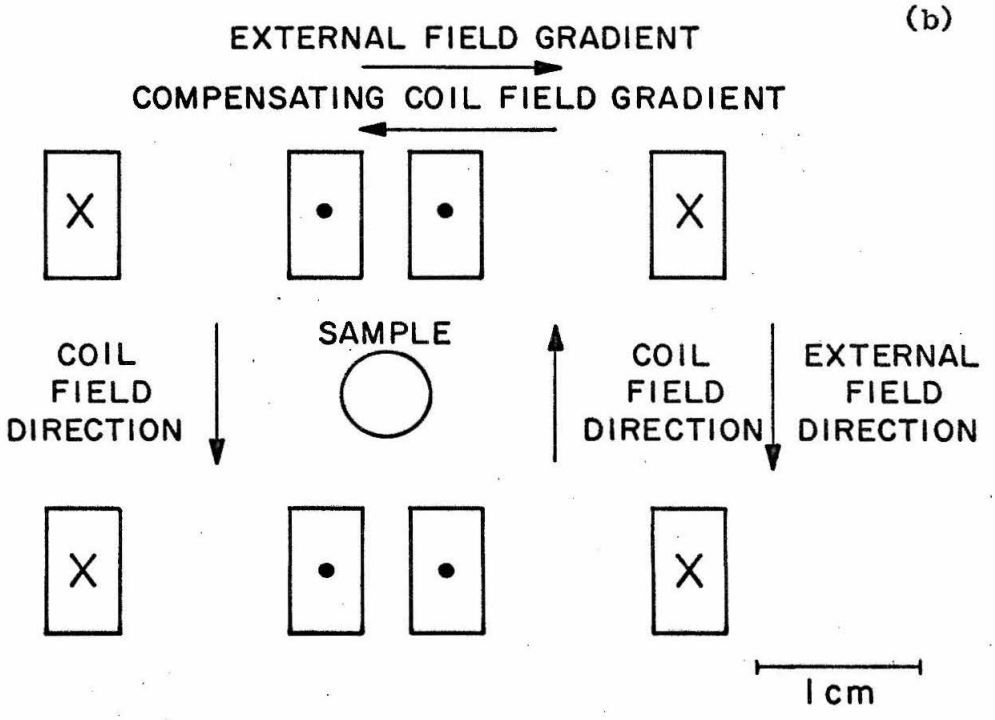

SECTION A-A

FIGURE 21: SCHEMATIC ILLUSTRATION

OF MAGNETOMETER COMPONENTS

(a) A section through the magnet shows:

A. vacuum chamber
B. detector box
C. focal plane
D. low frequency probe
E. high frequency probe
F. anti-scattering baffles
G. maximum limits of beam, focus on central ray
H. high frequency oscillator and detector
I. low frequency oscillator and detector
J. BNC connector joining coaxial brass tubes
K. two rods (one behind the other) controlling high frequency variable capacitor and regeneration
L. two rods (one behind the other) controlling low frequency variable capacitor and regeneration
M. gear box
N. selsyn
O. support for gear box
P. plywood flooring of spectrometer table
Q. outer return

(b) The front section of the gear box and selsyns shows:

R. gear box
S. gear controlling high frequency capacitance
T. gear controlling low frequency capacitance
U. gear controlling low frequency regeneration
V. gear controlling high frequency regeneration
W. selsyn controlling high and low frequency regeneration
X. selsyn controlling high and low frequency capacitance

(See pages 15, 76f.)

Figure 21

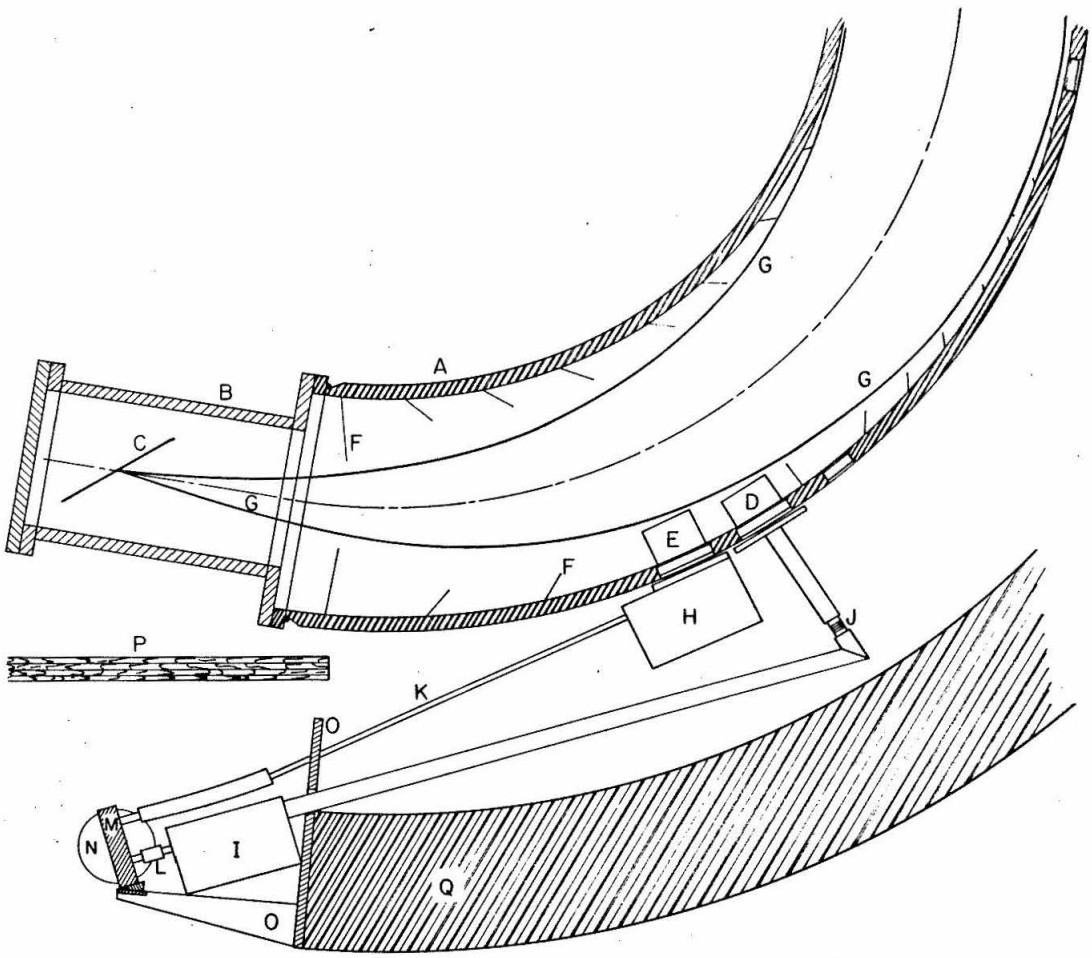

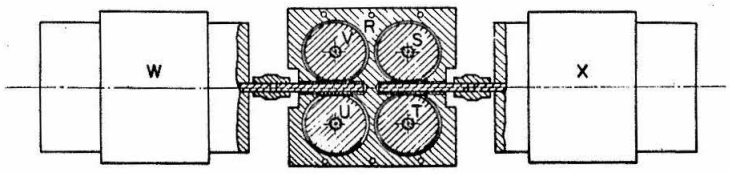

FIGURE 22: ASSEMBLY DRAWING OF ARRAY

The array is shown within the detector box in the side and top views of (a). In (b) and (c) sections show details of the movable foil holder assembly and details of the detector locations respectively. The detector box is bolted to the exit flange of the magnet, to the right of the two left-hand views in (a).

Some of the components are:

1. array baseplate which is bolted to detector box
3. array support, permanently attached to (1)
5-6. foil holders
8-9. push rods for operating foil holders
11-12-27. positioning guides for fixing z position
13. original slit assembly, milled tantalum sheet
15. foil holder spring
17. foil holder hinge assembly
18. detectors

(See pages 83ff.)

Figure 22a

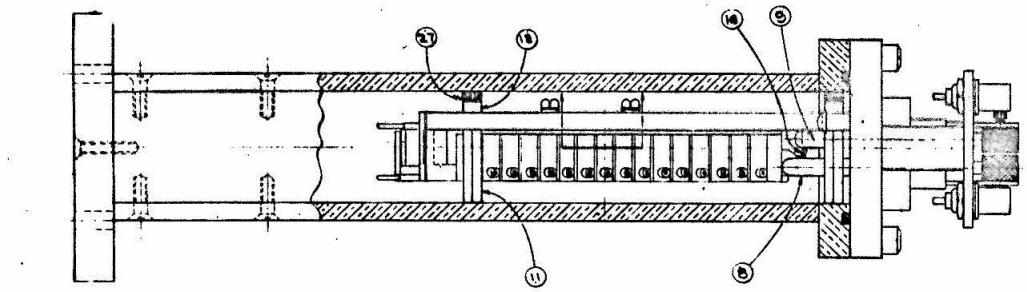

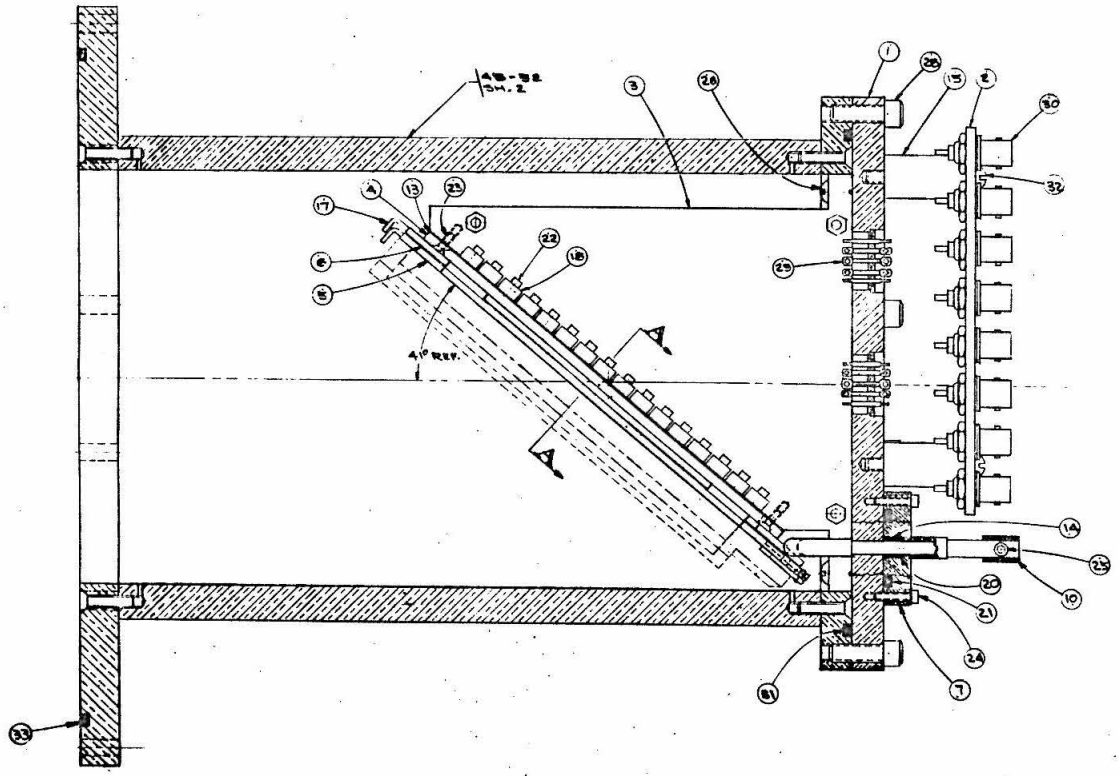

Figure 22

(b)

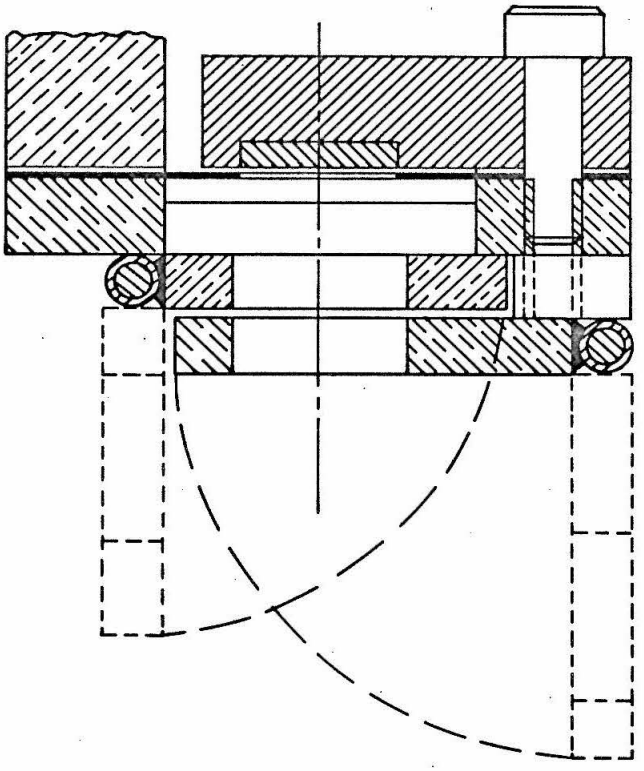

SECTION A-A

(c)

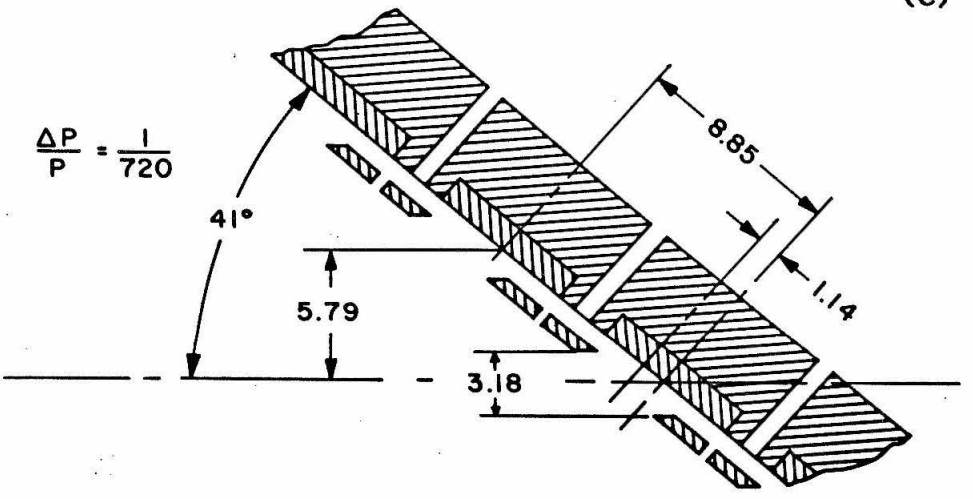

SECTION B-B

FIGURE 23: BLOCK DIAGRAM OF
SIXTEEN DETECTOR ARRAY ELECTRONICS

Since all detectors have identical circuitry (except that detector 1 needs no routing pulse), the circuitry of an arbitrary detector is shown. Apparatus located at the spectrometer is indicated by solid lines, that located in the control area by broken lines. (See pages 85ff.)

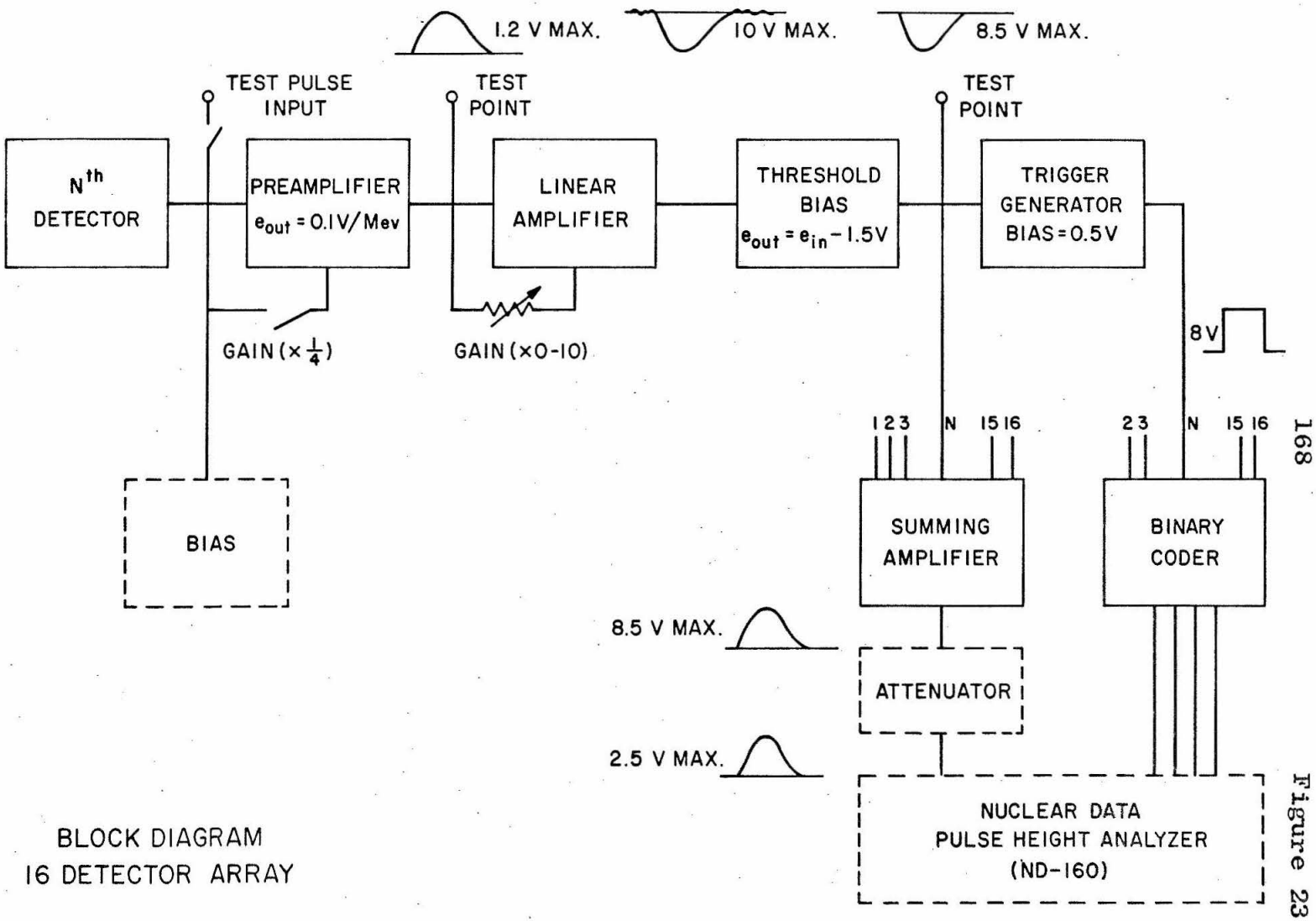

BLOCK DIAGRAM
16 DETECTOR ARRAY

Figure 23

FIGURE 24: FREQUENCY FACTOR DATA

The circles indicate the frequency positions of the Po^{212} alpha line as the magnetic field is moved over the surface of each of the sixteen array detectors. The frequency is plotted against the calculated distance along the focal plane; the point determined for each detector is adjacent to the detector number. (See page 92; Table VI.)

Similar data have been obtained for use with emulsions. The closed circles are the frequencies of the Po^{212} alpha line for eleven field settings plotted against emulsion distance and normalized to the detector 8 position. (See pages 57, 96; Table VII.)

Curvature of the data from the straight line indicates the dispersion change across the focal plane.

Figure 24

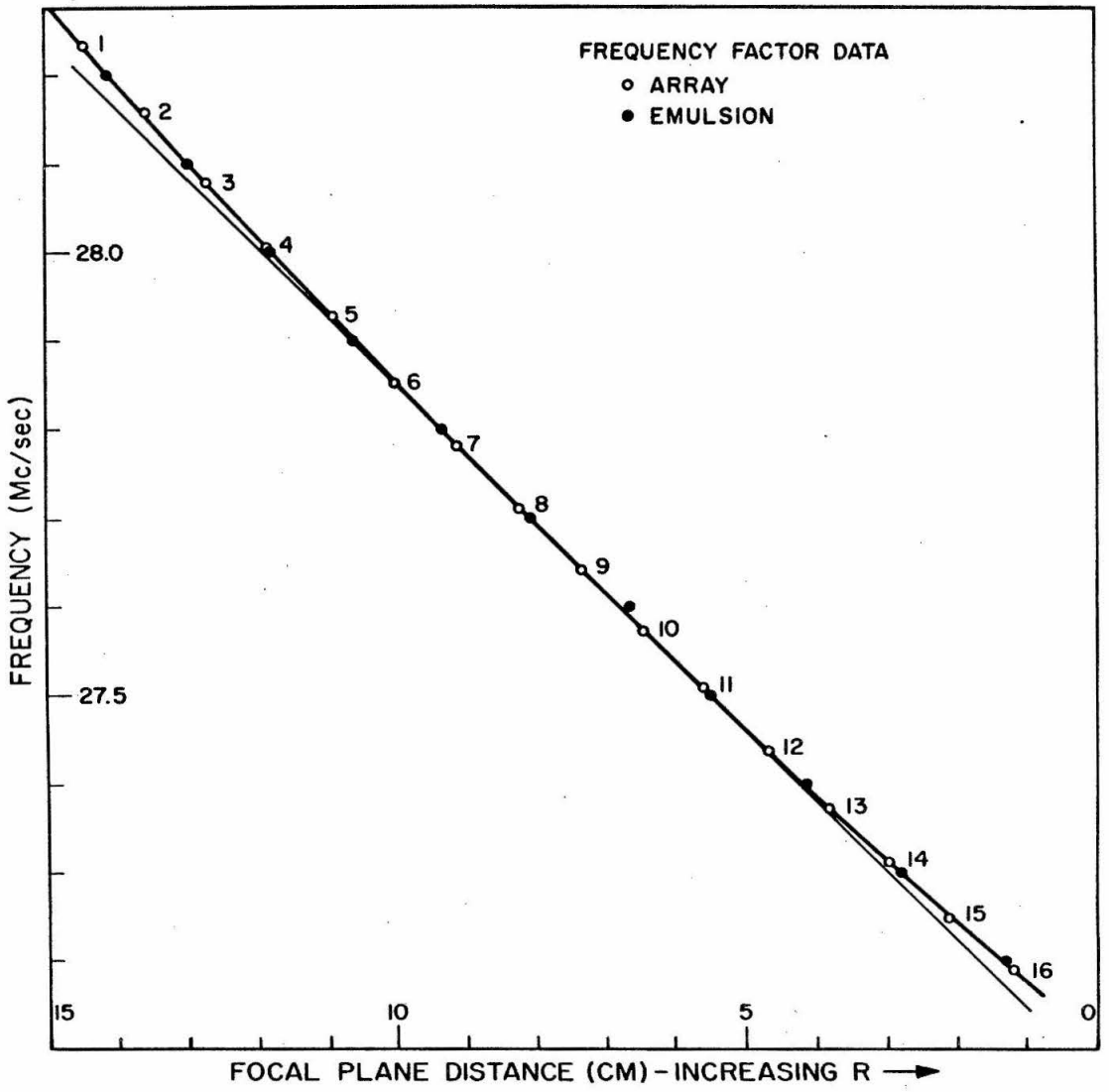
FREQUENCY FACTOR DATA
ARRAY
EMULSION
1
2
3
4
5
6
7
8
9
10
11
12
13
14
15
16
28.0
27.5
FREQUENCY (Mc/sec)
15
10
5
0
FOCAL PLANE DISTANCE (CM) - INCREASING R

FIGURE 25: YIELD FACTORS

Experimental yield factors of L. Cocke plotted with a solid curve derived from the frequency factor data (Table VI) are shown. Owing to array changes these yield factors are not valid for the analysis of recent data. They were obtained with $\Delta \phi = 15$ and $\Delta\theta = 2.5$. (See pages 94f.)

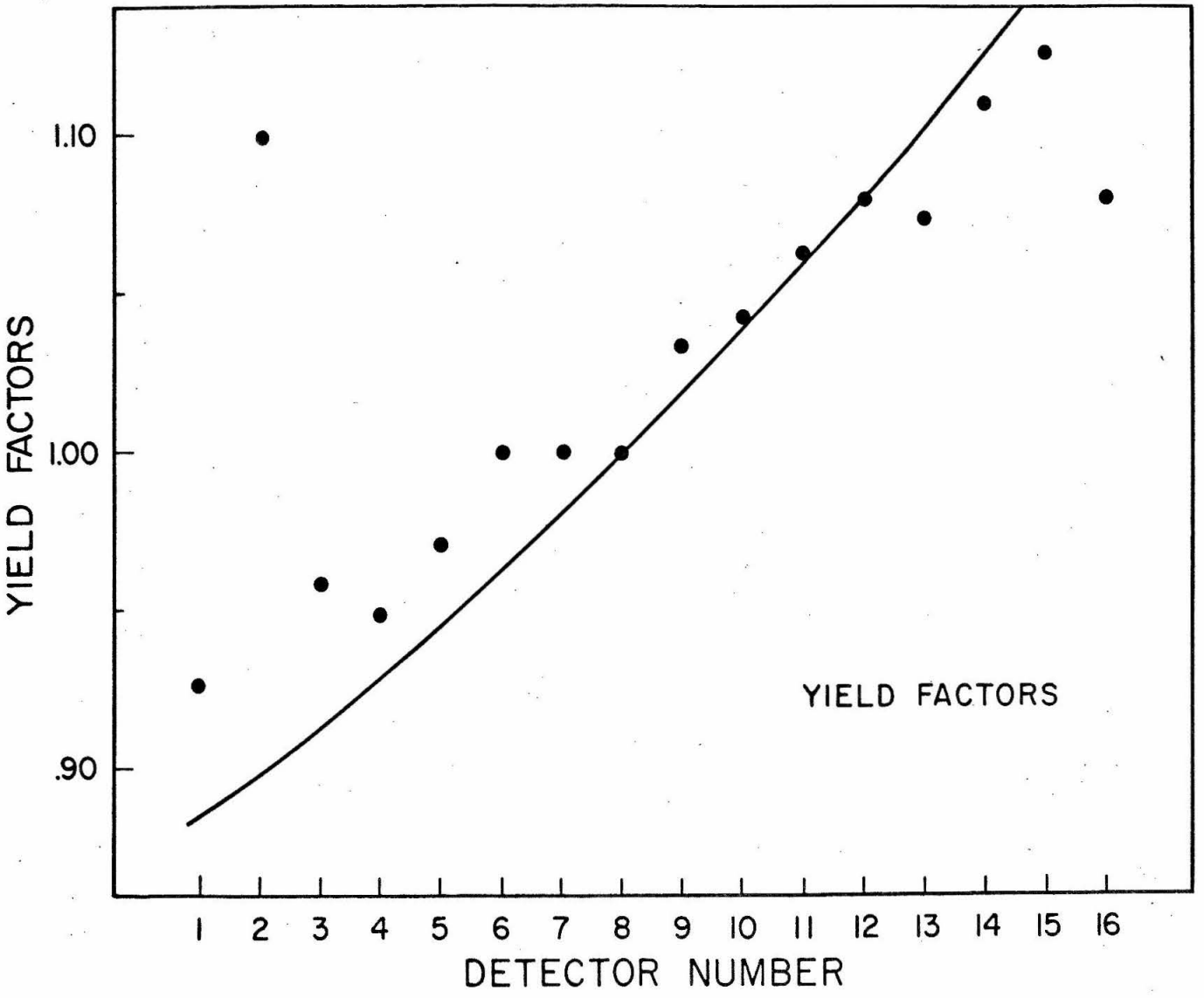
YIELD FACTORS
1.10
1.00
.90
YIELD FACTORS
1 2 3 4 5 6 7 8 9 10 11 12 13 14 15 16
DETECTOR NUMBER

Figure 25

FIGURE 26: DETECTOR 16 TRANSMISSION DATA FOR DIFFERENT SOLID ANGLES

Protons scattered from a gold foil are observed by detector 16 with four different entrance slit openings. The Θ aperture is 1.33° for all cases. The lower ϕ slit reading is 0 and the upper ϕ reading is:

1) 25
2) 20
3) 15
4) 10

The areas of the four right-hand curves are plotted on the left side. Because of beam interception by the magnetometer canisters the transmission does not increase linearly above $\phi = 15$. (See page 95.)

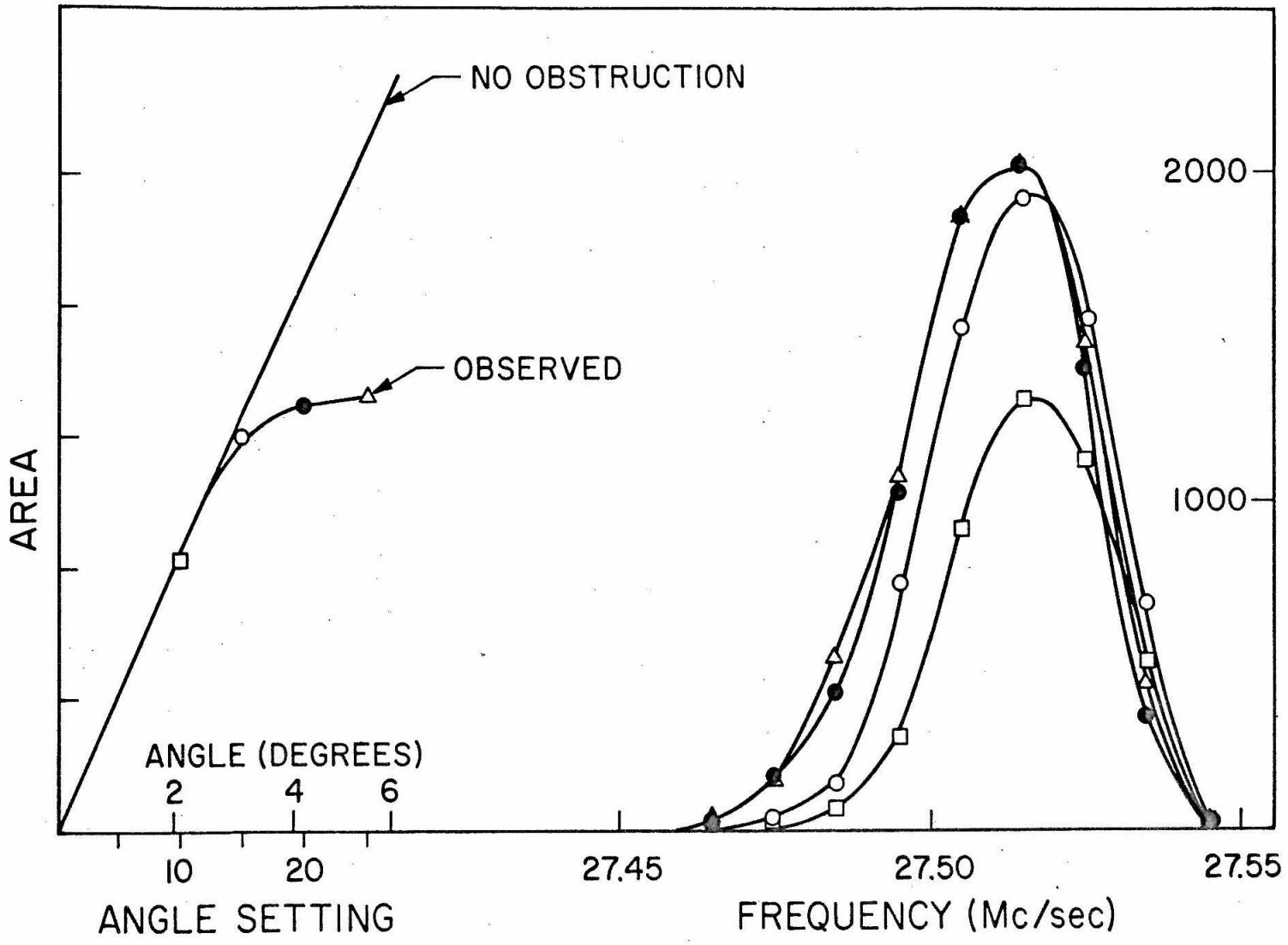
NO OBSTRUCTION
OBSERVED
AREA
ANGLE (DEGREES)
2
4
6
10
20
ANGLE SETTING
2000
1000
COUNTS
27.45
27.50
27.55
FREQUENCY (Mc/sec)

Figure 26